

Contents lists available at ScienceDirect

Journal of Computational Physics

journal homepage: www.elsevier.com/locate/jcp



Spatially quasi-periodic bifurcations from periodic traveling water waves and a method for detecting bifurcations using signed singular values



Jon Wilkening a,*, Xinyu Zhao b

- ^a Department of Mathematics, University of California, Berkeley, Berkeley, CA 94720, USA
- ^b Department of Mathematics and Statistics, McMaster University, Hamilton, Ontario L8S 4K1, Canada

ARTICLE INFO

Article history: Received 11 August 2022 Received in revised form 17 January 2023 Accepted 18 January 2023 Available online 26 January 2023

Keywords:
Water waves
Quasi-periodic solution
Bifurcation detection
Numerical continuation
Analytic singular value decomposition
Bloch-Fourier theory

ABSTRACT

We present a method of detecting bifurcations by locating zeros of a signed version of the smallest singular value of the Jacobian. This enables the use of quadratically convergent root-bracketing techniques or Chebyshev interpolation to locate bifurcation points. Only positive singular values have to be computed, though the method relies on the existence of an analytic or smooth singular value decomposition (SVD). The sign of the determinant of the Jacobian, computed as part of the bidiagonal reduction in the SVD algorithm, eliminates slope discontinuities at the zeros of the smallest singular value. We use the method to search for spatially quasi-periodic traveling water waves that bifurcate from large-amplitude periodic waves. The water wave equations are formulated in a conformal mapping framework to facilitate the computation of the quasi-periodic Dirichlet-Neumann operator. We find examples of pure gravity waves with zero surface tension and overhanging gravity-capillary waves. In both cases, the waves have two spatial quasi-periods whose ratio is irrational. We follow the secondary branches via numerical continuation beyond the realm of linearization about solutions on the primary branch to obtain traveling water waves that extend over the real line with no two crests or troughs of exactly the same shape. The pure gravity wave problem is of relevance to ocean waves, where capillary effects can be neglected. Such waves can only exist through secondary bifurcation as they do not persist to zero amplitude. The gravity-capillary wave problem demonstrates the effectiveness of using the signed smallest singular value as a test function for multi-parameter bifurcation problems. This test function becomes mesh independent once the mesh is fine enough.

© 2023 The Author(s). Published by Elsevier Inc. This is an open access article under the CC BY license (http://creativecommons.org/licenses/by/4.0/).

1. Introduction

This paper has the dual purpose of carrying out a detailed computational study of new families of spatially quasi-periodic traveling water waves that bifurcate from finite-amplitude periodic waves and developing a new test function for detecting bifurcations in general. We begin with a discussion of water waves.

E-mail addresses: wilkening@berkeley.edu (J. Wilkening), zhaox171@mcmaster.ca (X. Zhao).

^{*} Corresponding author.

The study of traveling solutions of the free-surface water wave problem has a long history. Stokes [76] first studied two-dimensional periodic traveling solutions in the gravity-driven case without surface tension. He constructed an asymptotic expansion of the solution in powers of an amplitude parameter and conjectured that the highest-amplitude solution possesses a wave crest with a sharp 120° interior corner angle. This was proved 100 years later by Amick, Fraenkel and Toland [7]. Longuet-Higgins and Fox [59] carried out a matched asymptotic analysis of the almost-highest traveling water wave and discovered that interesting oscillatory structures develop near the wave crest as the wave height approaches that of the sharply-crested wave of greatest height. They also showed that the wave speed ceases to increase monotonically as the wave crest sharpens, and instead possesses an infinite number of turning points.

The problem of traveling gravity waves in two dimensions can be studied as a bifurcation problem with a one-dimensional kernel [20,21,81]. In this setting, nonlinear solutions form a bifurcation branch from the zero amplitude solution. This branch is called the primary branch. Plotnikov [70] proved that there are infinitely many critical points, either turning points or bifurcation points on this primary branch. In [21], Buffoni, Dancer and Toland showed that for each sufficiently large value of the integer m, there exists a secondary bifurcation branch of solutions of period $2\pi m$ bifurcating from a 2π -periodic solution near the highest wave. These results build on earlier work of Chen and Saffman [24], who computed subharmonic bifurcations corresponding to m=2 and m=3. Zufiria computed a sequence of 3 bifurcations within an m=6 framework, the third being a symmetry-breaking bifurcation that leads to a branch of non-symmetric traveling gravity waves [96]. Vanden-Broeck [85] further extended Chen and Saffman's results to m=9 and provided numerical evidence that the bifurcated solutions approach non-periodic waves when m approaches infinity. Our goal in this paper is to study such secondary bifurcations with infinite spatial period, which requires new techniques beyond the usual setting of periodic waves.

In [18], as an alternative to imposing periodic boundary conditions, Bridges and Dias propose a quasi-periodic (QP) framework to study weakly nonlinear traveling solutions of the gravity-capillary water wave problem. The solution of the linearized problem can be written as a superposition of two cosine waves whose wave numbers k_1 and k_2 are both solutions of the dispersion relation

$$c^2 = \frac{g}{k} + \tau k. \tag{1.1}$$

Here g is the acceleration of gravity, τ is the surface tension coefficient, and c is the wave speed, which must be the same for $k=k_1$ and $k=k_2$. This is a generalization of the Wilton ripple problem [2,82,93] to the case that k_1 and k_2 are irrationally related. In [91], the present authors propose a conformal mapping approach [25,37–39,42,71,78] to generalize the QP framework of Bridges and Dias to the fully nonlinear water wave regime, numerically confirming the existence of spatially quasi-periodic traveling water waves. The conformal map simplifies the computation of the Dirichlet-Neumann operator to a QP variant of the Hilbert transform.

The solutions in the two-parameter family computed in [91] persist to zero amplitude as QP waves, where they include both branches of the dispersion relation (1.1) as special cases. The left and right branches are classified by Djordjevic and Redekopp [36] as gravity waves and capillary waves, respectively. At the scale of gravity waves in the ocean, the wave number of capillary waves is typically 10^7 times larger than that of gravity waves. Such a large wave number ratio is computationally out of reach in our framework; moreover, we would not expect to find interesting nonlinear interactions between waves of such vastly different length scales. Thus, if we wish to find QP traveling waves that might be found in the ocean, we must look beyond families of solutions that persist to zero-amplitude and consider the secondary bifurcation problem. In this regime, one may as well set $\tau = 0$, which motivates our study of QP solutions of the pure gravity wave problem. For simplicity, and for comparison to the gravity-capillary waves found in [91], we focus on the case $k_2/k_1 = 1/\sqrt{2}$.

A useful feature of the conformal mapping framework is the possibility of studying overhanging waves [41], where the wave profile is not the graph of a single-valued function. In [92], the present authors consider the spatially quasiperiodic initial value problem for water waves and compute a solution that begins at t=0 with a periodic wave profile but a QP velocity potential. Each of the infinite number of wave crests evolves differently as time advances, with some waves overturning and others flattening out. We now pose the question of whether overhanging quasi-periodic traveling water waves exist. Clearly surface tension or hydroelastic forces will be needed to balance the force of gravity in a steady, overhanging state. Crapper [28] discovered a family of exact overhanging periodic traveling solutions of the pure capillary wave problem (with no gravity). Kinnersley [54] found analogues of these exact solutions in finite depth, expressed in terms of elliptic functions, again for the pure capillary wave problem. Schwartz and Vanden-Broeck [73] computed and classified several families of traveling gravity-capillary waves, providing several examples of overhanging waves. Guyenne and Parau [50] and Wang et al. [86] computed overhanging traveling solutions of the flexural gravity wave problem of an ice sheet over deep water. Akers, Ambrose and Wright [1] show that Crapper's pure capillary wave solution can be perturbed to account for gravity. In the present work, we search for QP bifurcations from the two-parameter family of periodic waves referred to by Schwartz and Vanden-Broack as "type 1 waves." We obtain a new two-parameter family of QP gravity-capillary waves. The largest-amplitude waves in this family exhibit an infinite, non-repeating pattern of erratically-spaced overhanging waves, each with a different shape.

Because QP waves are represented by periodic functions on higher-dimensional tori, computing large-amplitude QP traveling waves is a high-dimensional nonlinear optimization problem. We build on the basic framework of Wilkening and Yu [90], who formulated the search for standing waves as an overdetermined nonlinear least squares problem. In the

present setting of QP traveling waves, we optimize over a two-dimensional array of Fourier coefficients to represent a one-dimensional QP function. The 1D water wave equations are imposed in the characteristic direction (k_1, k_2) at each point of a uniform grid overlaid on the two-dimensional QP torus in physical (as opposed to Fourier) space. The problem is overdetermined since we zero-pad the Fourier representation of the solution so that the nonlinear least squares solver only has access to the lower-frequency modes of the solution. This reduces aliasing errors and improves the efficiency of the computation by reducing the number of degrees of freedom for a given grid spacing. We wrote a custom Levenberg-Marquardt solver that employs ScaLapack on a supercomputer to carry out the linear least squares problems that govern the trust region search steps [67].

We also present a new test function¹ for locating bifurcation points in finite or infinite dimensional equilibrium problems. We combine the best features of the singular value decomposition (SVD) approach [26,75]; the Jacobian determinant approach [4,16,57,83]; the minimally augmented systems approach [5,48,49,57]; and the continuation of invariant subspaces (CIS) approach [14–16,30,35,46]. To find branch points in equilibrium problems, say f(q) = 0, where q = (u, s) with $u \in \mathbb{R}^n$ and $s \in \mathbb{R}$, one searches for parameter values s on a path q(s) of solutions at which the dimension of the kernel of the Jacobian $\mathcal{J}(s) = f_q(q(s))$ increases by one. Often one defines an augmented (or extended) Jacobian, $\mathcal{J}^e(s)$, consisting of $\mathcal{J}(s)$ with an extra row consisting of a multiple of the transpose of q'(s), which is tangent to the primary branch of solutions. In bifurcation problems arising in low-dimensional dynamical systems, the determinant of $\mathcal{J}^e(s)$ can be used as a test function that changes sign at simple bifurcations. In this case, the method presented here has the same theoretical justification; see, e.g., [4]. In high dimensions, e.g. after discretizing a continuous problem, it is preferable for many reasons (discussed in Section 3.2) to search for zeros of the smallest singular value $\sigma_{\min}(s)$ of $\mathcal{J}^e(s)$ rather than using the determinant to locate bifurcation points. But singular values are usually computed as non-negative numbers, which leads to slope discontinuities in $\sigma_{\min}(s)$ at its zeros and precludes the use of root-bracketing methods. As shown by Shen [75], it is still possible to devise a Newton-type method, but this involves approximations of the second derivative operator, f_{qq} , applied in certain directions using finite difference approximations, which we aim to avoid.

We instead take advantage of the existence of an analytic singular value decomposition [22,53], or ASVD, $\mathcal{J}^e(s) = U(s)\Sigma(s)V(s)^T$, where the diagonal entries of $\Sigma(s)$, denoted $\sigma_i(s)$, can change sign and do not necessarily remain monotonically ordered. A smooth SVD [34] is sufficient if $\mathcal{J}^e(s)$ is not analytic. Sign changes in $\sigma_{\min}(s)$ eliminate the slope discontinuities at its zeros. The standard SVD transfers negative signs in $\sigma_{\min}(s)$ to the corresponding column of U(s) or row of $V(s)^T$, which changes the sign of one of their determinants. We can recover the signed version by defining $\chi(s) = \det(U(s)) \det(V(s)) \sigma_{\min}(s) = (\operatorname{sgn} \det \mathcal{J}^e(s)) \sigma_{\min}(s)$ as a test function whose zeros coincide with bifurcation points, where now the standard SVD with positive singular values is being used. This opens the door to using quadratically convergent derivative free methods such as Brent's method [17] to locate the zeros of $\chi(s)$. We show that once enough Fourier modes are employed to resolve both the underlying periodic traveling wave and the left and right singular vectors corresponding to $\sigma_{\min}(s)$, then $\chi(s)$ becomes independent of N, the Fourier cutoff index. Other methods we are familiar with make stronger use of the finite-dimensional status of the truncated problem, leading to test functions with no infinite-dimensional limit. Having a globally defined test function $\chi(s)$ that does not change on refining the mesh is particularly useful in multi-parameter problems, with $s \in \mathbb{R}^d$. We demonstrate this with d=2 in Section 4.2.

Another effective method of locating bifurcations is to border $\mathcal{J}^e(s)$ with a carefully chosen additional row and column to obtain a matrix $\mathcal{J}^{ee}(s)$ and solve

$$\mathcal{J}^{ee}(s) \begin{pmatrix} r \\ \psi \end{pmatrix} = \begin{pmatrix} 0 \\ 1 \end{pmatrix}, \qquad r, 0 \in \mathbb{R}^{n+1}, \quad \psi, 1 \in \mathbb{R}. \tag{1.2}$$

The scalar function $\psi(s)$ can then be used as a test function whose zeros coincide with the desired branch points [5,14,16, 48,49,57]. We discuss this approach further in Section 3.2 and compare the relative merits of $\chi(s)$ and $\psi(s)$, one being that $\psi(s)$ will change discontinuously if the mesh is refined adaptively as s changes while $\chi(s)$ will not.

To reduce the cost of searching for quasi-periodic bifurcation points, we take advantage of Bloch-Fourier theory for diagonalizing linear operators over periodic potentials [55]. This technique has proved useful for studying subharmonic stability of water waves [29,58,61,62,65,80,82], but requires reformulation to fit with our quasi-periodic torus framework. Decomposing the Fréchet derivative of the traveling water wave equations in the QP torus representation into a direct sum of Bloch-Fourier operators allows us to focus on a single Bloch frequency when searching for bifurcations. The dimension of the restricted operator corresponds to points in a one-dimensional subset of the two-dimensional Fourier lattice, which makes it possible to locate QP bifurcations from very large-amplitude periodic traveling waves. Tracking the bifurcation curves beyond linearization about traveling waves then brings in the full 2D array of Fourier modes for the torus representation of the solution.

This paper is organized as follows. In Section 2 we review the equations governing spatially quasi-periodic traveling water waves [91] and describe the numerical continuation algorithm we use to compute both periodic and quasi-periodic traveling waves. In Section 3, we introduce spaces of real-analytic torus functions, work out the Bloch-Fourier theory of quasi-periodic bifurcations from traveling waves, define and analyze the test function $\chi(s)$ for identifying bifurcation points,

¹ Here we use terminology from the computational dynamical systems literature [16,57], where a test function changes sign at a simple bifurcation; it is not related to test functions from the theory of distributions.

and show how to compute the sign of the determinant of a matrix efficiently along with its singular values. In Section 4, we present numerical results for the QP gravity wave problem and study a two-parameter bifurcation problem leading to examples of overhanging QP traveling gravity-capillary waves. In the appendices, we discuss the effects of floating-point arithmetic on $\chi(s)$ and prove that the Fréchet derivative for this problem is a bounded operator between spaces of real analytic torus functions when the parameters of these spaces are chosen appropriately. Concluding remarks are given in Section 5.

2. Spatially quasi-periodic water waves

2.1. Governing equations for traveling waves

We study the problem of traveling gravity-capillary water waves over a two-dimensional, irrotational, inviscid fluid of infinite depth. We adopt a conformal mapping formulation [25,37,40,78,91] of the problem; specifically, we consider a conformal map

$$\tilde{z}(w) = \tilde{x}(w) + i\tilde{y}(w), \qquad w = \alpha + i\beta$$
 (2.1)

that maps the lower half plane

$$\mathbb{C}^{-} := \{ \alpha + i\beta : \quad \alpha \in \mathbb{R}, \quad \beta < 0 \} \tag{2.2}$$

to the fluid domain in physical space. Here time has been frozen at t = 0 and dropped from the notation, and we place a tilde over functions defined on the real line to simplify the notation for higher-dimensional torus representation of quasi-periodic functions. This is the opposite convention of [91,92], but seems more natural in hindsight. When the free surface is single-valued in physical space, the fluid domain has the form

$$\Omega := \{ (x, y) : -\infty < y < \tilde{\eta}^{\text{phys}}(x), \quad x \in \mathbb{R} \}, \tag{2.3}$$

where $\tilde{\eta}^{\text{phys}}$ is the free surface elevation. To fix the map, we assume that \tilde{z} satisfies

$$\lim_{\beta \to -\infty} \tilde{z}_w = 1 \quad \text{and} \quad \tilde{z}(0) = 0. \tag{2.4}$$

We also assume that $\tilde{z}(w)$ can be extended continuously to $\overline{\mathbb{C}^-}$ and maps the real line $\beta=0$ to the free surface. We introduce the notation $\tilde{\zeta}=\tilde{z}|_{\beta=0}$, $\tilde{\xi}=\tilde{x}|_{\beta=0}$ and $\tilde{\eta}=\tilde{y}|_{\beta=0}$ so that the free surface is parameterized by

$$\tilde{\xi}(\alpha) = \tilde{\xi}(\alpha) + i\tilde{\eta}(\alpha), \qquad \tilde{\eta}(\alpha) = \tilde{\eta}^{\text{phys}}(\tilde{\xi}(\alpha)), \qquad \alpha \in \mathbb{R}.$$
 (2.5)

If the free-surface is not single-valued in physical space, one may drop the condition that $\tilde{\eta}(\alpha) = \tilde{\eta}^{\text{phys}}(\tilde{\xi}(\alpha))$ and simply require that $\tilde{\zeta}(\alpha)$ does not self-intersect; see [91].

In this paper, we focus on the cases where $\tilde{\eta}(\alpha)$ is periodic or quasi-periodic with two quasi-periods. As defined in [43,64], such a function $\tilde{\eta}$ is of the form

$$\tilde{\eta}(\alpha) = \eta(k_1 \alpha, k_2 \alpha), \qquad \eta(\alpha_1, \alpha_2) = \sum_{(j_1, j_2) \in \mathbb{Z}^2} \hat{\eta}_{j_1, j_2} e^{i(j_1 \alpha_1 + j_2 \alpha_2)},$$
(2.6)

where η is defined on the torus $\mathbb{T}^2 = \mathbb{R}^2/(2\pi\mathbb{Z})^2$. After non-dimensionalization, we may assume that the two basic frequencies of $\tilde{\eta}$ are

$$k_1 = 1, \qquad k_2 = k,$$
 (2.7)

where k is irrational. We refer to such functions η as torus functions and $\tilde{\eta}$ as having been extracted or reconstructed from η . One can observe that the form (2.6) still applies when $\tilde{\eta}$ is periodic; in this case, the corresponding torus function satisfies

$$\eta(\alpha_1, \alpha_2) = \tilde{\eta}(\alpha_1), \qquad \alpha_1, \alpha_2 \in \mathbb{T}. \tag{2.8}$$

This allows us to use $\eta(\alpha_1, \alpha_2)$ to represent both quasi-periodic and periodic functions $\tilde{\eta}(\alpha)$.

In [91], quasi-periodic traveling gravity-capillary waves on deep water are formulated in terms of $\eta(\alpha_1, \alpha_2)$. The governing equations for η read

$$P\left[\frac{b}{2J} + g\eta - \tau\kappa\right] = 0, \qquad b = c^2, \qquad \xi = H[\eta],$$

$$J = (1 + \partial_{\alpha}\xi)^2 + (\partial_{\alpha}\eta)^2, \qquad \kappa = \frac{(1 + \partial_{\alpha}\xi)(\partial_{\alpha}^2\eta) - (\partial_{\alpha}\eta)(\partial_{\alpha}^2\xi)}{J^{3/2}},$$
(2.9)

where c is the wave speed; g is the gravitational acceleration; τ is the surface tension coefficient; and ξ , J and κ are auxiliary torus functions representing the quasi-periodic part of the horizontal parameterization of the free surface, the square of the arclength element, and the curvature, respectively. For gravity waves, τ is zero. The operators P, H and ∂_{α} are defined by

$$P = id - P_{0}, P_{0}[f] = \frac{1}{(2\pi)^{2}} \int_{\mathbb{T}^{2}} f(\alpha_{1}, \alpha_{2}) d\alpha_{1} d\alpha_{2},$$

$$H[f](\alpha_{1}, \alpha_{2}) = \sum_{j_{1}, j_{2} \in \mathbb{Z}} (-i) \operatorname{sgn}(j_{1} + kj_{2}) \hat{f}_{j_{1}, j_{2}} e^{i(j_{1}\alpha_{1} + j_{2}\alpha_{2})},$$

$$\partial_{\alpha} f(\alpha_{1}, \alpha_{2}) = (\partial_{\alpha_{1}} + k\partial_{\alpha_{2}}) f(\alpha_{1}, \alpha_{2}).$$
(2.10)

Here $\partial_{\alpha} = (1, k)^T \cdot \nabla$ is the directional derivative in the (1, k) direction on the torus; H is the "quasi-periodic Hilbert transform" [91]; and

$$\operatorname{sgn}(a) = \begin{cases} 1, & a > 0, \\ 0, & a = 0, \\ -1, & a < 0. \end{cases}$$
 (2.11)

Note that ∂_{α} and H act on torus functions in such a way that extracting the 1d function from the result is equivalent to first extracting the function and then applying the 1d derivative or Hilbert transform operators:

$$(\partial_{\alpha} f)(\alpha, k\alpha) = \partial_{\alpha} [f(\alpha, k\alpha)],$$

$$(Hf)(\alpha, k\alpha) = H[f(\cdot, k\cdot)](\alpha) = \frac{1}{\pi} PV \int_{-\infty}^{\infty} \frac{f(\beta, k\beta)}{\alpha - \beta} d\beta.$$
(2.12)

Both ∂_{α} and H are diagonal in 2D Fourier space, with Fourier multipliers

$$\widehat{\partial_{j_1,j_2}} = i(j_1 + kj_2), \qquad \widehat{H}_{j_1,j_2} = (-i)\operatorname{sgn}(j_1 + kj_2), \tag{2.13}$$

respectively. Different choices of k lead to different operators.

One can check that if $\eta(\alpha_1, \alpha_2)$ is a solution of (2.9), then $\eta(-\alpha_1, -\alpha_2)$ is also a solution. In this paper we will focus on real-valued traveling solutions with even symmetry: $\eta(-\alpha_1, -\alpha_2) = \eta(\alpha_1, \alpha_2)$. Equivalently, we assume the Fourier coefficients of η satisfy

$$\hat{\eta}_{j_1,j_2} = \hat{\eta}_{-j_1,-j_2} = \overline{\hat{\eta}}_{j_1,j_2}, \qquad j_1, j_2 \in \mathbb{Z}. \tag{2.14}$$

Since adding a constant to η will not change (2.9), we assume $P_0[\eta] = 0$ when computing traveling waves. Under these assumptions, we reconstruct $\tilde{\xi}$ in (2.5) from $\xi = H[\eta]$ using

$$\tilde{\xi}(\alpha) = \alpha + \xi(\alpha, k\alpha),\tag{2.15}$$

which is an odd function. For most torus functions, adding a tilde denotes evaluation at $(\alpha, k\alpha)$, but we treat ξ as a special case and include the linear growth term α in (2.15). This is why we refer to ξ as the quasi-periodic part of the horizontal parameterization.

Remark 2.1. It is preferable to report solutions with zero mean in physical space rather than in conformal space. Let us briefly use a superscript 0 to denote a traveling wave with the above properties, which satisfies

$$\hat{\eta}_{0,0}^{(0)} = 0. \tag{2.16}$$

The desired solution only requires adjusting the (0,0) Fourier mode:

$$\hat{\eta}_{0,0} = -P_0 [(\eta^{(0)})(1 + \xi_{\alpha}^{(0)})], \qquad \hat{\eta}_{j_1,j_2} = \hat{\eta}_{j_1,j_2}^{(0)}, \qquad (j_1, j_2) \neq (0, 0),$$
(2.17)

where $\lim_{a\to\infty}\frac{1}{2a}\int_{-a}^a\tilde{\eta}(\alpha)\tilde{\xi}_{\alpha}(\alpha)\,d\alpha=0$ is the zero mean condition, and we make use of $\tilde{\xi}_{\alpha}^{(0)}=(1+\xi_{\alpha}^{(0)})$, from (2.15). Thus, we may assume $\hat{\eta}_{0,0}=0$ when computing periodic waves, quasi-periodic waves, and the bifurcation points where they meet; we can then adjust the mean of each wave computed as a simple post-processing step.

Remark 2.2. One can check that if $\eta(\alpha_1, \alpha_2) = \sum_{j_1, j_2 \in \mathbb{Z}} \hat{\eta}_{j_1, j_2} e^{i(j_1\alpha_1 + j_2\alpha_2)}$ is a real-valued solution of (2.9) with even symmetry, then the following three functions are also real-valued solutions with even symmetry:

$$\eta(\alpha_{1} + \pi, \alpha_{2}) = \sum_{j_{1}, j_{2} \in \mathbb{Z}} (-1)^{j_{1}} \hat{\eta}_{j_{1}, j_{2}} e^{i(j_{1}\alpha_{1} + j_{2}\alpha_{2})},$$

$$\eta(\alpha_{1}, \alpha_{2} + \pi) = \sum_{j_{1}, j_{2} \in \mathbb{Z}} (-1)^{j_{2}} \hat{\eta}_{j_{1}, j_{2}} e^{i(j_{1}\alpha_{1} + j_{2}\alpha_{2})},$$

$$\eta(\alpha_{1} + \pi, \alpha_{2} + \pi) = \sum_{j_{1}, j_{2} \in \mathbb{Z}} (-1)^{j_{1} + j_{2}} \hat{\eta}_{j_{1}, j_{2}} e^{i(j_{1}\alpha_{1} + j_{2}\alpha_{2})}.$$
(2.18)

2.2. Numerical algorithm

Following [91], we formulate (2.9) as a nonlinear least-squares problem and define objective and residual functions

$$\mathcal{F}[\eta, \tau, b] = \frac{1}{8\pi^2} \int_{\mathbb{T}^2} \mathcal{R}^2[\eta, \tau, b] d\alpha_1 d\alpha_2, \qquad \mathcal{R}[\eta, \tau, b] = P\left[\frac{b}{2J} + g\eta - \tau\kappa\right]. \tag{2.19}$$

We use square brackets for the functional \mathcal{F} and operator \mathcal{R} so that $\mathcal{R}(\alpha_1, \alpha_2)$ can be short-hand for $\mathcal{R}[\eta, \tau, b](\alpha_1, \alpha_2)$. We represent a torus function f in two ways, either through its values on a uniform $M_1 \times M_2$ grid on \mathbb{T}^2 , or via the fast Fourier transform coefficients of these sampled values:

$$f_{m_1,m_2} = f(2\pi m_1/M_1, 2\pi m_2/M_2) = \sum_{j_2=0}^{M_2-1} \sum_{j_1=0}^{M_1-1} \check{f}_{j_1,j_2} e^{2\pi i (j_1 m_1/M_1 + j_2 m_2/M_2)},$$

$$\check{f}_{j_1,j_2} = \frac{1}{M_1 M_2} \sum_{m_2=0}^{M_2-1} \sum_{m_1=0}^{M_1-1} f_{m_1,m_2} e^{-2\pi i (j_1 m_1/M_1 + j_2 m_2/M_2)} = \sum_{n_1,n_2 \in \mathbb{Z}} \hat{f}_{j_1+n_1 M_1,j_2+n_2 M_2}.$$
(2.20)

Here $\hat{f}_{j_1,j_2}=(4\pi^2)^{-1}\iint_{\mathbb{T}^2}f(\alpha_1,\alpha_2)e^{-i(j_1\alpha_1+j_2\alpha_2)}d\alpha_1\,d\alpha_2$ are the actual Fourier modes of $f(\alpha_1,\alpha_2)$, which are related to the FFT modes \check{f}_{j_1,j_2} by the above aliasing formula. We only store the values of the periodic arrays $\{f_{m_1,m_2}\}$ and $\{\check{f}_{j_1,j_2}\}$ with indices

$$0 \le m_1 < M_1, \quad 0 \le m_2 < M_2, \quad 0 \le j_1 \le M_1/2, \quad 0 \le j_2 < M_2,$$
 (2.21)

where we take advantage of $\check{f}_{-j_1,-j_2} = \overline{\check{f}_{j_1,j_2}}$ when $f(\alpha_1,\alpha_2)$ is real-valued to avoid having to store modes with index $j_1 < 0$. We assume M_1 and M_2 are sufficiently large and $|\hat{f}_{j_1,j_2}|$ decays sufficiently fast as $|j_1| + |j_2| \to \infty$ that

$$\check{f}_{j_1,j_2} \approx \begin{cases} \hat{f}_{j_1,j_2} & 0 \leqslant j_2 \leqslant M_2/2, \\ \hat{f}_{j_1,j_2-M_2} & M_2/2 < j_2 < M_2. \end{cases}$$
(2.22)

When evaluating $\Re[\eta, \tau, b]$, we only vary b, τ and the leading Fourier coefficients of η ,

$$\hat{\eta}_{j_1,j_2}, \quad (-N_1 \leqslant j_1 \leqslant N_1, \quad -N_2 \leqslant j_2 \leqslant N_2), \tag{2.23}$$

where N_1 and N_2 are cutoff frequencies typically taken to be around $M_1/3$ and $M_2/3$, respectively. The higher-frequency Fourier modes $\hat{\eta}_{j_1,j_2}$ with $|j_1| > N_1$ or $|j_2| > N_2$ are set to zero. This means that the FFT modes $\check{\eta}_{j_1,j_2}$ in the range (2.21) with $j_1 > N_1$ or $N_2 < j_2 < M_2 - N_2$ are set to zero. Since $\check{\eta}_{0,0}$ is also set to zero at this stage of the computation (and later adjusted via Remark 2.1), and since η is real-valued and even, satisfying (2.14), the number of independent FFT coefficients $\check{\eta}_{j_1,j_2}$ is

$$N_{\text{tot}} = N_1(2N_2 + 1) + N_2. \tag{2.24}$$

Remark 2.3. For simplicity, from now on we focus on the Fourier modes of the torus functions that arise (e.g., $\hat{\eta}_{j_1,j_2}$), with the understanding that in the numerical implementation they map to FFT modes (e.g., $\check{\eta}_{j_1,j_2}$) with indices in the ranges (2.21) via the assumption (2.22).

We evaluate $R[\eta, \tau, b](\alpha_1, \alpha_2)$ on the $M_1 \times M_2$ grid. Using the trapezoidal rule on the integral (2.19), which is a spectrally accurate approximation, we obtain an overdetermined nonlinear least-squares problem from $\mathbb{R}^{N_{\text{tot}}}$ to $\mathbb{R}^{M_1M_2}$, namely

minimize
$$F[\{\hat{\eta}_{j_1,j_2}\}; \tau, b] = \frac{1}{2}r^T r$$
, $r_{m_2M_1+m_1} = \frac{\Re(2\pi m_1/M_1, 2\pi m_2/M_2)}{\sqrt{M_1M_2}}$. (2.25)

Here we have written the objective function to suggest that τ and $b=c^2$ are prescribed parameters and the independent Fourier modes $\{\hat{\eta}_{j_1,j_2}\}$ are the unknowns over which the objective function is minimized. For small-amplitude traveling waves, as explained in [91], it is better to prescribe two Fourier modes, say $\hat{\eta}_{1,0}$ and $\hat{\eta}_{0,1}$, and include τ and b among the unknowns to be determined by solving (2.25). In the present work, as explained below, we study large-amplitude waves and use a hybrid choice in which τ and either $\hat{\eta}_{1,0}$, $\hat{\eta}_{0,1}$ or the wave height (defined below) are prescribed while b and the other Fourier modes of η are found by the solver.

One of the examples presented in [91] involves computing a two-parameter family of quasi-periodic traveling waves with $k=1/\sqrt{2}$ held fixed and $\hat{\eta}_{1,0}$ and $\hat{\eta}_{0,1}$ prescribed to vary over the interval I=[-0.01,0.01]. Each of these amplitude parameters is assigned values on a 16-point Chebyshev-Lobatto grid over I, and polynomial interpolation is used to express the surface tension coefficient τ in the form

$$\tau(\hat{\eta}_{1,0}, \hat{\eta}_{0,1}) = \sum_{m=0}^{15} \sum_{n=0}^{15} \check{\tau}_{mn} T_m(100\hat{\eta}_{1,0}) T_n(100\hat{\eta}_{0,1}), \qquad (\hat{\eta}_{1,0}, \hat{\eta}_{0,1}) \in I^2,$$
(2.26)

where $\{T_m(x)\}_{m=0}^{\infty}$ are the Chebyshev polynomials. The wave speed c is similarly interpolated. The tensor product Chebyshev coefficients $\check{\tau}_{mn}$ and \check{c}_{mn} are found to decay below 10^{-15} in amplitude for $m+n\geqslant 10$, suggesting that (2.26) is accurate to double-precision accuracy throughout the parameter region I^2 . Setting both amplitude parameters to zero gives $\tau=\tau_{\text{lin}}=g/(k_1k_2)$ and $c^2=c_{\text{lin}}^2=(k_1+k_2)\tau$, as predicted by linear theory, with g=1, $k_1=1$, $k_2=k=1/\sqrt{2}$ in this case.

The above approach sidesteps the difficulty of finding bifurcation points within the family of periodic traveling waves. Instead, all the waves in the polynomial interpolation leading to (2.26) are genuinely quasi-periodic, with non-zero values of both $\hat{\eta}_{1,0}$ and $\hat{\eta}_{0,1}$. Indeed, by using an even number of Chebyshev-Lobatto nodes, 0 is not among the interpolation points in either direction. After the expansion coefficients $\check{\tau}_{mn}$ or \check{c}_{mn} have been identified via interpolation, we can set $\hat{\eta}_{1,0}$ or $\hat{\eta}_{0,1}$ to zero to find the curves $\tau(\hat{\eta}_{1,0},0)$ or $\tau(0,\hat{\eta}_{0,1})$ where a bifurcation exists from periodic traveling waves of wave number 1 or $k=1/\sqrt{2}$ to quasi-periodic waves of wave numbers $\vec{k}=(1,k)$. These curves are the intersection of a two-parameter family of quasi-periodic solutions with a two-parameter family of periodic solutions.

In the present paper, we address the difficulty sidestepped above. We begin by computing families of large-amplitude periodic traveling waves, which can be parameterized by surface tension and one amplitude parameter. We may assume without loss of generality that $\eta(\alpha_1,\alpha_2)=\tilde{\eta}(\alpha_1)$ is independent of α_2 , as in (2.8). All the Fourier modes $\hat{\eta}_{j_1,j_2}$ with $j_2\neq 0$ are then zero, so we may drop the j_2 subscript and view $\{\hat{\eta}_j\}_{j\in\mathbb{Z}}$ as the coefficients of the 1D Fourier expansion of $\tilde{\eta}(\alpha)$. The unknowns for the periodic problem are then

$$\vec{p} = (b, \hat{\eta}_1, \hat{\eta}_2, \hat{\eta}_3, \dots, \hat{\eta}_{N_1-1}, \hat{\eta}_N),$$
 (2.27)

where $\hat{\eta}_0$ is set to 0 as discussed in Remark 2.1, $\hat{\eta}_{-j} = \hat{\eta}_j$ due to (2.14), and τ is a prescribed parameter. We also define a wave amplitude by introducing coefficients v_i and setting

$$\vec{v} \cdot \vec{p} = v_0 b + \sum_{i=1}^{N_1} v_j p_j = \mu, \tag{2.28}$$

where μ is the prescribed amplitude parameter. The two cases we consider are

case 1:
$$\vec{v} = (0, 1, 0, ..., 0),$$
 $\mu = \hat{\eta}_1 \quad (= \hat{\eta}_{1,0}),$ case 2: $v_i = 0 \ (i \text{ even}), \quad v_i = 4 \ (i \text{ odd}), \quad \mu = h = \tilde{\eta}(0) - \tilde{\eta}(\pi).$ (2.29)

In case 2, the reason for $v_j=4$ when j is odd is that $\hat{\eta}_{-j}=\hat{\eta}_j$ and together they contribute $4\hat{\eta}_j$ to the wave height, $h=\tilde{\eta}(0)-\tilde{\eta}(\pi)$, when j is odd. Note that b (j=0) and the even modes with $j\geqslant 2$ have no effect on the wave height due to cancellation. For this periodic sub-problem, both $\eta(\alpha_1,\alpha_2)$ and $\Re[\eta,\tau,b](\alpha_1,\alpha_2)$ are independent of α_2 , so one can simplify (2.25) to

minimize
$$F[\vec{p}; \mu, \tau] = \frac{1}{2}r^T r$$
, $r_m = \begin{cases} \frac{\Re(2\pi m/M_1, 0)}{\sqrt{M_1}}, & 0 \leqslant m < M_1, \\ \vec{v} \cdot \vec{p} - \mu, & m = M_1, \end{cases}$ (2.30)

where we have added an equation to enforce (2.28) and re-organized the argument list of F to separate the prescribed parameters from the unknowns.

Remark 2.4. When solutions of the periodic problem are embedded in the 2D torus representation, it is often preferable to employ the double-index Fourier notation, $\hat{\eta}_{j_1,j_2} = \hat{\eta}_{j_1} \delta_{j_2,0}$, where δ_{ij} is the Kronecker delta. The amplitude parameter in case 1 of (2.29) is then $\hat{\eta}_{1,0}$.

Remark 2.5. In case 1 of (2.29), we can alternatively drop the last component of \vec{r} in (2.30) and remove $\hat{\eta}_1$ from the vector \vec{p} of unknowns over which the minimization is performed. This mode is set equal to μ externally and not varied by the solver.

Given an initial guess $(\vec{p}^0; \mu, \tau)$ for a periodic traveling wave, we use the Levenberg-Marquardt method [67] to minimize F in (2.30) over the unknowns \vec{p} holding (μ, τ) fixed. We employ the delayed Jacobian update strategy proposed by Wilkening and Yu [90] in the context of computing standing water waves. For the initial guess, we use linear theory to get started on one or several straight-line paths through parameter space, i.e., through the (μ, τ) -plane. Once two solution on such a path have been computed, we use linear extrapolation for the starting guesses of successive solutions on the numerical continuation path. We increase N_1 and M_1 adaptively as we go to maintain spectral accuracy of the computed traveling waves.

We search for bifurcation points along the numerical continuation path of periodic traveling waves using the methods of Section 3 below. When a bifurcation branch is found, we follow it using the same strategy as for periodic traveling waves, but with $\hat{\eta}_{0,1}$ replacing μ as the first numerical continuation parameter. We use τ as the second parameter in both cases. On this branch, $\hat{\eta}_{0,1} = 0$ corresponds to the periodic traveling wave, and the list of unknowns, \vec{p} , is expanded to include the modes $\hat{\eta}_{j_1,j_2}$ with $j_2 \neq 0$:

$$\vec{p} = (b, \{\hat{\eta}_{j_1, j_2}\}), \qquad \begin{pmatrix} 1 \leqslant j_1 \leqslant N_1 \\ -N_2 \leqslant j_2 \leqslant N_2 \end{pmatrix} \text{ or } \begin{pmatrix} j_1 = 0 \\ 2 \leqslant j_2 \leqslant N_2 \end{pmatrix}.$$
 (2.31)

Here we follow the strategy of Remark 2.5 and remove $\hat{\eta}_{0,1}$ from the list \vec{p} rather than add a component to \vec{r} to govern the amplitude. Since b has replaced $\hat{\eta}_{0,1}$ in the list, we see that in the quasi-periodic problem, the number of degrees of freedom of the nonlinear least squares problem (2.25) is N_{tot} from (2.24). For the numerical continuation path, we hold τ fixed with its value at the bifurcation point and vary $\hat{\eta}_{0,1}$ with progressively larger values, increasing N_1 , N_2 , M_1 and M_2 as needed to maintain spectral accuracy. We stop when we run out of computational resources to further increase the problem size. Details will be given in Sections 4.1 and 4.2 below.

The Levenberg-Marquardt algorithm requires the evaluation of the Jacobian $\mathcal{J}_{ij} = \partial r_i/\partial p_j$, which can be carried out analytically or with finite differences. We take the analytical approach. Let us denote the Fréchet derivative of \mathcal{R} by

$$D_{q}\mathcal{R} = (D_{\eta}\mathcal{R}, D_{\tau}\mathcal{R}, D_{b}\mathcal{R}), \qquad q = (\eta, \tau, b), \tag{2.32}$$

and employ "dot notation" [6,90] for the variational derivative of a quantity at q in the \dot{q} direction:

$$\dot{\mathcal{R}}(q,\dot{q}) = D_q \mathcal{R}[q]\dot{q} = \frac{d}{d\varepsilon} \bigg|_{\varepsilon=0} \mathcal{R}[q + \varepsilon \dot{q}]. \tag{2.33}$$

We will not use a dot for time derivatives in this paper. Explicitly, we have

$$\dot{\mathcal{R}} = P \left[\frac{1}{2J} \dot{b} - \frac{b}{2J^2} \dot{J} + g \dot{\eta} - \tau \dot{\kappa} - \kappa \dot{\tau} \right],$$

$$\dot{\xi} = H [\dot{\eta}], \qquad \dot{J} = 2 \left\{ (1 + \partial_{\alpha} \xi) (\partial_{\alpha} \dot{\xi}) + (\partial_{\alpha} \eta) (\partial_{\alpha} \dot{\eta}) \right\},$$

$$\dot{\kappa} = -\frac{3\kappa}{2J} \dot{J} + \frac{1}{J^{3/2}} \left\{ (\partial_{\alpha}^{2} \eta) (\partial_{\alpha} \dot{\xi}) + (1 + \partial_{\alpha} \xi) (\partial_{\alpha}^{2} \dot{\eta}) - (\partial_{\alpha}^{2} \xi) (\partial_{\alpha} \dot{\eta}) - (\partial_{\alpha} \eta) (\partial_{\alpha}^{2} \dot{\xi}) \right\},$$
(2.34)

where η , ξ , J, κ , $\dot{\eta}$, $\dot{\xi}$, \dot{J} and $\dot{\kappa}$ are torus functions; b, τ , \dot{b} and $\dot{\tau}$ are scalars; and ξ represents only the quasi-periodic part of $\tilde{\xi}$, via (2.15). With these formulas, it is easy to evaluate the entries of the Jacobian

$$\mathcal{J}_{i,j} = \frac{\partial r_i}{\partial p_j} = \frac{\dot{R}(2\pi m_1/M_1, 2\pi m_2/M_2)}{\sqrt{M_1 M_2}}, \qquad 0 \leqslant i = m_2 M_1 + m_1 < M_1 M_2, \tag{2.35}$$

where m_1, m_2 are in the ranges (2.21) and j enumerates the entries of \vec{p} in (2.31). For example, j=0 corresponds to b, so one sets $\dot{q}=(\dot{\eta},\dot{\tau},\dot{b})=(0,0,1)$ in (2.34) to compute the zeroth column of \mathcal{J} via (2.35). Since τ is treated as a fixed parameter, we set $\dot{\tau}=0$ for each column of the Jacobian in the present work; however, in [91], τ is computed by the solver, just like b, so one of the Jacobian columns corresponds to $\dot{q}=(\dot{\eta},\dot{\tau},\dot{b})=(0,1,0)$. Each of the remaining columns corresponds to varying one of the Fourier mode degrees of freedom. Since we make use of the symmetry (2.14), these columns correspond to variations of the form

$$\dot{q}_{j_1,j_2} = \left(e^{i(j_1\alpha_1 + j_2\alpha_2)} + e^{-i(j_1\alpha_1 + j_2\alpha_2)}, 0, 0\right),\tag{2.36}$$

where j_1 and j_2 range over the values listed in (2.31) to enumerate columns 1 through ($N_{\text{tot}}-1$) of \mathcal{I} in a zero-based numbering convention. More details on the form of \dot{R} for variations of the form (2.36) will be given in Section 3 below. In

the periodic sub-problem, $\mathcal{J}_{i,j}$ in (2.35) is modified in the obvious way to account for the change from (2.25) to (2.30) and (2.31) to (2.27).

In the process of finding a bifurcation point q^{bif} from periodic to quasi-periodic traveling waves in Section 3 below, we will obtain a null vector \dot{q}^{qua} of $D_q \mathcal{R}[q^{\text{bif}}]$ that is transverse to the family of traveling waves. In the numerical continuation algorithm, we take the bifurcation point q^{bif} as the zeroth point on the path. The first point on the path, which, unlike the zeroth point, will be genuinely quasi-periodic, is obtained using the Levenberg-Marquardt algorithm with initial guess $q^{\text{bif}} + \varepsilon \dot{q}^{\text{qua}}$. Here ε is a suitably small number that we choose by trial and error to make progress in escaping the family of periodic waves while still resembling the zeroth solution. In the minimization, τ is held fixed with its value at the zeroth solution and $\hat{\eta}_{0,1}$ is held fixed with the value $\varepsilon \dot{\hat{\eta}}_{0,1}^{\text{qua}}$ (since $\hat{\eta}_{0,1}^{\text{bif}} = 0$). After the zeroth and first solution on the path are computed, we continue along a straight line through parameter space (the $(\hat{\eta}_{0,1}, \tau)$ -plane) using linear extrapolation for the initial guess for the next quasi-periodic solution. The straight line involves holding τ fixed and incrementing $\hat{\eta}_{0,1}$ for successive solutions. The increment is initially $\varepsilon \dot{\hat{\eta}}_{0,1}$, but can be changed adaptively, if needed. This numerical continuation strategy is easy to implement and requires only a few iterations to find quasi-periodic solutions that deviate significantly from the periodic solution at the bifurcation point as long as ε is chosen to be large enough to make progress along the path (but small enough for linear extrapolation to be effective).

3. Quasi-periodic bifurcations from periodic traveling waves

In [91], we compute small-amplitude quasi-periodic traveling waves that bifurcate from the zero-amplitude wave. In this section, we consider quasi-periodic bifurcations from finite-amplitude periodic traveling waves that can be far beyond the linear regime of the zero solution. In particular, we wish to study genuinely quasi-periodic traveling waves with zero surface tension, which do not exist at small amplitude.

Before discussing bifurcation theory, it is convenient to frame the problem in a Hilbert space setting. Recall that a torus function $\eta:\mathbb{T}^2\to\mathbb{C}$ is real-analytic if and only if (iff) it has a convergent power series in a neighborhood of each $\vec{\alpha}\in\mathbb{T}^2$. Equivalently [19,92], η is real-analytic iff its Fourier modes $\hat{\eta}_{j_1,j_2}$ in (2.6) decay exponentially, i.e., there exist positive constants C and σ such that $|\hat{\eta}_{j_1,j_2}|\leqslant Ce^{-\sigma(|j_1|+|j_2|)}$ for all $(j_1,j_2)\in\mathbb{Z}^2$. We follow the standard convention [56] that real-analytic functions can be complex-valued. Although η in (2.6) must be real-valued for (2.5) to make sense, it is useful to allow complex-valued torus functions when considering the effect of perturbations in Fourier space. Ultimately, linear combinations will be taken to keep the result real-valued. Similarly, while $b=c^2$ must be positive and τ must be nonnegative, perturbations of these quantities can have either sign, and can even be complex as long as linear combinations are eventually taken to make them real.

Definition 3.1. For $\sigma \geqslant 0$, let \mathcal{V}_{σ} be the Hilbert space of real-analytic torus functions of finite norm induced by the inner product

$$\langle f, g \rangle = \sum_{(j_1, j_2) \in \mathbb{Z}^2} \hat{f}_{j_1, j_2} \ \hat{g}_{j_1, j_2} \ e^{2\sigma(|j_1| + |j_2|)}. \tag{3.1}$$

We also define the subspaces

$$\mathcal{V}_{\sigma}^{(l)} = \{ f \in \mathcal{V}_{\sigma} : \hat{f}_{j_1, j_2} = 0 \text{ if } j_2 \neq l \}, \qquad (l \in \mathbb{Z}),
\mathcal{V}_{\sigma}^{\text{per}} = \mathcal{V}_{\sigma}^{(0)}, \qquad \mathcal{V}_{\sigma}^{\text{qua}} = (\mathcal{V}_{\sigma}^{\text{per}})^{\perp} = \bigoplus_{l \neq 0} \mathcal{V}_{\sigma}^{(l)}$$
(3.2)

and write, e.g., $(\mathcal{V}_{\sigma}^{(1)}, 0, \mathbb{C})$ and $(\mathcal{V}_{\sigma}^{\text{per}}, \mathbb{C}, \mathbb{C})$ as shorthand for $\{(f, 0, b) : f \in \mathcal{V}_{\sigma}^{(1)}, b \in \mathbb{C}\}$ and $\mathcal{V}_{\sigma}^{\text{per}} \times \mathbb{C}^2$, respectively, with the product Hilbert space norms.

Note that $\mathcal{V}^{\text{per}}_{\sigma}$ consists precisely of the torus functions $f(\alpha_1,\alpha_2)$ in \mathcal{V}_{σ} that do not depend on α_2 . We think of functions in $\mathcal{V}_{\sigma} \setminus \mathcal{V}^{\text{per}}_{\sigma}$ as being genuinely quasi-periodic even though this set includes functions $f(\alpha_1,\alpha_2)$ that are independent of α_1 . We adopt this viewpoint as our focus is on bifurcations from 2π -periodic traveling waves. The case of bifurcations from $(2\pi/k)$ -periodic traveling waves can be investigated within this framework by rescaling space by a factor of k to make the wavelength of these waves 2π , and then replacing k by 1/k as the second basic frequency.

3.1. Linearization about periodic traveling waves

Recall from (2.19) that the governing equations (2.9) for traveling water waves are equivalent to solving

$$\mathcal{R}[q] = P \left[\frac{b}{2I} + g\eta - \tau \kappa \right] = 0, \qquad q = (\eta, \tau, b), \tag{3.3}$$

where J and κ depend on η via (2.9). We computed the Fréchet derivative of \mathcal{R} in (2.34) using "dot notation," defined in (2.33). The following theorem is proved in Appendix B:

Theorem 3.2. Suppose $q^{per} = (\eta, \tau, b)$ with $\eta \in \mathcal{V}_{\sigma}^{per}$ for some $\sigma > 0$. Suppose also that η is real-valued and the resulting $J(\alpha_1, \alpha_2)$ in (2.9), which is independent of α_2 , is non-zero for every $\alpha_1 \in \mathbb{T}$. Then there exists $\rho \in (0, \sigma)$ such that $D_q \mathcal{R}[q^{per}]$ is a bounded operator from $(\mathcal{V}_{\sigma}, \mathbb{C}, \mathbb{C})$ to \mathcal{V}_{ρ} .

We do not assume q^{per} is a solution of $\mathcal{R}[q] = 0$ in this theorem, though that is the case of interest. Our next goal is to show that when linearized about a periodic solution, variations in (τ, b) and periodic perturbations of η lead to periodic changes in \mathcal{R} while quasi-periodic perturbations lead to quasi-periodic changes in \mathcal{R} . We combine the discussion of the numerical computation with the derivation since the only difference is whether infinite Fourier series of real analytic functions are considered or whether these functions are approximated via the FFT on a uniform grid.

Let $q^{\text{per}} = (\eta, \tau, b)$ satisfy the hypotheses of Theorem (3.2). Then clearly

$$D_q \mathcal{R}[q^{\text{per}}](0, \dot{\tau}, \dot{b}) = P[\dot{b}/(2J) - \kappa \dot{\tau}]$$
(3.4)

is periodic, i.e., a torus function independent of α_2 . Moreover, if \dot{q} is of the form

$$\dot{q}^{(l_1,l_2)} = (e^{il_1\alpha_1}e^{il_2\alpha_2}, 0, 0), \qquad l_1, l_2 \in \mathbb{Z}, \tag{3.5}$$

then (2.34) simplifies to

$$\dot{\mathcal{R}} = P \left[-\frac{b}{2J^{2}} \dot{J} + g \dot{\eta} - \tau \dot{\kappa} \right], \quad \dot{\eta} = e^{il_{1}\alpha_{1}} e^{il_{2}\alpha_{2}}, \quad \dot{\xi} = -i \operatorname{sgn}(l_{1} + kl_{2}) e^{il_{1}\alpha_{1}} e^{il_{2}\alpha_{2}},
\dot{J} = 2 \left\{ |l_{1} + kl_{2}| (1 + \partial_{\alpha}\xi) + i (l_{1} + kl_{2}) \partial_{\alpha} \eta \right\} e^{il_{1}\alpha_{1}} e^{il_{2}\alpha_{2}},
\dot{\kappa} = -\frac{3\kappa}{2J} \dot{J} + \frac{1}{J^{3/2}} \left\{ |l_{1} + kl_{2}| \partial_{\alpha}^{2} \eta - (l_{1} + kl_{2})^{2} (1 + \partial_{\alpha}\xi) - i (l_{1} + kl_{2}) (\partial_{\alpha}^{2}\xi + |l_{1} + kl_{2}| \partial_{\alpha}\eta) \right\} e^{il_{1}\alpha_{1}} e^{il_{2}\alpha_{2}}.$$
(3.6)

The terms in braces, which we denote by $\tilde{A}^{(1)}(\alpha_1)$ and $\tilde{A}^{(2)}(\alpha_1)$, respectively, are independent of α_2 . Next we expand $\tilde{\eta}(\alpha)$ in (2.8) as a 1d Fourier series, $\sum_i \hat{\eta}_j e^{ij\alpha}$, which gives

$$(1 + \partial_{\alpha}\xi) = 1 + \sum_{i} |j|\hat{\eta}_{j}e^{ij\alpha_{1}}, \quad \partial_{\alpha}^{r}\eta = \sum_{i} (ij)^{r}\hat{\eta}_{j}e^{ij\alpha_{1}}, \quad \partial_{\alpha}^{2}\xi = \sum_{i} ij|j|\hat{\eta}_{j}e^{ij\alpha_{1}},$$

$$(3.7)$$

where $r \in \{1, 2\}$. The 1d inverse FFT can then be used to compute $\tilde{A}^{(1)}(\alpha_1)$ and $\tilde{A}^{(2)}(\alpha_1)$ on a uniform grid in the α_1 variable that is fine enough to resolve the Fourier modes to the desired accuracy. We then write

$$\dot{\kappa}(\alpha_{1},\alpha_{2}) = \tilde{A}^{(3)}(\alpha_{1})e^{il_{1}\alpha_{1}}e^{il_{2}\alpha_{2}}, \qquad \tilde{A}^{(3)} = -3\frac{\kappa}{J}\tilde{A}^{(1)} + \frac{1}{J^{3/2}}\tilde{A}^{(2)},
-\frac{b}{2J^{2}}\dot{J} + g\dot{\eta} - \tau\dot{\kappa} = \tilde{A}^{(4)}(\alpha_{1})e^{il_{1}\alpha_{1}}e^{il_{2}\alpha_{2}}, \qquad \tilde{A}^{(4)} = -\frac{b}{J^{2}}\tilde{A}^{(1)} + g - \tau\tilde{A}^{(3)},$$
(3.8)

where $\tilde{A}^{(3)}(\alpha_1)$ and $\tilde{A}^{(4)}(\alpha_1)$ are computed pointwise on the grid. For each $m \in \{1, 2, 3, 4\}$, we note that $\tilde{A}^{(m)}(\alpha_1)$ depends on (l_1, l_2) , and will be written $\tilde{A}^{(l_1, l_2, m)}(\alpha_1)$ when the dependence needs to be shown explicitly. Finally, we obtain

$$(D_q \mathcal{R}[q^{\text{per}}] \dot{q}^{(l_1, l_2)})(\alpha_1, \alpha_2) = P[\tilde{A}^{(l_1, l_2, 4)}(\alpha_1) e^{il_1 \alpha_1} e^{il_2 \alpha_2}] = \tilde{u}^{(l_1, l_2)}(\alpha_1) e^{il_2 \alpha_2},$$
 (3.9)

where the projection P was defined in (2.10) above. The Fourier expansion

$$\tilde{u}^{(l_1,l_2)}(\alpha) = \sum_{j} \hat{u}_{j}^{(l_1,l_2)} e^{ij\alpha}, \qquad \hat{u}_{j}^{(l_1,l_2)} = \begin{cases} \hat{A}_{j-l_1}^{(l_1,l_2,4)}, & (j,l_2) \neq (0,0), \\ 0, & (j,l_2) = (0,0), \end{cases}$$
(3.10)

is easily read off from the FFT of $\tilde{A}^{(l_1,l_2,4)}(\alpha)$, where we used the fact that multiplication by $e^{il_1\alpha_1}$ in (3.9) simply shifts the Fourier index by l_1 . Of course, by Remark 2.3, $\hat{A}^{(l_1,l_2,4)}_{j-l_1}$ will be computed via a one-dimensional de-aliasing formula analogous to (2.22). Since τ and b are real and $\eta(\alpha_1,\alpha_2)=\tilde{\eta}(\alpha_1)$ is real-valued, inspection of (3.6)–(3.9) shows that

$$\tilde{A}^{(-l_1, -l_2, m)}(\alpha) = \overline{\tilde{A}^{(l_1, l_2, m)}(\alpha)}, \qquad \tilde{u}^{(-l_1, -l_2)}(\alpha) = \overline{\tilde{u}^{(l_1, l_2)}(\alpha)}, \qquad \binom{m = 1, 2, 3, 4}{l_1, l_2 \in \mathbb{Z}}.$$
(3.11)

This shows that $D_q \mathcal{R}[q^{\text{per}}] \overline{\dot{q}^{(l_1,l_2)}} = \overline{D_q \mathcal{R}[q^{\text{per}}] \dot{q}^{(l_1,l_2)}}$, which is also evident from (3.6). If, moreover, η has even symmetry, then

$$\tilde{A}^{(l_1, l_2, m)}(-\alpha) = \overline{\tilde{A}^{(l_1, l_2, m)}(\alpha)}, \qquad \tilde{u}^{(l_1, l_2)}(-\alpha) = \overline{\tilde{u}^{(l_1, l_2)}(\alpha)}, \qquad \binom{m = 1, 2, 3, 4}{l_1, l_2 \in \mathbb{Z}},$$
(3.12)

which implies that the Fourier coefficients of these complex-valued functions are real.

Remark 3.3. Evaluation of (3.6) and (3.9) along the characteristic line $\alpha_1 = \alpha$, $\alpha_2 = k\alpha$ gives the real-line version of these equations, which can be derived directly via a Fourier-Bloch analysis commonly used in the study of subharmonic stability of traveling waves [29,80]. However, by posing the problem in a quasi-periodic torus framework, it becomes possible to follow bifurcation branches beyond linearization about periodic traveling waves.

Remark 3.4. In summary, we have shown that $D_q \mathcal{R}[q^{\text{per}}]$ has a block structure, mapping $(\dot{\eta}, \dot{\tau}, \dot{b}) \in (\mathcal{V}_{\sigma}^{\text{per}}, \mathbb{C}, \mathbb{C})$ to $\mathcal{V}_{\rho}^{\text{per}}$ and $(\dot{\eta}, 0, 0) \in (\mathcal{V}_{\sigma}^{(l_2)}, 0, 0)$ to $\mathcal{V}_{\rho}^{(l_2)}$ for $l_2 \in \mathbb{Z} \setminus \{0\}$.

Remark 3.5. The spaces V_{σ} are convenient for identifying the block structure of $D_q \mathcal{R}[q^{\text{per}}]$, which leads us to a numerical algorithm for computing quasi-periodic bifurcation points and perturbation directions to switch to the new branch; however, we are not able to apply rigorous bifurcation theorems such as the Crandall-Rabinowitz theorem [27] to prove existence of genuinely spatially quasi-periodic water waves in this framework since $D_q \mathcal{R}[q^{\text{per}}]$ is not a Fredholm operator from $(\mathcal{V}_{\sigma}, \mathbb{C}, \mathbb{C})$ to \mathcal{V}_{ρ} . Indeed, when ρ and σ are chosen as in the proof of Theorem B.1 in Appendix B, the algebraic codimension is infinite since $D_q \mathcal{R}[q^{\text{per}}]$ is also bounded if the range is decreased slightly to $\mathcal{V}_{\rho+\varepsilon}$ for sufficiently small ε , and the embedding of $\mathcal{V}_{\rho+\varepsilon}$ into \mathcal{V}_{ρ} has infinite algebraic co-dimension. Proofs of existence [20,21,81] of bifurcations from 2π -periodic traveling waves to $2\pi m$ -periodic traveling waves for sufficiently large integers m employ a variant of Nekrasov's equation [66] instead of (3.3) for the governing equations. Adapting these proofs to the quasi-periodic case is an interesting avenue of future research, and may require employing Nash-Moser theory [10,12,13,69] to overcome small divisors, whose effects can be seen in the numerical results presented in Section 4.1 below.

It is convenient at this point to introduce alternative basis functions and subspaces that more clearly exhibit the even, real-valued nature of the solutions we seek. Let

$$\varphi_{\vec{l}}(\vec{\alpha}) = 2\cos(\vec{l} \cdot \vec{\alpha}),
\psi_{\vec{l}}(\vec{\alpha}) = -2\sin(\vec{l} \cdot \vec{\alpha}),$$

$$\vec{l} \in \Lambda = \left\{ (l_1, l_2) \in \mathbb{Z}^2 : l_2 > 0 \text{ or } (l_2 = 0 \text{ and } l_1 > 0) \right\},$$
(3.13)

where $\vec{\alpha}=(\alpha_1,\alpha_2)$. We also define $\varphi_{0,0}(\vec{\alpha})=1$. Then

$$\left(\varphi_{\vec{l}}(\vec{\alpha}), \psi_{\vec{l}}(\vec{\alpha})\right) = \left(e^{i\vec{l}\cdot\vec{\alpha}}, e^{-i\vec{l}\cdot\vec{\alpha}}\right) \begin{pmatrix} 1 & i \\ 1 & -i \end{pmatrix}, \qquad (\vec{l} \in \Lambda)$$
(3.14)

and the torus function expansions of an arbitrary function

$$f(\vec{\alpha}) = \sum_{j_1, j_2} \hat{f}_{j_1, j_2} e^{i(j_1 \alpha_1 + j_2 \alpha_2)} = a_{\vec{0}} \varphi_{\vec{0}}(\vec{\alpha}) + \sum_{\vec{l} \in \Lambda} \left(a_{\vec{l}} \varphi_{\vec{l}}(\vec{\alpha}) + b_{\vec{l}} \psi_{\vec{l}}(\vec{\alpha}) \right)$$
(3.15)

are related by

$$a_{\vec{0}} = \hat{f}_{\vec{0}}, \quad \begin{pmatrix} a_{\vec{l}} \\ b_{\vec{l}} \end{pmatrix} = \begin{pmatrix} \frac{1}{2} & \frac{1}{2} \\ \frac{1}{2i} & \frac{-1}{2i} \end{pmatrix} \begin{pmatrix} \hat{f}_{\vec{l}} \\ \hat{f}_{-\vec{l}} \end{pmatrix}, \quad \begin{pmatrix} \hat{f}_{\vec{l}} \\ \hat{f}_{-\vec{l}} \end{pmatrix} = \begin{pmatrix} 1 & i \\ 1 & -i \end{pmatrix} \begin{pmatrix} a_{\vec{l}} \\ b_{\vec{l}} \end{pmatrix}, \quad (\vec{l} \in \Lambda).$$
 (3.16)

Note that $f(\vec{\alpha})$ is real-valued precisely when all the $a_{\vec{l}}$ and $b_{\vec{l}}$ are real. In this case, these coefficients are the real and imaginary parts of $\hat{f}_{\vec{l}}$ for $\vec{l} \in \Lambda$, and $\hat{f}_{-\vec{l}} = \overline{\hat{f}_{\vec{l}}}$. Similarly, $f(\vec{\alpha})$ is even with respect to $\vec{\alpha} \in \mathbb{T}^2$ precisely when all the $b_{\vec{l}}$ are zero. We also define the subspaces

$$\begin{split} & \mathcal{X}_{\sigma}^{\text{const}} = \text{span}_{\sigma}\{\varphi_{0,0}\} = \{ \text{constant functions on } \mathbb{T}^2 \}, \\ & \mathcal{X}_{\sigma}^{\text{per}} = \mathcal{X}_{\sigma}^{(0)} = \text{span}_{\sigma}\{\varphi_{l_1,0} : l_1 \geqslant 1 \}, \qquad \mathcal{Y}_{\sigma}^{\text{per}} = \mathcal{Y}_{\sigma}^{(0)} = \text{span}_{\sigma}\{\psi_{l_1,0} : l_1 \geqslant 1 \}, \\ & \mathcal{X}_{\sigma}^{(l_2)} = \text{span}_{\sigma}\{\varphi_{l_1,l_2} : l_1 \in \mathbb{Z} \}, \qquad \mathcal{Y}_{\sigma}^{(l_2)} = \text{span}_{\sigma}\{\psi_{l_1,l_2} : l_1 \in \mathbb{Z} \}, \qquad (l_2 \geqslant 1), \end{aligned}$$

where $\operatorname{span}_{\sigma}$ of a list of functions is the closure of the set of finite linear combinations of the functions with respect to the \mathcal{V}_{σ} norm from (3.1). We note that

$$\mathcal{V}_{\sigma}^{\text{per}} = \mathcal{X}_{\sigma}^{\text{const}} \oplus \mathcal{X}_{\sigma}^{\text{per}} \oplus \mathcal{Y}_{\sigma}^{\text{per}}, \qquad \mathcal{V}_{\sigma}^{(l_2)} \oplus \mathcal{V}_{\sigma}^{(-l_2)} = \mathcal{X}_{\sigma}^{(l_2)} \oplus \mathcal{Y}_{\sigma}^{(l_2)}, \quad (l_2 \geqslant 1), \tag{3.18}$$

$$\mathcal{V}_{\sigma} = \mathcal{X}_{\sigma}^{\text{const}} \oplus \mathcal{X}_{\sigma}^{\text{per}} \oplus \mathcal{Y}_{\sigma}^{\text{per}} \oplus \mathcal{X}_{\sigma}^{\text{qua}} \oplus \mathcal{Y}_{\sigma}^{\text{qua}}, \qquad \mathcal{X}_{\sigma}^{\text{qua}} = \bigoplus_{l_{2}=1}^{\infty} \mathcal{X}_{\sigma}^{(l_{2})}, \tag{3.19}$$

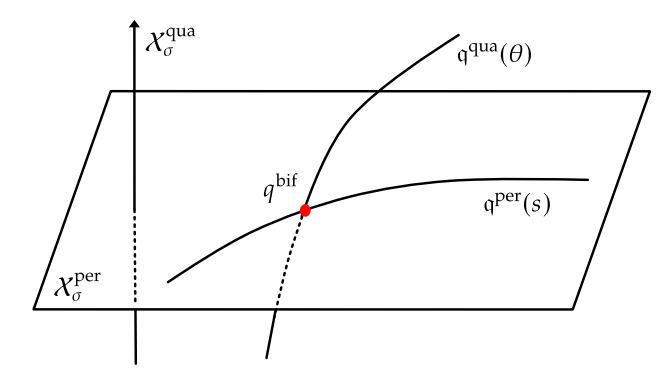


Fig. 1. Simple quasi-periodic bifurcation diagram.

with a similar formula for $\mathcal{Y}^{\text{qua}}_{\sigma}$. Since the basis functions $\varphi_{\tilde{l}}(\vec{\alpha})$ and $\psi_{\tilde{l}}(\vec{\alpha})$ are real-valued, the spaces in (3.19) may be regarded as complex or real Hilbert spaces. It is also useful to define

$$\mathcal{X}_{\sigma} = \mathcal{X}_{\sigma}^{\text{per}} \oplus \mathcal{X}_{\sigma}^{\text{qua}},$$
 (3.20)

which contains the even functions of V_{σ} of zero mean on \mathbb{T}^2 .

As explained above, since we assume in (2.14) that η is real-valued and even, the Fourier coefficients of $\tilde{u}^{(l_1,l_2)}(\alpha)$ in (3.10) are real. Thus, from (3.9) and (3.11) we have

$$D_{q} \mathcal{R}[q^{\text{per}}](\varphi_{\tilde{l}}, 0, 0) = \sum_{j_{1} \in \mathbb{Z}} \hat{u}_{j_{1}}^{(l_{1}, l_{2})} \varphi_{j_{1}, l_{2}}(\vec{\alpha}),$$

$$D_{q} \mathcal{R}[q^{\text{per}}](\psi_{\tilde{l}}, 0, 0) = \sum_{j_{1} \in \mathbb{Z}} \hat{u}_{j_{1}}^{(l_{1}, l_{2})} \psi_{j_{1}, l_{2}}(\vec{\alpha}),$$

$$(\vec{l} = (l_{1}, l_{2}) \in \Lambda).$$
(3.21)

The $j_1=0$ term can be omitted from these sums when $l_2=0$ since $\hat{u}_0^{(l_1,0)}=0$, and must be omitted in the second formula as $\psi_{0,0}(\vec{\alpha})$ is not defined. We also see directly from (3.4) and (3.6) that $D_q \mathcal{R}[q^{\mathrm{per}}](0,\dot{\tau},\dot{b})$ is an even function and $D_q \mathcal{R}[q^{\mathrm{per}}](\varphi_{0,0},0,0)=0$.

Remark 3.6. Since η is assumed real-valued and even and $D_q \mathcal{R}[q^{\text{per}}]$ maps even perturbations to even functions and odd perturbations to odd functions, we can restrict attention to even functions and perturbations. In light of Remark 2.1 and the presence of the projection P in the definition (3.3) of \mathcal{R} , we may further restrict attention to functions and perturbations of zero mean. It follows from (3.21) that $D_q \mathcal{R}[q^{\text{per}}]$ has a block structure with respect to the decomposition (3.20), mapping $(\dot{\eta}, \dot{\tau}, \dot{b}) \in (\chi_{\sigma}^{\text{per}}, \mathbb{R}, \mathbb{R})$ to χ_{ρ}^{per} and $(\dot{\eta}, 0, 0) \in (\chi_{\sigma}^{(l_2)}, 0, 0)$ to $\chi_{\rho}^{(l_2)}$ for $l_2 \geqslant 1$.

If the surface tension τ is held fixed, which will be the case for the pure gravity wave problem in section 4.1 below, then there will be a one-parameter "primary" branch of periodic traveling waves, which we denote by $q=\mathfrak{q}^{\mathrm{per}}(s)\in(\mathcal{X}_{\sigma}^{\mathrm{per}},\mathbb{R},\mathbb{R})$. Here s is any convenient amplitude parameter such as $\hat{\eta}_{1,0}$ or the crest-to-trough height of the wave, $h=\tilde{\eta}(0)-\tilde{\eta}(\pi)$. Following [4,23,24,27,95], we are interested in finding simple bifurcation points q^{bif} where a second solution curve $q=\mathfrak{q}^{\mathrm{qua}}(\theta)\in(\mathcal{X}_{\sigma},\mathbb{R},\mathbb{R})$ intersects the first non-tangentially, with θ another amplitude parameter such as $\hat{\eta}_{0,1}$; see Fig. 1. Suppose such an intersection occurs at $s=s_0$ and $\theta=\theta_0$. Differentiating $\mathfrak{R}[\mathfrak{q}^{\mathrm{per}}(s)]=0$ and $\mathfrak{R}[\mathfrak{q}^{\mathrm{qua}}(\theta)]=0$, we obtain

$$D_q \mathcal{R}[q^{\text{bif}}] \Big((\mathfrak{q}^{\text{per}})'(s_0) \Big) = 0 = D_q \mathcal{R}[q^{\text{bif}}] \Big((\mathfrak{q}^{\text{qua}})'(\theta_0) \Big). \tag{3.22}$$

At a simple bifurcation [27], these null vectors span the kernel of $D_q \mathcal{R}[q^{\text{bif}}]$,

$$\ker D_q \mathcal{R}[q^{\text{bif}}] = \operatorname{span} \left\{ \left(q^{\text{per}} \right)'(s_0), \left(q^{\text{qua}} \right)'(\theta_0) \right\}. \tag{3.23}$$

Because τ is frozen and we restrict attention to even perturbations of zero mean, the domain of $D_q \mathcal{R}[q^{\text{bif}}]$ is taken to be $\mathcal{D}_{\sigma} = (X_{\sigma}, 0, \mathbb{R})$ when computing the kernel. We decompose

$$\mathcal{D}_{\sigma} = \mathcal{D}_{\sigma}^{\text{per}} \oplus \left(\bigoplus_{l=1}^{\infty} \mathcal{D}_{\sigma}^{(l)} \right), \qquad \mathcal{D}_{\sigma}^{\text{per}} = \{ (\dot{\eta}, 0, \dot{b}) : \dot{\eta} \in \mathcal{X}_{\sigma}^{\text{per}}, \dot{b} \in \mathbb{R} \}, \\ \mathcal{D}_{\sigma}^{(l)} = \{ (\dot{\eta}, 0, 0) : \dot{\eta} \in \mathcal{X}_{\sigma}^{(l)} \}.$$

$$(3.24)$$

Let $\dot{q}^{per} = (q^{per})'(s_0)$, which belongs to $\mathcal{D}^{per}_{\sigma}$ since solutions on this branch are periodic. By (3.24), we can decompose $(q^{qua})'(\theta_0) = \dot{q}_1^{per} + \sum_{l=1}^{\infty} \dot{q}^{(l)}$ with $\dot{q}_1^{per} \in \mathcal{D}^{per}_{\sigma}$ and $\dot{q}^{(l)} \in \mathcal{D}^{(l)}_{\sigma}$. Our assumption that the bifurcation is simple implies that

precisely one of the $\dot{q}^{(l)}$ is non-zero. In more detail, because $D_q \mathcal{R}[q^{\mathrm{bif}}]$ has a block structure, each non-zero component \dot{q}_1^{per} and $\dot{q}^{(l)}$ will also be in the kernel. At least one of the $\dot{q}^{(l)}$, say with $l=l_0$, must be non-zero since solutions on the path $q^{\mathrm{qua}}(\theta)$ are supposed to be genuinely quasi-periodic, and we require that this occurs at linear order in the perturbation. But then all the other $\dot{q}^{(l)}$ must be zero and \dot{q}_1^{per} must be a multiple of \dot{q}^{per} , or else the dimension of $\ker D_q \mathcal{R}[q^{\mathrm{bif}}]$ would be greater than two. For simplicity, and without loss of generality, we may assume $l_0=1$. Indeed, observing the way k and l_2 appear in the formulas of (3.6), we see that if $\dot{q}^{(l)}$ belongs to the kernel for l>1, then $\dot{q}^{(1)}$ will be in the kernel for an auxiliary problem with k replaced by kl. Renaming $\dot{q}^{(1)}$ by \dot{q}^{qua} , we have shown that the kernel should take the form

$$\ker D_{a} \mathcal{R} [q^{\text{bif}}] = \operatorname{span} \{ \dot{q}^{\text{per}}, \dot{q}^{\text{qua}} \}, \qquad \dot{q}^{\text{per}} \in \mathcal{D}_{\sigma}^{\text{per}}, \qquad \dot{q}^{\text{qua}} \in \mathcal{D}_{\sigma}^{(1)}, \tag{3.25}$$

where $(q^{per})'(s_0) = \dot{q}^{per}$ and $(q^{qua})'(\theta_0) = C\dot{q}^{per} + \dot{q}^{qua}$ for some $C \in \mathbb{R}$. As explained in Section 4.1 below, a non-zero value of C would break a symmetry that arises on the solution branches we have found. Thus, C turns out to be zero and $q^{bif} + \varepsilon \dot{q}^{qua}$ can be used as a natural initial guess to switch from the periodic branch to the quasi-periodic branch, where ε is a suitably small number chosen empirically.

When the surface tension is allowed to vary, which will be the case in the gravity-capillary wave problem of section 4.2, there will be a two-parameter family of periodic traveling waves that contains one-dimensional bifurcation curves where the periodic waves intersect with two-dimensional sheets of quasi-periodic traveling waves. In this formulation, one can increase the domain of $D_q \mathcal{R}[q^{\text{bif}}]$ from (3.24) to $\mathcal{D}_{\sigma} = (\chi_{\sigma}, \mathbb{R}, \mathbb{R})$ and the dimension of the kernel will increase from two to three. But computationally, we can sweep through these manifolds of solutions with τ or an amplitude parameter fixed, which reduces the problem to searching for isolated bifurcation points along one-parameter solution curves, as described above. The general theory of multi-parameter bifurcation theory is presented in [3,9], for example.

Remark 3.7. If we had not separated $\mathcal{X}_{\sigma}^{\text{const}}$ from $\mathcal{X}_{\sigma}^{\text{per}}$ in (3.17), the dimension of the manifolds of solutions would increase by one, as would the kernel, but in a trivial way: one can add a constant to η for any of the solutions to obtain another solution. One could add an equation to the nonlinear system $\mathcal{R}[q] = 0$ to select the physical solution with zero mean in physical space, but it is simpler to just hold $\hat{\eta}_{0,0} = 0$ in this search phase of the problem and compute the correction afterwards, as explained in Remark 2.1.

3.2. Detecting quasi-periodic bifurcation points

In this section, we discuss how to detect quasi-periodic bifurcation points on $\mathfrak{q}^{\mathrm{per}}(s)$ and compute the corresponding bifurcation directions. Because we seek bifurcation points q^{bif} such that $D_q \mathcal{R}[q^{\mathrm{bif}}]$ has a null vector $\dot{q}^{\mathrm{qua}} \in \mathcal{D}_{\sigma}^{(1)}$, it suffices to compute the restriction of $D_q \mathcal{R}[\mathfrak{q}^{\mathrm{per}}(s)]$ to $\mathcal{D}_{\sigma}^{(1)} = (\chi_{\sigma}^{(1)}, 0, 0)$ and search for values of s for which this operator has a non-trivial kernel. By Remark 3.6, the range of this restriction may be taken to be $\chi_{\sigma}^{(1)}$.

Recall from Section 2.2 that we compute periodic traveling waves numerically by specifying $\hat{\eta}_{1,0}$ and τ as given parameters and minimizing the objective function (2.30) to find the square of the wave speed, $b=c^2$, and the remaining leading Fourier modes $(\hat{\eta}_{2,0},\ldots,\hat{\eta}_{N_1,0})$. The computations are done on a uniform M_1 -point grid in the α_1 variable, where $M_1\approx 3N_1$ is generally sufficient to achieve spectrally accurate solutions with minimal effects of aliasing errors. Fourier modes $\hat{\eta}_{j_1,0}$ with $|j_1|>N_1$ are taken to be zero, and η is assumed real and even so that $\hat{\eta}_{-j_1,0}=\hat{\eta}_{j_1,0}\in\mathbb{R}$. N_1 is chosen large enough that the Fourier modes decay to machine precision by the time $|j_1|$ reaches N_1 .

For each of these computed periodic solutions, $q^{\mathrm{per}}=q^{\mathrm{per}}(s)$, we form the matrix $\mathcal{I}^{\mathrm{qua}}[q^{\mathrm{per}}]$ representing the restriction

For each of these computed periodic solutions, $q^{\text{per}} = q^{\text{per}}(s)$, we form the matrix $\mathcal{I}^{\text{qua}}[q^{\text{per}}]$ representing the restriction of $D_q \mathcal{R}[q^{\text{per}}]$ to $\mathcal{D}_{\sigma}^{(1)}$, using the $\{\varphi_{l_1,1}\}$ basis in both the domain and range of the restricted operator, up to a cutoff frequency N. We order the basis functions via $l_1 = (0, 1, -1, 2, -2, 3, -3, \dots, N, -N)$ and use (3.21) to obtain

$$\mathcal{I}^{\text{qua}}\left[q^{\text{per}}\right] = \begin{pmatrix} \hat{u}_{0}^{(0,1)} & \hat{u}_{0}^{(1,1)} & \hat{u}_{0}^{(-1,1)} & \cdots & \hat{u}_{0}^{(N,1)} & \hat{u}_{0}^{(-N,1)} \\ \hat{u}_{1}^{(0,1)} & \hat{u}_{1}^{(1,1)} & \hat{u}_{1}^{(-1,1)} & \cdots & \hat{u}_{1}^{(N,1)} & \hat{u}_{1}^{(-N,1)} \\ \hat{u}_{1}^{(0,1)} & \hat{u}_{1}^{(1,1)} & \hat{u}_{-1}^{(-1,1)} & \cdots & \hat{u}_{-1}^{(N,1)} & \hat{u}_{-1}^{(-N,1)} \\ \vdots & \vdots & \vdots & & \vdots & \vdots \\ \hat{u}_{N}^{(0,1)} & \hat{u}_{N}^{(1,1)} & \hat{u}_{N}^{(-1,1)} & \cdots & \hat{u}_{N}^{(N,1)} & \hat{u}_{N}^{(-N,1)} \\ \hat{u}_{N}^{(0,1)} & \hat{u}_{N}^{(1,1)} & \hat{u}_{N}^{(-1,1)} & \cdots & \hat{u}_{N}^{(N,1)} & \hat{u}_{N}^{(-N,1)} \\ \hat{u}_{-N}^{(0,1)} & \hat{u}_{-N}^{(1,1)} & \hat{u}_{-N}^{(-1,1)} & \cdots & \hat{u}_{-N}^{(N,1)} & \hat{u}_{-N}^{(-N,1)} \end{pmatrix},$$

$$(3.26)$$

where $\tilde{u}^{(l_1,l_2)}(\alpha_1)$ is defined above, in (3.9), and a formula for its Fourier modes $\hat{u}_j^{(l_1,l_2)}$ is given in (3.10). We generally choose N in the range $N_1 \leqslant N \leqslant (3/2)N_1$. The goal is to have enough rows and columns in \mathcal{I}^{qua} that when the singular value decomposition

$$\mathcal{I}^{\text{qua}}[\mathfrak{q}^{\text{per}}(s)] = U(s)\Sigma(s)V(s)^{T}, \qquad \Sigma(s) = \text{diag}\left(\sigma_{1}(s), \sigma_{2}(s), \dots, \sigma_{2N+1}(s)\right)$$
(3.27)

is computed, the left and right singular vectors corresponding to the smallest singular value have expansions in the $\{\varphi_{l,1}\}$ basis with coefficients $\{a_{l,1}\}$ that decay in amplitude to machine precision by the time |l| reaches N. Here the singular values

 $\sigma_i(s)$ are not related to the parameter σ in the weighted spaces \mathcal{V}_{σ} , \mathcal{D}_{σ} and \mathcal{X}_{σ} . Our reasons for using the unweighted Fourier basis $\{\varphi_{l_1,1}\}$ when computing the matrix representation of $D_q \mathcal{R}[q^{\text{per}}]$ from $\mathcal{D}_{\sigma}^{(1)}$ to $\mathcal{X}_{\rho}^{(1)}$ are explained in Remark 3.12 below.

Because this is a discretization of an infinite-dimensional problem, the smallest singular values are of physical interest while the largest are under-resolved and inaccurately computed. Thus, we order the singular values in *ascending order*

$$0 \leqslant \sigma_1(s) \leqslant \sigma_2(s) \leqslant \dots \leqslant \sigma_{2N+1}(s). \tag{3.28}$$

Increasing N further does not change the smallest singular values and corresponding singular vectors (up to floating-point arithmetic effects) as they are already fully resolved without using the high-frequency columns and rows of \mathcal{I}^{qua} that are added. Standard computational routines, of course, return them in descending order. But for this discussion, we reverse the columns of U(s) and the rows of $V(s)^T$ from the computation to match the convention (3.28). In the end, the matrices U(s) and $V(s)^T$ do not have to be computed at all; see Section 3.3.

As the parameter s changes, we compute $\Sigma(s)$ in (3.27) and search for zeros s_0 of the smallest singular value, $\sigma_1(s_0) = 0$. Since singular values are returned as non-negative quantities, $\sigma_1(s)$ has a slope discontinuity at each of its zeros. This is a challenge for root-finding algorithms that rely on bracketing or polynomial approximation. But if the matrix entries of g^{qua} depend analytically on s, there is an analytic SVD in which the singular values and vectors are analytic functions of s; see Bunse-Gerstner et al. [22] and Kato ([53], pp. 120–122, 392–393). If \mathcal{I}^{qua} is not analytic with respect to s, a smooth SVD [34] often exists and can be used instead. When the SVD is computed numerically, instead of changing the sign of $\sigma_1(s)$ when s crosses s_0 , the corresponding left or right singular vector will change sign. If we transfer this sign change to $\sigma_1(s)$, the slope discontinuity is eliminated and $\sigma_1(s)$ becomes analytic or smooth.

One idea we experimented with is to multiply $\sigma_1(s)$ by $\operatorname{sgn}(\langle u_1, v_1 \rangle)$, where u_1 and v_1 are the first columns of U and V in (3.27) under the convention (3.28); $\operatorname{sgn}(a)$ is defined above in (2.11); and $\langle u, v \rangle = \sum_j u^j v^j$, where we use superscripts for the components of a column vector that has been extracted from a matrix. If $u_1(s_0)$ and $v_1(s_0)$ are nearly orthogonal, one can instead use $\operatorname{sgn}(\langle Tu_1, v_1 \rangle)$, where T is a Householder reflection that aligns $u_1(s_1)$ with $v_1(s_1)$ at some point s_1 near s_0 . Although this works fine in the present problem (even without introducing T), it is clear that in general, $\langle Tu_1, v_1 \rangle$ might change discontinuously if $\sigma_1(s)$ and $\sigma_2(s)$ ever cross, possibly leading to a sign change that does not correspond to a zero crossing of $\sigma_1(s)$.

We propose, instead, to use the signs of the determinants of U and V to track orientation changes in the singular vectors when s crosses a zero of $\sigma_1(s)$. So we define

$$\chi(s) = \operatorname{sgn} \left(\det U(s) \right) \operatorname{sgn} \left(\det V(s) \right) \sigma_1(s)$$

$$= \left(\operatorname{sgn} \det \mathcal{I}^{\operatorname{qua}} \left[\mathfrak{q}^{\operatorname{per}}(s) \right] \right) \sigma_1(s). \tag{3.29}$$

The zeros s_0 of $\chi(s)$ will be used to identify bifurcation points $q^{\text{bif}} = q^{\text{per}}(s_0)$. Since U(s) and V(s) are orthogonal, their determinants are equal to 1 or -1 and can be computed accurately by LU or QR factorization to determine which. (Including sgn just rounds the numerical result to the exact value). The second formula of (3.29) has to be treated with care, but can be computed faster than the first formula as an intermediate step of computing $\sigma_1(s)$, without having to actually form the matrices U(s) or V(s) or compute their determinants; see Section 3.3.

To find a zero s_0 of $\chi(s)$, we can use a root bracketing technique such as Brent's method [17] to reduce $|\chi(s)|$ to the point that floating-point errors corrupt the smallest singular value of the SVD algorithm, which is typically below 10^{-13} in double-precision. Alternatively, one can compute $\chi(s)$ at a set of Chebyshev nodes on an interval $[s_1, s_2]$ for which $\chi(s_1)$ and $\chi(s_2)$ have opposite signs. One can then use Newton's method or Brent's method on the Chebyshev interpolation polynomial to find a zero s_0 of $\chi(s)$. We demonstrate both techniques in Section 4 below. Once $q^{\text{bif}} = \mathfrak{q}^{\text{per}}(s_0)$ has been found, the null vector \dot{q}^{qua} in (3.25) is given by

$$\dot{q}^{\text{qua}} = (\dot{\eta}^{\text{qua}}, 0, 0), \qquad \dot{\eta}^{\text{qua}} = v^1 \varphi_{0,1} + \sum_{j=1}^{N} \left[v^{2j} \varphi_{j,1} + v^{2j+1} \varphi_{-j,1} \right] = \sum_{j=-N}^{N} a_{j,1} \varphi_{j,1}, \tag{3.30}$$

where $v = v_1$ is the first column of V and we make use of the row and column ordering of \mathcal{I}^{qua} in (3.26). Here $a_{0,1} = v^1$, $a_{j,1} = v^{2j}$ and $a_{-j,1} = v^{2j+1}$ for $1 \le j \le N$. Since V is orthogonal, $||v_1|| = 1$, so \dot{q}^{qua} is already normalized sensibly and $q^{\text{bif}} + \varepsilon \dot{q}^{\text{qua}}$ serves as a useful initial guess for computing solutions on the secondary branch $q^{\text{qua}}(\theta)$. The null vector only needs to be computed when $s = s_0$ is a zero of $\chi(s)$, and can be computed efficiently without forming U(s) or the other columns of V(s) if the problem size is large enough to make these calculations expensive; see Section 3.3.

Remark 3.8. An important feature of $\chi(s)$ is that once N is large enough that the left and right singular vectors u_1 and v_1 have entries that decay to zero in floating-point arithmetic, further increases in N do not change the numerical value of $\chi(s)$.

To explain Remark 3.8, we first consider the zero-amplitude case. Setting $\eta=0$, $\xi=0$, J=1 and $\kappa=0$ in (3.6), we find that

$$\hat{u}_{j}^{(l_{1},l_{2})} = \begin{cases} -b|l_{1} + kl_{2}| + g + \tau(l_{1} + kl_{2})^{2}, & j = l_{1}, \\ 0, & \text{otherwise.} \end{cases}$$
(3.31)

Thus, \mathcal{J}^{qua} in (3.26) is diagonal, and the last two diagonal entries are

$$\mathcal{I}_{2N,2N}^{\text{qua}} = (1 - \tau | N + k |)(1 - | N + k |),$$

$$\mathcal{I}_{2N+1,2N+1}^{\text{qua}} = (1 - \tau | - N + k |)(1 - | - N + k |),$$
(3.32)

where we used $b=c^2=(g/k_1)+\tau k_1$ for the square of the wave speed of the zero-amplitude traveling wave of dimensionless wave number $k_1=1$ and gravitational acceleration g=1. Assuming k>0 and N>k+1, we have $1-|\pm N+k|\leqslant 1-(N-k)<0$, so both of these final diagonal entries are negative if $\tau=0$. If $\tau>0$, then both diagonal entries will be positive once $\tau N>\tau k+1$ and N>k+1. Thus, with or without surface tension, once N is large enough, increasing N by one does not change the sign of the determinant of \mathcal{I}^{qua} in the linearization about $\eta=0$. With N fixed, because an analytic SVD of the form (3.27) exists, the sign of $\det \mathcal{I}^{\text{qua}}$ [q^{per}(s)] will only change when s passes through a zero of $\chi(s)$, which is the signed version of the smallest singular value $\sigma_1(s)$. If such zero crossings correspond to well-resolved singular vectors in the kernel and N_1 and N_2 are large enough, then upon replacing $N=N_1$ by $N=N_2$, the same crossings will be encountered and the sign of the determinant at a given s will not change. This argument would break down if truncating the matrix leads to a spurious null vector at some s for either N_1 or N_2 , but we find that only the large singular values are sensitive to where the matrix is truncated. When a null vector is found, it is easy to check s-posteriori that the entries s-part of s-par

Remark 3.9. In finite-dimensional bifurcation problems, say $f(q) = 0 \in \mathbb{R}^n$ with $q = (u, s) \in \mathbb{R}^{n+1}$ and primary branch parameterized by q = q(s), one can use

$$\det \mathcal{J}^{e}(s), \qquad \mathcal{J}^{e}(s) = \begin{pmatrix} f_{q}[q(s)] \\ q'(s)^{T} \end{pmatrix}$$
(3.33)

as a test function that changes sign at simple bifurcations. This is the numerical approach advocated in [4], for example, and is one of the test functions implemented in MATCONT [16,33]. In our case, using Bloch's theorem, we only have to consider quasi-periodic perturbations $\dot{q} \in \mathcal{D}_{\sigma}^{(l_2)}$ with $l_2 = 1$, so we can replace $\det \mathcal{J}^e(s)$ above by $\det \mathcal{J}^{\text{qua}}[\mathfrak{q}^{\text{per}}(s)]$ in (3.26). The most common way to compute the determinant is as the product of the diagonal entries of the LU factorization. But these products can be very large or very small, potentially leading to overflow or underflow in floating-point arithmetic, and it is difficult to know what order of magnitude of the determinant constitutes a zero crossing. One can look for zeros among the diagonal entries of the LU factorization, but there are many cases where a nearly singular matrix has diagonal entries all bounded away from zero. For example, the bidiagonal matrix with 1's on the diagonal and 2's on the superdiagonal has unit determinant but is effectively singular once the matrix size exceeds 50. Moreover, unlike our $\chi(s)$ function, the numerical value of the determinant will change when the matrix truncation parameter N changes. For all these reasons, the determinant itself is not a suitable function to identify bifurcation points in this problem, though its sign is effective at removing the slope discontinuities of $\sigma_1(s)$, enabling the use of root-finding algorithms to rapidly locate its zeros.

Remark 3.10. In the context of dynamical systems, du/dt = f(u, s), many test functions have been devised to identify fold points, Hopf points, and branch points [15,16,33,46,48]. For large-scale equilibrium problems arising from discretized PDEs, Bindel et al. [16] reached the same conclusion we did above in Remark 3.9 on the unsuitability of (3.33) as a test function. Instead, in [16], minimally augmented systems [5,14,15,48,49] are used together with Newton's method to locate branch points. Studying the details of this approach, e.g., Algorithm 5 of [16], the Newton iteration involves solving f = 0 simultaneously with driving $\psi(s)$ in (1.2) to zero. As a result, intermediate Newton iterations will not involve states u that lie precisely on the primary bifurcation curve. This causes a problem for us as we have to linearize about a periodic solution to use Bloch-Fourier theory. The assumption that g^{ee} in (1.2) is square is also incompatible with our formulation of the traveling wave problem as an overdetermined nonlinear least squares problem, where g in (2.35) has more rows than columns to reduce aliasing errors and improve the accuracy of the computed periodic or quasi-periodic traveling waves. We prefer to treat the two stages of finding traveling waves and studying their behavior under perturbation as separate infinite dimensional problems that we solve with spectral methods using as many modes as necessary to achieve double-precision accuracy. One could still devise a minimally augmented systems approach within this philosophy to search for changes in the dimension of the kernel of $\mathcal{I}^{\text{qua}}[q^{\text{per}}(s)]$, but it would require a custom implementation and the resulting test function $\psi(s)$ analogous to (1.2) would not be much cheaper to compute than our $\chi(s)$. Moreover, $\psi(s)$ is only locally defined near each bifurcation point due to various choices of vectors that are made when augmenting the Jacobian. It also does not have the mesh independence feature of $\chi(s)$, so $\psi(s)$ will change discontinuously if the mesh is refined adaptively as s changes.

Remark 3.11. The closest test function we have found in the literature to (3.29) is a signed version of the magnitude of the smallest eigenvalue of f_u , denoted $|\lambda_{\min}(s)|$, (see equation (67) of [16]), which is proposed as an alternative to $\det(f_u(s))$ for detecting zero-Hopf points. We use σ_{\min} instead of $|\lambda_{\min}|$ and broaden the scope of the test function to search for branch

points. This has the advantage that it can be applied to an equation g(u,s)=0 that is equivalent to f(u,s)=0 but is no longer in dynamical systems form. For example, one does not obtain the dynamic water wave equations [25,37–39,71,92] by setting $\eta_t=\Re[q]$ in (3.3), since the velocity potential has been eliminated in the traveling wave equations. While the eigenvalues of f_u at an equilibrium point give information about the dynamics of u under perturbation, only the kernel of g_u (and changes in its dimension) are relevant, making $\sigma_{\min}(s)$ more natural than $|\lambda_{\min}(s)|$ in a test function based on solving g=0.

Remark 3.12. Since $D_q \mathcal{R}[q^{\mathrm{per}}]$ maps $(\chi_{\sigma}^{(1)}, 0, 0)$ to $\chi_{\rho}^{(1)}$ with $0 < \rho < \sigma$, it would be natural to use $\left\{2^{-1/2}e^{-\sigma(|l_1|+1)}\varphi_{l_1,1}\right\}_{l_1 \in \mathbb{Z}}$ and $\left\{2^{-1/2}e^{-\rho(|j_1|+1)}\varphi_{j_1,1}\right\}_{j_1 \in \mathbb{Z}}$ as orthonormal bases for $\chi_{\sigma}^{(1)}$ and $\chi_{\rho}^{(1)}$ in the domain and range. This would cause the rows and columns of $\mathcal{J}^{\mathrm{qua}}[q^{\mathrm{per}}]$ to be rescaled so that entry $\hat{u}_{j_1}^{(l_1,1)}$ in (3.26) is multiplied by $e^{-\sigma|l_1|}e^{\rho|j_1|}$. This yields a two-parameter family of matrices $\mathcal{J}^{\mathrm{qua}}[q^{\mathrm{per}}]$, parameterized by ρ and σ , that ultimately predict the same bifurcation points and perturbation directions to switch branches. Recall that σ is defined by the requirement that $\eta \in \mathcal{V}_{\sigma}^{\mathrm{per}}$, so any smaller positive value can also be used without violating the hypotheses. If σ is small, the corresponding ρ will also be small since $\rho \in (0,\sigma)$. So we are effectively considering the $\sigma \to 0^+$ limit, with $e^{-\sigma|l_1|}e^{\rho|j_1|} \approx 1$, in the formula (3.26) for $\mathcal{J}^{\mathrm{qua}}[q^{\mathrm{per}}]$.

This is the most suitable choice for the numerical algorithm for three reasons. First, if ρN were large, floating-point errors would be amplified in the matrix entries in the lower-left corner of $\mathcal{I}^{\text{qua}}[q^{\text{per}}]$, where $|j_1| \gg |l_1|$, possibly reducing the accuracy of $\sigma_1(s)$ in (3.28) and the corresponding right singular vector, v_1 , which is the desired null vector predicting the bifurcation direction at the zeros of $\sigma_1(s)$. Second, N may need to be increased to fully resolve this null vector for the rescaled version of $\mathcal{I}^{\text{qua}}[q^{\text{per}}]$. Indeed, if v_1^j are the entries of v_1 for the unscaled version of $\mathcal{I}^{\text{qua}}[q^{\text{per}}]$, then $Ce^{\sigma|j|}v_j$ will be the entries of v_1 for the rescaled version, which decay slower and therefore need a larger N to decay below the roundoff-error threshold. (C is a normalizing constant.) And third, rescaling the matrix $\mathcal{I}^{\text{qua}}[q^{\text{per}}]$ will change its singular values, possibly leading to new small singular values that do not correspond to bifurcation directions but instead to high-frequency inputs to $D_q \mathcal{R}[q^{\text{per}}]$ that are compressed due to the change in norm from the input space $(\mathcal{X}^{(1)}_{\sigma},0,0)$ to the output space $\mathcal{X}^{(1)}_{\rho}$. By considering the $\sigma \to 0^+$ limit, only the well-resolved singular values are small.

3.3. Computing the sign of the determinant of a matrix along with its singular values

For simplicity, since the results of this section are not tied to the water wave problem, we revert to standard numerical linear algebra notation: \mathcal{I}^{qua} will be denoted by A; its dimension 2N+1 will be denoted by n; and the singular values will be ordered so that $\sigma_1 \geqslant \sigma_2 \geqslant \cdots \sigma_n \geqslant 0$. In floating-point arithmetic, we *define* the sign of the determinant as a single function (without computing det A as an intermediate result) to be

$$\operatorname{sgn} \det A = (\det U)(\det V), \qquad A = U \Sigma V^T, \qquad \Sigma = \operatorname{diag}(\sigma_1, \dots, \sigma_n). \tag{3.34}$$

This is a procedural definition: compute the SVD of A numerically to obtain U and V, which are orthogonal. Then compute their determinants by LU or QR factorization, round to 1 or -1, and multiply them together. As explained in Section 3.2, if A depends analytically on a parameter s, then $\chi(s) = (\det U(s))(\det V(s))\sigma_n(s)$ will be a real analytic function that does not have slope discontinuities at the zeros of $\sigma_n(s)$. This conclusion relies on the *existence* of an analytic SVD, but it is only necessary to compute the standard SVD with non-negative singular values. Our goal now is to show how to compute $(\det U)(\det V)$ without actually forming the matrices U and V or computing their determinants explicitly.

Recall that the first step of the SVD algorithm is to compute a bidiagonal reduction, e.g., using the 'dgebrd' routine in the LAPACK library:

$$U_0^T A V_0 = B_0. (3.35)$$

Here U_0 and V_0 are orthogonal matrices and B_0 is upper bidiagonal. We will show that

$$\operatorname{sgn} \det A = (\det U_0)(\det V_0) \operatorname{sgn} (\det B_0), \tag{3.36}$$

where $\operatorname{sgn}(\det B_0) = \prod_{j=1}^n \operatorname{sgn}\left((B_0)_{jj}\right)$. Here $(\det U_0)$ and $(\det V_0)$ are ± 1 with parity matching the number of left and right Householder transformations performed in the bidiagonal reduction, which are easy to count from the output of 'dgebrd'. The left-hand side of (3.36) is still defined as $(\det U)(\det V)$, but we wish to use (3.36) as a cheaper alternative.

Our task is now to analyze what would happen if we were to continue with the standard algorithm to compute U and V along with Σ . The next step of this standard algorithm is to call 'dbdsqr' to compute a sequence of upper bidiagonal matrices

$$B_k = U_k^T B_{k-1} V_k, \qquad (k = 1, 2, 3, ...)$$
 (3.37)

that converge rapidly to a diagonal matrix $\tilde{\Sigma}$. In the initial iterations, while searching for the smallest singular values, 'dbdsqr' employs a zero-shift in the implicit QR algorithm [31] or the mathematically equivalent 'dqds' algorithm [32,45].

This leads to high relative accuracy in all the computed singular values. Moreover, each iteration of (3.37) in floating-point arithmetic is equivalent to introducing a small relative perturbation of each non-zero matrix entry of B_{k-1} , performing a "bulge-chasing" sequence of Givens rotations in exact arithmetic [31,32], and then perturbing each non-zero entry of the result by a small relative amount to obtain B_k . These perturbations of the diagonal and superdiagonal entries of B_{k-1} and B_k do not affect the signs of their determinants, and the Givens rotations all have unit determinant, so $\operatorname{sgn}(\det B_k) = \operatorname{sgn}(\det B_{k-1})$. On each iteration, super-diagonal entries of B_k that are sufficiently small relative to their neighboring diagonal entries are zeroed out, which does not affect $\operatorname{sgn}(\det B_k)$. The algorithm terminates and $\widetilde{\Sigma}$ is set to B_k when the last super-diagonal entry is zeroed out. Thus, $\operatorname{sgn}(\det \widetilde{\Sigma}) = \operatorname{sgn}(\det B_0)$. At this point we have

$$A = \tilde{U}\tilde{\Sigma}\tilde{V}^T, \qquad \tilde{U} = U_0U_1 \cdots U_K, \qquad \tilde{V}^T = V_K^T \cdots V_1^T V_0^T, \tag{3.38}$$

where *K* is the number of iterations required for convergence. We finally obtain

$$A = U\Sigma V^{T} = (\tilde{U}P^{T})(P\tilde{\Sigma}DP^{T})(PD\tilde{V}^{T}), \qquad D = \operatorname{diag}\left(\operatorname{sgn}(\tilde{\sigma}_{1}), \dots, \operatorname{sgn}(\tilde{\sigma}_{n})\right), \tag{3.39}$$

where multiplying $\tilde{\Sigma}$ by D takes the absolute values of the diagonal entries and P is a permutation matrix such that $\Sigma = P\tilde{\Sigma}DP^T$ contains the singular values on the diagonal in non-increasing order. Note that we have transferred the signs on the diagonal of $\tilde{\Sigma}$ to the rows of \tilde{V}^T via D. We conclude that

$$(\det U_0)(\det V_0)\operatorname{sgn}(\det B_0) = (\det U_0)(\det V_0)\operatorname{sgn}(\det \tilde{\Sigma}) = (\det \tilde{U})(\det \tilde{V})\det(D)$$

$$= \det(\tilde{U}P^T)\det(PD\tilde{V}^T) = (\det U)(\det V),$$
(3.40)

where we used $\det(\tilde{U}) = \det(U_0)$ and $\det(\tilde{V}) = \det(V_0)$ since the matrices U_1, \ldots, U_K and V_K^T, \ldots, V_1^T are comprised of Givens rotations of unit determinant. This shows that we can stop at (3.36) and get the same result as continuing to the completed computation of $(\det U)(\det V)$. Again, this is due to the 'dbdsqr' and 'dqds' algorithms maintaining high relative accuracy on the entries of successive bidiagonal matrices B_k . The smallest entries on the diagonal cannot jump across zero as this would entail a large relative change.

Since sgn det A is known already after the initial bidiagonal reduction, it is not necessary to accumulate the Givens rotations to form \tilde{U} and \tilde{V}^T in (3.38), apply the permutations to form U and V^T in (3.39), or compute the determinants of U and V explicitly. The initial bidiagonal reduction involves $(8/3)n^3 + O(n^2)$ flops [32] while forming U and V and computing their determinants involves another $(16/3)n^3 + O(n^2)$ flops, which triples the running time. Once a zero of $\chi(s)$ has been found, we can form V to find the null vector of A in $2n^3 + O(n^2)$ flops, without also forming U or computing the determinants of U and V.

4. Numerical results

We now present two examples of quasi-periodic traveling waves that bifurcate from finite-amplitude periodic traveling waves: quasi-periodic gravity waves and overturning quasi-periodic gravity-capillary waves.

4.1. Quasi-periodic gravity waves

As noted in the introduction, typical wave numbers for capillary waves in the ocean are 10^7 times greater than those of gravity waves, and one does not expect to observe interesting nonlinear interaction between component waves of such different length scales. For ocean waves, it is appropriate to set the surface tension coefficient to zero, which removes the capillary wave branch [36] from the dispersion equation (1.1). We are interested in quasi-periodic waves in which the two wavelengths are comparable, so we use $k_1 = 1$ and $k_2 = k = 1/\sqrt{2}$ for comparison with several of the examples in [91]. Whereas the quasi-periodic solutions computed in [91] persist to zero amplitude, the pure gravity wave problem does not support genuinely quasi-periodic solutions in the linearization about the zero solution since there is only one wave number k for a given wave speed c in the dispersion relation (1.1). Thus, we must search for secondary bifurcations.

Since surface tension is held fixed at $\tau=0$, this is a one-parameter bifurcation problem. We use the wave height, $h=\tilde{\eta}(0)-\tilde{\eta}(\pi)$, as the amplitude parameter as it increases monotonically from the zero solution to the sharply crested 120° corner wave [59]. The blue curves in Fig. 2 show wave speed c versus wave height h (left panel and inset) and versus $\hat{\eta}_{1,0}$ (right panel and inset). Here we follow the convention of Remark 2.4 and write $\hat{\eta}_{1,0}$ rather than $\hat{\eta}_1$, even though $\eta(\alpha_1,\alpha_2)=\tilde{\eta}(\alpha_1)$ is independent of α_2 . Each blue marker corresponds to a computed periodic traveling wave. Note that both the wave speed c and the first Fourier mode $\hat{\eta}_{1,0}$ possess turning points beyond which they no longer increase monotonically as one progresses further along the primary bifurcation branch. The black markers correspond to quasiperiodic solutions, and will be discussed below. We increase the Fourier cutoff N_1 in (2.27) as needed to maintain spectral accuracy in the computed traveling waves.

Table 1 gives the sequence of Fourier cutoff values N_1 used in the data of Fig. 2 as well as the largest wave height h for which N_1 was used. We used $M_1 = 3N_1$ gridpoints in the pseudo-spectral computation of the products and quotients in (2.9) and (2.35) and for the rows of the residual function r_m in (2.30). Also shown in the table are the Fourier cutoff

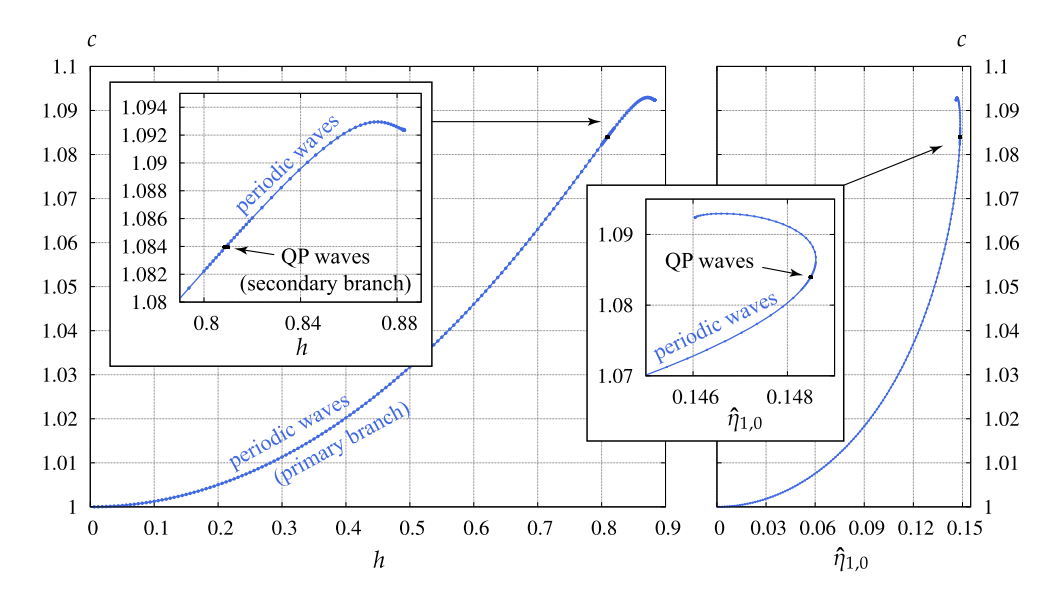


Fig. 2. Bifurcation diagrams of the primary branch (blue) and a secondary branch (black) for traveling water waves with zero surface tension. The wave height $h = \tilde{\eta}(0) - \tilde{\eta}(\pi)$ is preferable as an amplitude parameter to the wave speed c or the first Fourier mode $\hat{\eta}_{1,0}$ on the primary branch as it increases monotonically all the way to the extreme 120° corner wave. (For interpretation of the colors in the figure(s), the reader is referred to the web version of this article.)

Table 1 Largest wave height h for which the Fourier cutoff N_1 was used to compute the periodic waves on the primary branch in Fig. 2, and the cutoff N that was used to truncate $g^{\rm per}$ to 2N+1 rows and columns. In the bottom row, $N=N_1$.

h	0.075	0.2	0.3	0.4	0.575	0.65	0.725	0.8	0.82	0.832
N_1	22	30	48	60	128	180	300	600	768	864
Ν	48	54	64	80	160	192	324	640	768	864
h	0.8394	0.8429	0.8525	0.8627	0.8687	0.8721	0.8763	0.8786	0.8815	0.88305
N_1	1024	1350	1800	2400	4096	6144	8192	12288	16384	32000

values N used to truncate \mathcal{I}^{qua} in (3.26) to 2N+1 rows and columns. This calculation also requires a grid on which to evaluate the products and quotients in (3.6)–(3.10). For this we used M=3N gridpoints. In the last column of Table 1, with $N=N_1=32000$, we reduced M_1 to 65536 and M to 78732 to reduce the memory cost and running time, so aliasing errors may be slightly higher in this final batch of results.

Panels (a)–(c) of Fig. 3 show the first several singular values σ_j (blue) as well as $-\sigma_j$ (red), keeping in mind the convention (3.28) that $\sigma_{j+1} \geqslant \sigma_j \geqslant 0$. These are plotted as functions of the wave height h for each of the periodic solutions corresponding to the blue markers in Fig. 2. We find two bifurcation points in the range $0 \leqslant h \leqslant 0.88305$, which we label

$$h_A = 0.8090707936918, h_F = 0.882674234631. (4.1)$$

The corresponding wave speeds are

$$c_A = 1.083977046908, \qquad c_E = 1.09238325132. \tag{4.2}$$

Here *E* stands for "extreme," as the wave profile of this bifurcation is getting close to the limiting 120° corner wave, which has been computed accurately by Gandzha and Lukomsky [47] and has a wave height of $h_{\text{max}} = 0.88632800992$. The black curve in Fig. 3 shows $\chi(h)$, which turns out to satisfy

$$\chi(h) = \begin{cases} \sigma_1(h), & h \le h_A \text{ or } h \in [h_E, 0.88305], \\ -\sigma_1(h), & h_A \le h \le h_E. \end{cases}$$
(4.3)

There may be additional zero-crossings with h > 0.88305, but we ran out of computational resources to search for them.

We compute h_A using Brent's method [17] starting with the bracket $\chi(0.8)=0.0100259>0$ and $\chi(0.82)=-0.0130748<0$. Brent's method uses a combination of linear interpolation, inverse quadratic interpolation, and bisection to rapidly shrink the bracket to a zero of the function without derivative evaluations. In this example, only 7 additional function evaluations were needed to converge, with $\chi(h)$ taking on the values 4.5×10^{-4} , -4.7×10^{-9} , 7.2×10^{-12} , 1.5×10^{-13} , -2.3×10^{-13} , 1.1×10^{-14} , -2.9×10^{-15} . The last value corresponds to $h=h_A$ reported in (4.1). We used

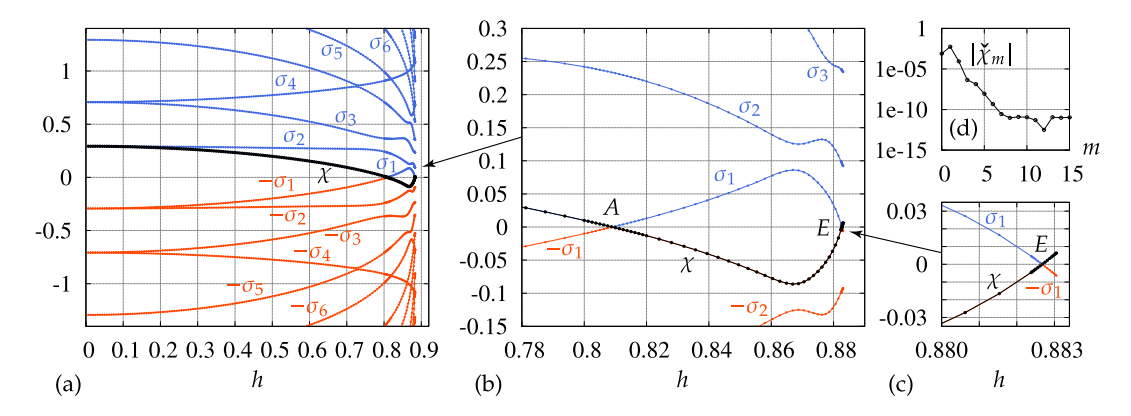


Fig. 3. Plots of the smallest singular values of g^{qua} versus h (blue), their negations (red), the test function $\chi(h)$ (black), the bifurcation points A and E, and the Chebyshev amplitudes $|\check{\chi}_m|$ obtained from the interpolation points shown in panel (c). Note that $\chi(h)$ is a smooth function in spite of the many changes in Fourier cutoff N_1 and mesh size M_1 from Table 1 represented in the graphs in panels (a)–(c).

 $N_1 = 768$ and $M_1 = 2304$ in the traveling wave calculation and 2N + 1 = 1537 for the dimension of \mathcal{I}^{qua} in the SVD calculation when computing $\chi(h)$ inside Brent's method. The total running time of the 9 function evaluations was 21.7 seconds on a workstation with two 12-core 3.0 GHz Intel Xeon Gold 6136 processors.

To demonstrate an alternative approach, we compute h_E using polynomial interpolation. First, we identify a bracket with $\chi(0.88238) = -0.00467 < 0$ and $\chi(0.88305) = 0.00638 > 0$. We then evaluate χ on a 16-point Chebyshev-Gauss grid over the interval [0.88238, 0.88305]. Unlike Brent's method, this can be done in parallel, though we did not have the computational resources to do this. From these values, we obtain the expansion

$$\chi(h) \approx \acute{\chi}(h) = \sum_{m=0}^{15} \check{\chi}_m T_m \left(2 \frac{h - 0.88238}{0.88305 - 0.88238} - 1 \right). \tag{4.4}$$

Panel (d) of Fig. 3 shows the Chebyshev mode amplitudes $|\check{\chi}_m|$. It appears that the modes decay rapidly up to m=7, and then start to be corrupted by floating-point arithmetic errors. So we truncate the series (4.4) by reducing the upper limit from 15 to 7 and then use Newton's method on $\check{\chi}(h)$ to obtain h_E in (4.1). A final evaluation of the original function χ (not its polynomial approximation) yields $\chi(h_E) = 2.1 \times 10^{-12}$. The relatively large floating-point errors visible in the high-frequency Chebyshev modes and the larger value of $|\chi(h_E)|$ relative to $|\chi(h_A)|$ are due to the increase in problem size. For the h_E calculation, we used $N_1 = N = 32000$, $M_1 = 65536$ and M = 78732. We discuss floating-point errors in the smallest singular value (and hence in χ) in Appendix A.

Remark 4.1. It would have been better (though not worth redoing) to use a nested set of Chebyshev-Lobatto grids with 2^n+1 points. We could have stopped at n=3 rather than guessing that 16 points would be enough to resolve $\chi(h)$ with spectral accuracy, which turned out to be overkill. Each $\chi(h)$ evaluation involves computing a traveling wave and then computing the SVD of \mathcal{I}^{qua} . At this problem size, each traveling wave calculation takes 45 minutes on one large memory node of the Lawrencium cluster at Lawrence Berkeley National Laboratory (LBNL) while the SVD takes 50 minutes on 15 standard memory nodes, using ScaLapack. Each node has 32 cores (2.3 GHz) and either 96 GB or 1.6 TB of memory.

Remark 4.2. If the problem is so large that even the bidiagonalization phase of the SVD is prohibitively expensive, one can compute only the smallest singular values using bisection and inverse iteration [32,74]. In this case, one can still use Chebyshev polynomials to represent $\chi(s)$ and locate bifurcation points, but a sign has to be added by hand to some of the values of $\sigma_{\min}(s_i)$ to convert them into $\chi(s_i)$, where s_i are the Chebyshev-Lobatto gridpoints. This is usually easy by plotting both $\sigma_{\min}(s_i)$ and $-\sigma_{\min}(s_i)$ on the same plot, as in panel (c) of Fig. 3, and looking at the graphs to determine where they cross zero. Usually at most one point has an ambiguous sign, and it is easy to tell which sign is correct since the Chebyshev modes will only decay rapidly when $\chi(s)$ has been sampled with the correct signs. One could potentially automate this process using continuous invariant subspace (CIS) methods [14,15,30,35,46] to avoid sign flips in the corresponding singular vectors, or by introducing signs from one end of the list of $\chi(s_i)$ values until the Chebyshev modes suddenly decay rapidly.

Panels (a) and (b) of Fig. 4 show the wave profiles $\tilde{\zeta}(\alpha) = \tilde{\xi}(\alpha) + i\tilde{\eta}(\alpha)$ of the periodic traveling waves with wave heights h_A and h_E in (4.1). Panel (b) shows a full period of the wave while panel (a) shows a closer view at the crest tip. The aspect ratio of both plots is 1 to demonstrate how close solution E is to the 120° corner wave. The mean fluid height of both waves is 0, with solution E higher close to the crest tip and solution E higher beyond the crossing points visible in panel (a). Panels (c) and (d) show the Fourier mode amplitudes $|\hat{\eta}_j|$ of these two solutions as well as the components E0 of the null vector \hat{q}^{qua} 0 expressed in the E1 basis, as in (3.30). Solution E3 is resolved to double-precision accuracy using

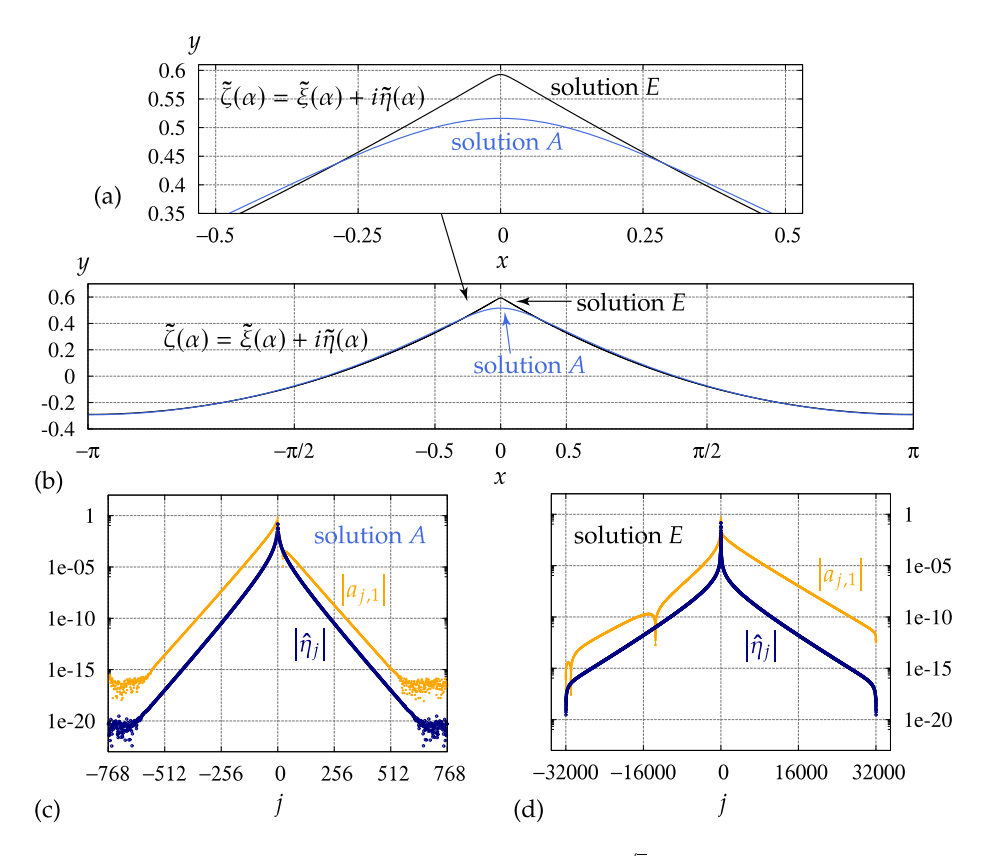


Fig. 4. Wave profiles of solutions A and E, where quasi-periodic bifurcations with $k = 1/\sqrt{2}$ were detected in Fig. 3, along with their Fourier mode amplitudes $|\hat{\eta}_i|$ and the amplitudes of the components $a_{i,1}$ of the null vector \dot{q}^{qua} in (3.30).

 $N_1 = N = 768$. Indeed, the mode amplitudes in panel (c) decay through at least 15 orders of magnitude with floating-point errors evident in the highest-frequency modes. Solution E is nearly fully resolved with $N_1 = N = 32000$, but the mode amplitudes in panel (d) have not decayed all the way to the point that roundoff effects become visible. We did not attempt to increase N_1 and N further due to the computational expense.

We next search for solutions on the quasi-periodic branch $\mathfrak{q}^{\mathrm{qua}}(\theta)$ that intersects $\mathfrak{q}^{\mathrm{per}}(s)$ at solution A. We have been using s=h, the wave height, as the amplitude parameter on the primary branch and will switch to $\theta=\hat{\eta}_{0,1}$ on the secondary branch. Note that $\theta=0$ for all the solutions on the primary branch. Another mode $\hat{\eta}_{j,1}$ with $j\neq 0$ could have been used instead, but j=0 turns out to maximize $|a_{j,1}|$ in the expansion of \dot{q}^{qua} in (3.30). The lowest-frequency coefficients, normalized so that $\sum_{|j|\leq N} |a_{j,1}|^2 = 1$, are

Note that $a_{j,1}$ is not symmetric about j=0, which is also evident in panel (c) of Fig. 4. As explained at the end of Section 2.2, we use

$$\mathfrak{q}^{\text{qua}}(\theta) \approx q^{\text{guess}} = q^{\text{bif}} + \varepsilon \dot{q}^{\text{qua}}, \qquad \varepsilon = \frac{\theta}{a_{0,1}}, \qquad \theta = \hat{\eta}_{0,1}, \tag{4.6}$$

as an initial guess for the first point on the bifurcation path, where $q^{\rm bif}=(\eta_A,\tau_A,b_A)$ with $\tau_A=0$ and $b_A=c_A^2$ from (4.2), and $\dot{q}^{\rm qua}=(\dot{\eta}^{\rm qua},0,0)$. The leading 2D Fourier modes of $\eta^{\rm guess}=\eta_A+\varepsilon\dot{\eta}^{\rm qua}$ are given by

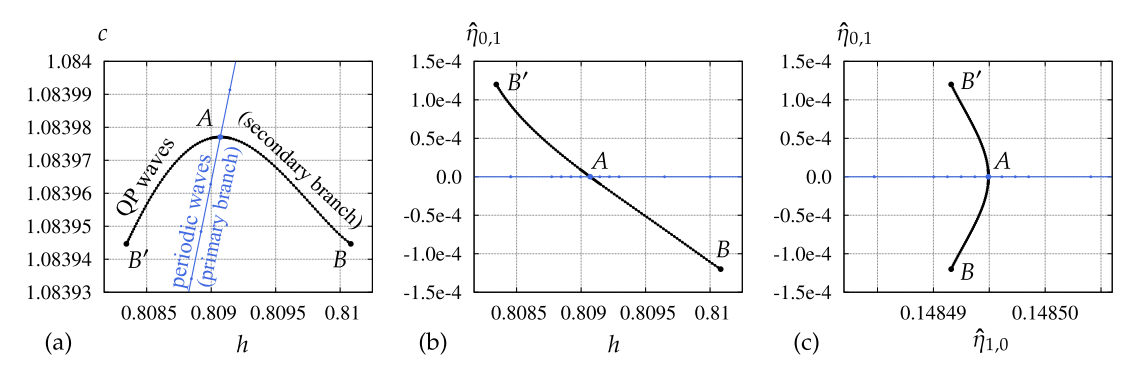


Fig. 5. The secondary branch of quasi-periodic traveling waves (black) bifurcates from the primary branch of periodic waves (blue) at solution A. The solutions between A and B' are related to those between A and B by the symmetry (4.8). Panel (a) shows a highly magnified view of the plots in the left panel of Fig. 2.

where we make use of (2.14) to obtain $\hat{\eta}_{j,-1}^{\text{guess}} = \hat{\eta}_{-j,1}^{\text{guess}} = \varepsilon a_{-j,1}$ for $j \geqslant 0$. We use the 'r2c' and 'c2r' routines of FFTW, which take advantage of (2.14) to avoid storing Fourier modes with $j_1 < 0$.

Since the kernel of $D_q \mathcal{R}[q^{\mathrm{bif}}]$ in (3.25) is two-dimensional, it might have been necessary to include a term $\varepsilon_2 \dot{q}^{\mathrm{per}}$ in (4.6) with ε_2 depending linearly on θ and ε . But solutions $\mathfrak{q}^{\mathrm{qua}}(\theta) = (\eta^{\mathrm{qua}}(\theta), 0, b^{\mathrm{qua}}(\theta))$ on this path turn out to have the symmetry property

$$\eta^{\text{qua}}(-\theta)(\alpha_1, \alpha_2) = \eta^{\text{qua}}(\theta)(\alpha_1, \alpha_2 + \pi), \qquad b^{\text{qua}}(-\theta) = b^{\text{qua}}(\theta). \tag{4.8}$$

Since all the nonzero Fourier modes $\dot{\hat{\eta}}_{j_1,j_2}^{\text{qua}}$ have $j_2 \in \{1,-1\}$, we see that

$$(-\varepsilon)\dot{\eta}^{\text{qua}}(\alpha_1,\alpha_2) = \varepsilon \dot{\eta}^{\text{qua}}(\alpha_1,\alpha_2 + \pi), \tag{4.9}$$

so changing the sign of the perturbation in (4.6) is equivalent to shifting by π in the α_2 direction. Including $\varepsilon_2 \dot{q}^{\text{per}}$ in the formula for q^{guess} would break this symmetry if ε_2 were a non-zero multiple of ε .

In Fig. 5, we plot 3 bifurcation curves showing different aspects of how the secondary branch, plotted in black, splits from the primary branch, plotted in blue. The black markers between the bifurcation point A and the point labeled B correspond to solutions computed by minimizing the objective function (2.25) holding $\theta = \hat{\eta}_{0,1}$ at fixed values. The markers on the other side, between A and B', were obtained from these solutions using the symmetry (4.8) rather than carrying out the minimization again. The decision to explore negative values of θ first was arbitrary. Exactly the same results would have been obtained in the other direction (aside from swapping the labels B and B'). We define the wave height B plotted in panels (a) and (b) as B0, B1 as B2. This choice will be discussed and justified in Remark 4.3 below.

For the first point on the secondary branch, we set $\varepsilon=1.768\times10^{-7}$, which corresponds to $\theta=\hat{\eta}_{0,1}=-1.0\times10^{-7}$. We then minimize the objective function (2.25) holding $\hat{\eta}_{0,1}$ fixed. The initial guess for the second point can be computed in the same way, by doubling ε , or from linear extrapolation from the zeroth point ($q^{\rm bif}$) and the first point. Both methods work well. The starting guess for each additional solution on the path is computed via linear extrapolation from the previous two solutions. As we progress along the path, we monitor the amplitudes of the 2D Fourier modes and increase N_2 as necessary to maintain spectral accuracy. The first several solutions are still very close to the periodic traveling wave, so $N_2=3$ and $M_2=8$ are sufficient. The traveling wave requires $N_1=550$, $M_1=1200$ to achieve spectral accuracy, so we held these fixed in the quasi-periodic calculation. Presumably N_1 and M_1 will need to be increased if one proceeds far enough along the path, but we always ran out of resolution in N_2 and M_2 first. The mesh parameters used for different values of $\theta=\hat{\eta}_{0,1}$ in our calculation are as follows:

Each column corresponds to a batch of solutions computed by numerical continuation by taking equal steps of size $\Delta\theta$ from $\theta = \theta_0$ to $\theta = \theta_1$. The factors of 10^{-6} apply to all the entries in the bottom 3 rows. For each new column, θ_0 is the same as θ_1 from the previous column, which means we recompute the solution with larger values of N_2 and M_2 using the previous solution as a starting guess. In the last column (with $N_2 = 48$), we simply refine the solution at $\theta = -1.2 \times 10^{-4}$ without progressing further along the path.

In Fig. 6, we plot the leading Fourier mode amplitudes $|\hat{\eta}_{j_1,j_2}|$ for solution *B*. The same data is plotted from three viewpoints in panels (a), (b) and (c). The grid is $M_1 \times M_2 = 1200 \times 108$, and the solver searches for modes $\hat{\eta}_{j_1,j_2}$ with

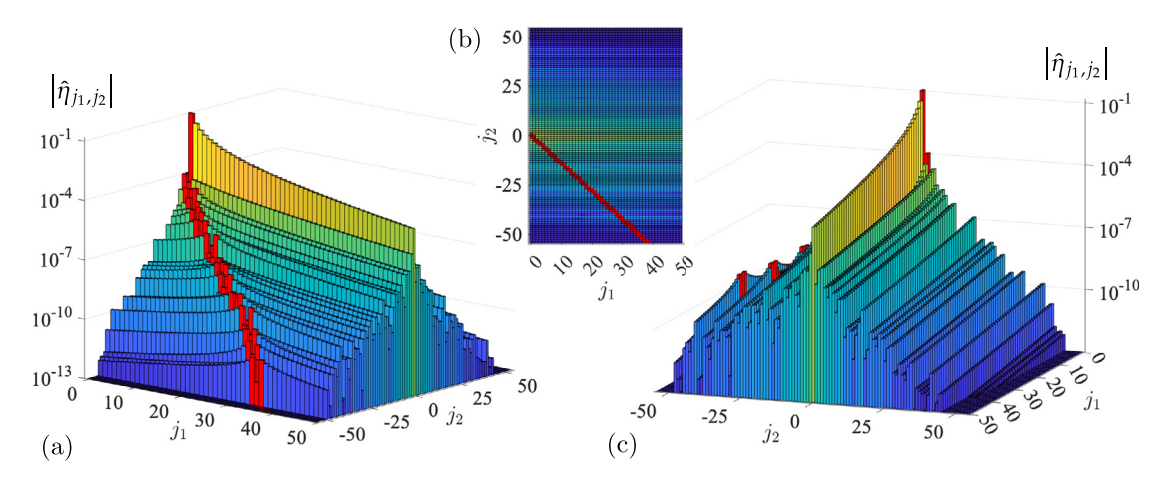


Fig. 6. Fourier mode amplitudes $|\hat{\eta}_{j_1,j_2}|$ for solution B of Fig. 5. The three plots show the same data from different viewpoints. The modes were truncated at $j_1 = 50$ in the plots, but extend to $j_1 = 550$ in the calculation. The resonant line $j_1 + kj_2 = 0$ is plotted in dark red in panel (b). The closest lattice points to this line are plotted in red in all three panels.

 $0 \le j_1 \le N_1 = 550$ and $|j_2| \le N_2 = 48$. The remaining modes with $551 \le j_1 \le 600$ and $49 \le |j_2| \le 54$ are set to zero in the nonlinear least squares solver but retained in the FFT calculations to reduce aliasing errors. The solver does not control $\hat{\eta}_{0,1}$, which is held fixed at -1.2×10^{-4} . The modes with $j_1 < 0$ are assumed to satisfy (2.14). In the figure, we truncate j_1 at 50, but the modes are non-zero out to $j_1 = 550$, and continue to decay along slices of constant j_2 in a similar way to the modes of the periodic wave A, shown in Fig. 4. The objective function F in (2.25) has been minimized to 1.9×10^{-25} for this solution. We did not try to compute more than one solution at this resolution as each calculation is quite expensive. The Jacobian \mathcal{J} in (2.35) has 129600 rows and 53398 columns and has to be factored at least once via the SVD in our implementation of the Levenberg-Marquardt method. We used ScaLapack for this purpose, and ran the code on 18 nodes (432 cores) of the Savio cluster at UC Berkeley. The running time was 70 minutes. We also did not attempt to follow the bifurcation branches at solution E as the periodic problem already involves 32000 active Fourier modes.

Panel (b) of Fig. 6 shows the Fourier amplitude data in a two-dimensional view using the same colormap as panels (a) and (c). Also plotted, in dark red, is the resonant line $j_1+j_2k=0$. Since $k=1/\sqrt{2}$ is irrational, the only lattice point lying precisely on this line is $(j_1,j_2)=(0,0)$. As discussed in [91], lattice points (j_1,j_2) close to this line correspond to plane waves $e^{i(j_1+j_2k)\alpha}$ of long wavelength. The residual function $\mathcal R$ in (3.3) is unchanged if η is perturbed by a constant function, and changes little for long wavelength perturbations. Thus, the above plane waves are approximate null vectors of the Jacobian (2.35). Such "small divisors" have been overcome in similar problems [10,12,13,44] building on Nash-Moser theory [52,69], though so far always at small-amplitude, near the zero solution. Adapting these rigorous techniques to the spatially quasi-periodic setting is a challenging open problem, especially in the present case of bifurcations from finite-amplitude periodic waves.

We avoid running into small divisors in our search for bifurcations by restricting $\ker D_q \mathcal{R}[q^{\text{bif}}]$ to $\mathcal{D}_{\sigma}^{(1)}$ in (3.26). But in fully nonlinear calculations such as solution B of Figs. 5 and 6, which has many active modes in both the j_1 and j_2 directions, one can see some effects of the small divisors on the Fourier modes corresponding to lattice points near the resonant line, which we plotted in red in all three panels of Fig. 6. In panel (a) we see that the modes $\hat{\eta}_{j_1,j_2}$ with $j_2 < 0$ grow in amplitude as j_1 increases to the resonant line (holding j_2 fixed), and then decay afterward. By contrast, we see in panel (c) that on the "back side" (with $j_2 > 0$), the modes appear to generally decay monotonically right away as j_1 increases. If we instead decrease j_1 through negative values with j_2 held fixed, the modes with $j_2 > 0$ are the ones that increase in magnitude until j_1 crosses the resonant line while the modes with $j_2 < 0$ will generally decay right away as $|j_1|$ increases. It is not necessary to plot this as it follows from the data shown in Fig. 6 and the symmetry (2.14), namely $\hat{\eta}_{-j_1,-j_2} = \hat{\eta}_{j_1,j_2}$.

Fig. 7 shows torus views of the bifurcation direction at solution A, namely $\dot{\eta}^{\text{qua}}(\alpha_1, \alpha_2)$ from (3.30), and the deviation in the wave profile from solution A to solution B,

$$\eta_B^{\text{dev}}(\alpha_1, \alpha_2) = \eta_B(\alpha_1, \alpha_2) - \eta_A(\alpha_1, \alpha_2), \tag{4.10}$$

where $\eta_A(\alpha_1,\alpha_2)$ is independent of α_2 . In the left panel, we actually plot $C\dot{\eta}^{\text{qua}}$, where the normalization constant C is chosen to minimize the distance from $C\dot{\eta}^{\text{qua}}$ to η_B^{dev} in L^2 on the torus, which turns out to be

$$C = \frac{\langle \dot{\eta}^{\text{qua}}, \eta_B^{\text{dev}} \rangle_{L^2(\mathbb{T}^2)}}{\langle \dot{\eta}^{\text{qua}}, \dot{\eta}^{\text{qua}} \rangle_{L^2(\mathbb{T}^2)}} = 2.121 \times 10^{-4}. \tag{4.11}$$

While the bifurcation direction predicts the large-scale features of η_B^{dev} , there are clear differences in the two contour plots. In particular, the symmetry in the left panel in which $\dot{\eta}^{\text{qua}}(\alpha_1,\alpha_2)$ changes sign on shifting α_2 by π , which occurs due to

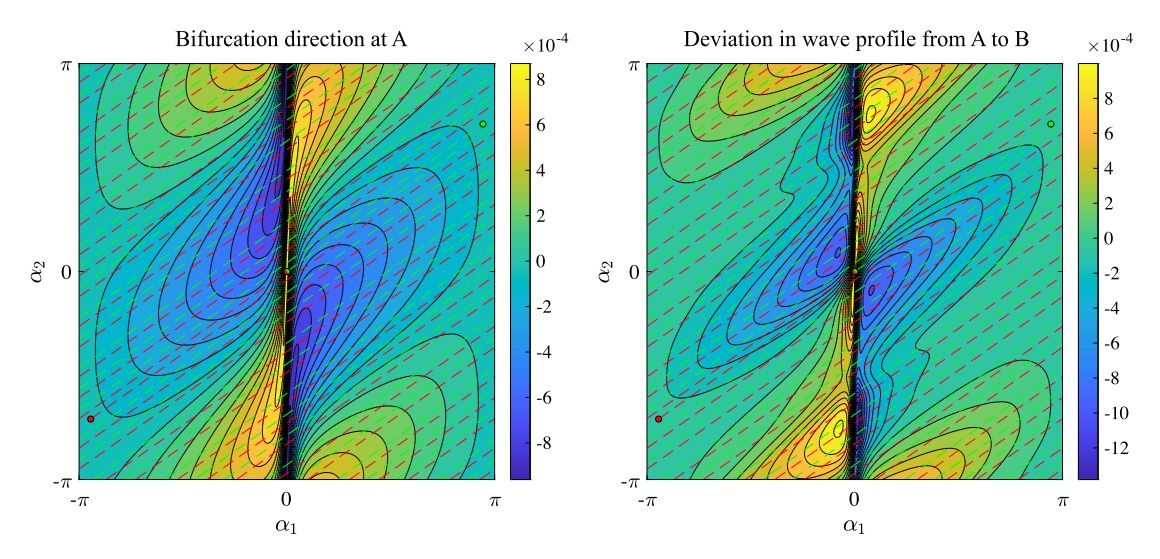


Fig. 7. Contour plots of the bifurcation direction $C\dot{\eta}^{\text{qua}}(\alpha_1,\alpha_2)$ and the deviation $\eta_B^{\text{dev}}(\alpha_1,\alpha_2)$ from solution A to solution B. The dashed lines show how the characteristic line $(\alpha,k\alpha)$ wraps around the periodic torus for $\alpha\geqslant 0$ (green) and $\alpha\leqslant 0$ (red). Evaluation along this characteristic line yields the one-dimensional quasi-periodic functions shown in panels (c) and (d) of Fig. 9.

 $\dot{\hat{\eta}}_{j_1,j_2}=0$ for $j_2\notin\{-1,1\}$, is broken in the right panel. Indeed, η_B^{dev} has a richer Fourier structure consisting of the modes plotted in Fig. 6 minus the modes of solution A, $\hat{\eta}_{j_1,j_2}=\hat{\eta}_j\delta_{j_2,0}$, where $\hat{\eta}_j$ is plotted in Fig. 4. Replacing α_2 by $\alpha_2+\pi$ in $\eta_B^{\text{dev}}(\alpha_1,\alpha_2)$ yields $\eta_{B'}^{\text{dev}}(\alpha_1,\alpha_2)$, where B' is the solution at the other end of the secondary bifurcation branch in Fig. 5.

Remark 4.3. For all the solutions on the path from *A* to *B* in Fig. 5, which correspond to negative values of $\theta = \hat{\eta}_{0,1}$, we find (by studying the numerical results) that the maximum and minimum values of $\eta(\theta)(\alpha_1, \alpha_2)$ occur at

$$\operatorname{argmax} \eta(\theta)(\alpha_1, \alpha_2) = (0, 0), \quad \operatorname{argmin} \eta(\theta)(\alpha_1, \alpha_2) = (\pi, 0), \quad (\theta < 0). \tag{4.12}$$

Thus, we define the wave height h on this quasi-periodic branch as

$$h(\theta) = \eta(\theta)(0, 0) - \eta(\theta)(\pi, 0). \tag{4.13}$$

However, on the path from A to B', where $\theta > 0$, the maximum and minimum values occur at $(0, \pi)$ and (π, π) , respectively, due to (4.8). So if we define $h_1(\theta) = \eta(\theta)(0, \pi) - \eta(\theta)(\pi, \pi)$, then the physical wave height is $h_1(\theta)$ for $\theta > 0$ and $h(\theta)$ for $\theta < 0$. Both $h_1(\theta)$ and $h(\theta)$ can be read off of panels (a) and (b) of Fig. 5, since $h_1(\theta) = h(-\theta)$. So it is preferable to plot $h(\theta)$ for positive and negative values of θ , as we have done, rather than plotting the physical wave height, which would introduce a slope discontinuity at the bifurcation point in panels (a) and (b) of Fig. 5. Moreover, it would discard the information about $h(\theta)$ with $\theta > 0$, replacing it by $h_1(\theta)$, which is already known from $h(\theta)$ with $\theta < 0$. We will simply refer to $h(\theta)$ in (4.13) as "the wave height."

Our next goal is to plot the 1D quasi-periodic functions obtained by evaluating the torus functions of Fig. 7 along the dashed red and green lines, namely

$$C\dot{\tilde{\eta}}(\alpha) = C\dot{\eta}^{\text{qua}}(\alpha, k\alpha), \qquad \tilde{\eta}_B^{\text{dev}}(\alpha) = \eta_B^{\text{dev}}(\alpha, k\alpha).$$
 (4.14)

We will plot them as functions of α rather than in the parametric form used in Fig. 4. This allows for a simpler correspondence with the torus functions of the conformal mapping formulation of (2.9) and avoids the complication of solutions A and B having slightly different parameterizations $\tilde{\xi}_A(\alpha)$ and $\tilde{\xi}_B(\alpha)$ in the x-direction. One would have to transform to a graph-based formulation of the problem to define analogues of $C\tilde{\eta}$ and $\tilde{\eta}_B^{\text{dev}}$ in (4.14) that are functions of x rather than α . Panel (a) of Fig. 8 shows that $\tilde{\eta}(\alpha)$ is more sharply peaked than the physical wave profile obtained by plotting $\tilde{\xi}(\alpha) = \tilde{\xi}(\alpha) + i\tilde{\eta}(\alpha)$ parametrically.

We wish to plot the functions in (4.14) over many cycles of the underlying periodic wave without losing resolution due to excessive horizontal compression of the plot. We do this by plotting the results on a periodic domain with a period that differs from 2π , the period of the underlying Stokes wave. To select a useful period for the plot, we consider best rational approximations of k. Panel (b) of Fig. 8 shows the fractional part

$$\{Qk\} = Qk - \lfloor Qk \rfloor, \qquad Q = 1, 2, 3, \dots, 50$$
 (4.15)

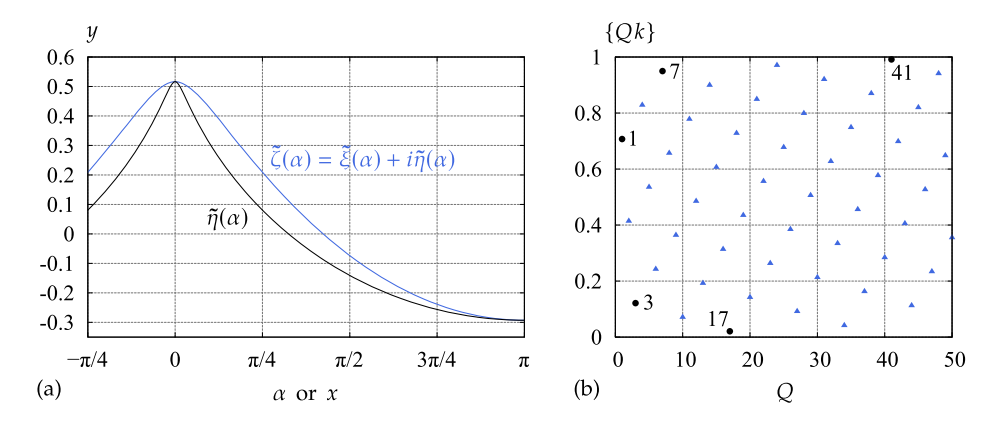


Fig. 8. Comparison of $\tilde{\eta}(\alpha)$ and the parametric plot $\tilde{\zeta}(\alpha) = \tilde{\xi}(\alpha) + i\tilde{\eta}(\alpha)$ for solution A, and fractional parts of the first 50 integer multiples of $k = 1/\sqrt{2}$.

of the first 50 integer multiples of the second wave number k, which is $k=1/\sqrt{2}$ in the present calculation. Here $\lfloor \cdot \rfloor$ is the floor function. We also write $\lfloor \cdot \rceil$ for the function that rounds its argument up or down to the nearest integer. Given a positive integer Q, the closest rational number of the form P/Q to k is found by setting $P=\lfloor Qk \rceil$. With this choice of P, let

$$e_1(Q) = |P - Qk| = \min(\{Qk\}, 1 - \{Qk\}), \qquad e_2(Q) = \left|\frac{P}{Q} - k\right| = \frac{e_1(Q)}{Q}.$$
 (4.16)

The black markers in the right panel of Fig. 8 minimize $e_1(Q)$ over previously seen values, i.e., $e_1(Q) \le e_1(q)$ for $1 \le q \le Q$. They correspond to the rational approximations

$$k \approx \frac{1}{1}, \qquad k \approx \frac{2}{3}, \qquad k \approx \frac{5}{7}, \qquad k \approx \frac{12}{17}, \qquad k \approx \frac{29}{41},$$
 (4.17)

where $k = 1/\sqrt{2}$. If we had minimized $e_2(Q)$ instead, as is usually done in defining best rational approximations, 1/2 and 7/10 would be added to the list.

Remark 4.4. In the present problem, $e_1(Q)$ gives the vertical shift (divided by 2π) of the characteristic line passing through (0,0) in the (1,k) direction after wrapping around the torus Q times in the α_1 -direction and approximately P times in the α_2 direction. So a small value of $e_1(Q)$ means $C\dot{\tilde{\eta}}(\alpha)$ and $\tilde{\eta}_B^{\text{dev}}(\alpha)$ will nearly recur on shifting α by $2\pi Q$. We will focus on the Q=17, P=12 case.

Panel (a) of Fig. 9 shows $17\frac{17}{36}$ cycles of solution A to the left and right of the origin. In panel (b), we wrap this solution around a torus of period $17\pi/9$. This is done by plotting $\tilde{\eta}_A(\alpha)$ parametrically versus

$$\bar{\alpha} = \operatorname{rem}\left(\alpha + \frac{17}{18}\pi, \frac{17}{9}\pi\right) - \frac{17}{18}\pi, \quad \operatorname{rem}(a, b) = \left(a/b - \lfloor a/b\rfloor\right)b. \tag{4.18}$$

The peak at the origin in panel (a) remains at the origin in panel (b), but successive peaks of the 2π -periodic Stokes wave are shifted by $\Delta\alpha=2\pi-\frac{17}{9}\pi=\frac{1}{9}\pi$ in panel (b) due to the mismatch of the period of the wave and that of the plot domain. The labels above the peaks indicate how far one must advance to the right in panel (a) to obtain the corresponding peak in panel (b). For example, progressing through 8 periods of the Stokes wave (to $\alpha=16\pi$) yields the right-most peak in panel (b). The next peak wraps around the plot domain, so $\alpha=18\pi$ in panel (a) gives the left-most peak of panel (b). The 17th peak in panel (a) (at $\alpha=34\pi$) sweeps out the same curve in panel (b) as the 0th peak in panel (a). The labels below the peaks in panel (b) work the same as those above the peaks, but moving left instead of right.

Panels (c) and (d) of Fig. 9 show the extracted functions (4.14) for $|\alpha| \le (2\pi) \left(17\frac{17}{36}\right)$, wrapped around the torus of panel (b) via (4.18). We do this to better view the quasi-periodic behavior of the traveling wave. In the same way that panel (b) shows more detail than panel (a) about the shape of the peaks of the Stokes wave, panels (c) and (d) show more detail than would be visible if they were compressed horizontally to match the style of panel (a). By offsetting the peaks of successive cycles of the Stokes wave, the dominant features of the linear perturbation $C\tilde{\eta}(\alpha)$ and the nonlinear perturbation $\tilde{\eta}_B^{\text{dev}}(\alpha)$ are similarly offset. Indeed, we find that the perturbations change most rapidly near the peaks of the Stokes wave, and these rapid changes are what we identify as their dominant features. We label these features in panels (c) and (d) with the value of α of the nearest peak of the Stokes wave. The labels come in pairs that differ by 34π . This is because two points α separated by 34π are mapped to the same point $\bar{\alpha}$ and will cross a peak of the Stokes wave together. So their dominant features will occur near each other when plotted versus $\bar{\alpha}$. The peak at the origin has 3 labels since the 0th, 17th and

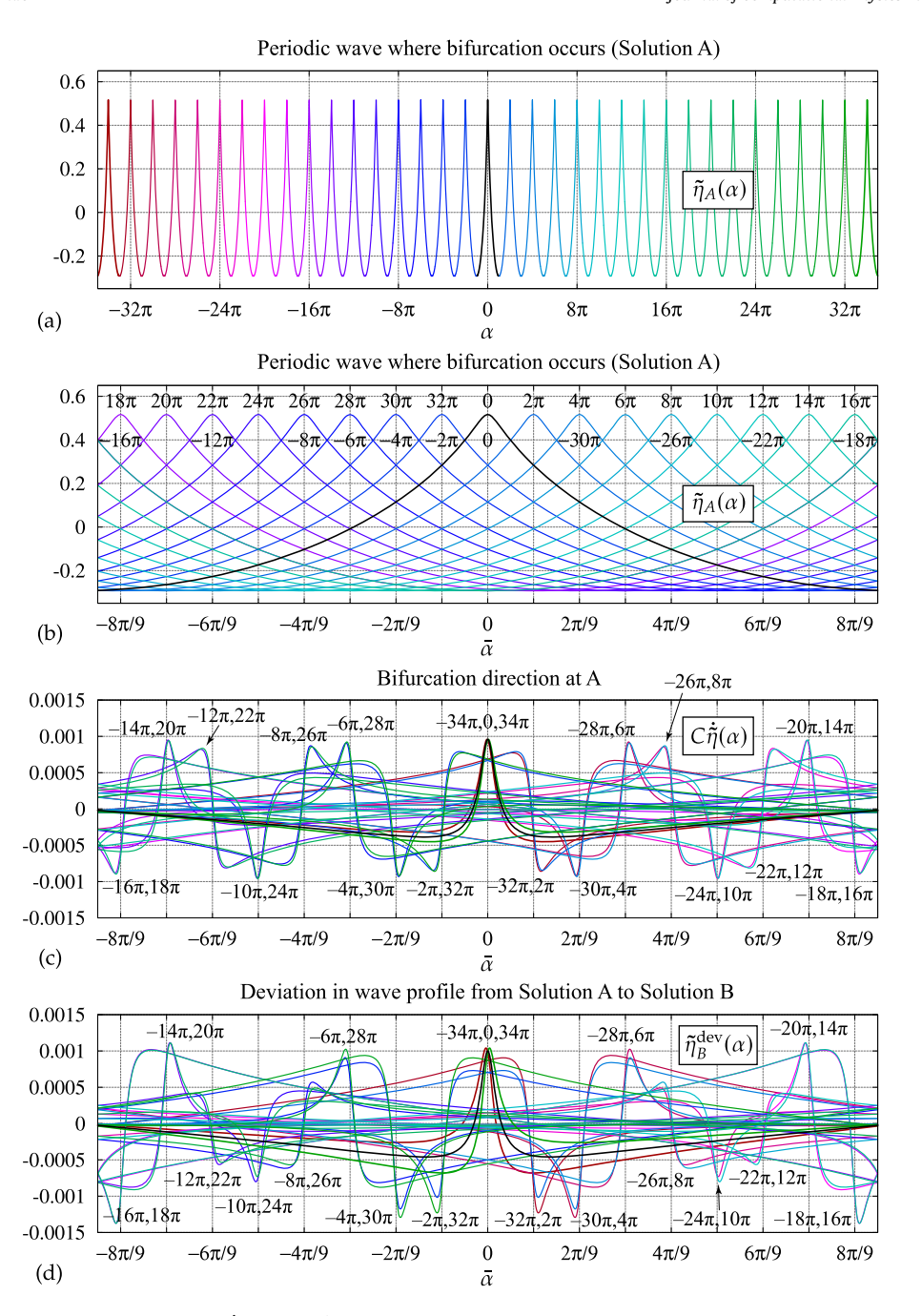


Fig. 9. Plots of $\tilde{\eta}_A(\alpha)$ and the perturbations $C\dot{\tilde{\eta}}(\alpha)$ and $\tilde{\eta}_B^{\text{dev}}(\alpha)$ predicted by linearization about solution A and actually occurring by following the secondary bifurcation branch from A to B. In panels (b)–(d), we plot the functions on a domain of period $(17/9)\pi$ to stagger both the peaks of solution A and the dominant features of the perturbations. The vertical dashed lines in panels (b)–(d) are centered on the peaks of the Stokes waves. The perturbations in panels (c) and (d) are color coded to match the corresponding peaks in panel (a) that have been perturbed.

-17th peaks of panel (a) are mapped to the 0th peak in panel (b). The final $\frac{17}{36}$ of a cycle is included so that these curves complete their cycles through the plot window rather than stopping abruptly at $\bar{\alpha} = 0$.

In addition to aligning their dominant features, mapping points α that differ by 17 cycles to the same point $\bar{\alpha}$ causes these curves to be close to each other in panels (c) and (d). By Remark 4.4, advancing α through 17 cycles will cause the torus function to be evaluated at the same value of α_1 and at a nearby value of α_2 , shifted up or down by $2\pi e_1(17) = 0.131$. In Fig. 7, the dashed green and red lines correspond to $\alpha \geqslant 0$ and $\alpha \leqslant 0$, respectively. Over the range $0 \leqslant \alpha \leqslant 34\pi$, each dashed green line is offset vertically by 0.131 from a nearby dashed red line. This vertical offset is equivalent to advancing α by 34π , i.e., by displacing (α_1, α_2) by $(34\pi, 34\pi k)$ and mapping back to \mathbb{T}^2 by periodicity, starting at a point on the red

line. The final fractional cycles of length $(17/36)(2\pi)$ in each direction are offset vertically by 0.131 from lines of the same color and terminate at the circular green and red markers in Fig. 7. As noted above, these fractional cycles are included to extend the plots in panels (c) and (d) of Fig. 9 to the end of the plot window so they don't end abruptly at $\bar{\alpha} = 0$.

Studying panels (c) and (d), we observe that the perturbation at the origin, plotted in black, sharpens the Stokes wave symmetrically, where we view following the secondary bifurcation branch as a perturbation of solution A. The other wave crests are perturbed asymmetrically and can be sharpened, flattened or shifted right or left, with no two perturbed in exactly the same way. Even though we could not follow this branch very far at the scale of the bifurcation diagram shown in Fig. 2 using wave height and wave speed as parameters, solution B has many small scale features not present in solution A. Moreover, nonlinear effects cause the deviation of B from A in panel (d) to differ visibly from that predicted by linearization, shown in panel (c). We also see that while the perturbations do stay reasonably close to each other when α increases by 17 cycles, differences are clearly visible and there would not be much agreement after another 17 or 34 cycles. Closer agreement could be achieved by switching to Q = 41 as $2\pi e_1(41) = 0.054$, but this would increase the number of peaks in panel (b) from 17 to 41, making it more difficult to distinguish the features that arise in panels (c) and (d).

From these results, it is natural to conjecture that this path of quasi-periodic solutions will continue until the wave profile develops a singularity, presumably with a 120° corner in physical space at the origin [59,76]. In the periodic case, this limiting corner wave has been proved to exist by Amick, Fraenkel and Toland [7] and studied numerically by Gandzha and Lukomsky [47]. Chen and Saffman [24] found that wavelength-doubling and wavelength-tripling bifurcations also lead to families of solutions that appear (in the numerical simulations) to terminate with the tallest crest sharpening to 120° while the other crests remain rounded. In the case of genuinely quasi-periodic traveling waves studied here, the analogous result would be for the torus function representing the traveling solution to develop a singularity at (0,0) when the wave height reaches a critical value.

To investigate this limit, it is preferable to transform our torus functions from a conformal mapping formulation to a graph-based formulation. Recall from (2.9) that ξ , which represents the quasi-periodic part of the horizontal position of the wave in the sense of (2.15), is related to the wave profile η via $\xi = H[\eta]$. Here ξ and η are torus functions. In [92], it is shown that if $\partial_{\alpha}|_{\alpha=0}\xi(\alpha_1+\alpha,\alpha_2+k\alpha)>-1$ for $(\alpha_1,\alpha_2)\in\mathbb{T}^2$, then the extracted wave profile

$$\tilde{\zeta}(\alpha) = \overbrace{\alpha + \xi(\alpha, k\alpha) + i}^{\tilde{\xi}(\alpha)} + i \overbrace{\eta(\alpha, k\alpha)}^{\tilde{\eta}(\alpha)}$$
(4.19)

is a graph and there is a torus function $\eta^{\text{phys}}(x_1, x_2)$ such that

$$\tilde{\eta}(\alpha) = \tilde{\eta}^{\text{phys}}(\tilde{\xi}(\alpha)), \qquad \tilde{\eta}^{\text{phys}}(x) = \eta^{\text{phys}}(x, kx), \qquad (\alpha, x \in \mathbb{R}).$$
 (4.20)

This torus function can be computed via

$$\eta^{\text{phys}}(\vec{\mathbf{x}}) = \eta(\vec{\mathbf{x}} + \vec{\mathbf{k}}\mathcal{A}(\vec{\mathbf{x}})), \qquad (\vec{\mathbf{x}} \in \mathbb{T}^2),$$
(4.21)

where $\vec{k} = (1, k)$ and $\mathcal{A}(\vec{x})$ is the unique solution [92] of

$$\mathcal{A}(\vec{x}) + \xi(\vec{x} + \vec{k}\mathcal{A}(\vec{x})) = 0, \qquad (\vec{x} \in \mathbb{T}^2). \tag{4.22}$$

Note that the wave number ratio, k, which is set to $1/\sqrt{2}$ in the examples presented here, is the same in physical space as in conformal space. It is shown in [92] that the inverse of the mapping $\vec{x} = \vec{\alpha} + \vec{k}\xi(\vec{\alpha})$ on \mathbb{T}^2 is $\vec{\alpha} = \vec{x} + \vec{k}\mathcal{A}(\vec{x})$.

Panel (a) of Fig. 10 shows a contour plot of $\eta^{\text{phys}}(x_1, x_2)$ for solution B of Figs. 5, 6, 7 and 9. After computing the torus function $\eta(\alpha_1, \alpha_2)$ for solution B in conformal space, we used Brent's method [17] to rapidly solve (4.22) for $\mathcal{A}(\vec{x})$ on a 257 × 257 uniform grid on \mathbb{T}^2 with period cell $[-\pi, \pi]^2$ and then evaluated $\eta^{\text{phys}}(\vec{x})$ via (4.21). The dashed green and red lines in panel (a) show where $\eta^{\text{phys}}(x_1, x_2)$ would be evaluated to extract $\tilde{\eta}^{\text{phys}}(x)$ in (4.20) over $-3\pi \leqslant \alpha \leqslant 3\pi$. Because the deviation of solution B from the periodic wave A is small, as seen in Figs. 7 and 9, it is difficult to see the variation of $\eta^{\text{phys}}(x_1, x_2)$ with respect to x_2 when plotted over the entire torus. In panel (b) of Fig. 10, we repeat the calculation on a subset of the torus, with $x_1 \in [-\pi/20, \pi/20]$ and $x_2 \in [-\pi, \pi]$. The increased resolution achieved by zooming in on this region reveals that the torus function $\eta^{\text{phys}}(x_1, x_2)$ has a maximum at (0, 0). This means the extracted wave $\tilde{\eta}^{\text{phys}}(x)$ is largest at x=0, where the characteristic line (x, kx) passes through (0, 0). In panel (c), we plot the (negative of the) curvature, $\kappa^{\text{phys}}(\vec{x}) = \kappa(\vec{x} + \vec{k}\mathcal{A}(\vec{x}))$, where the formula for $\kappa(\alpha_1, \alpha_2)$ is given in (2.9). These formulas imply that $\tilde{\kappa}(x) = \kappa^{\text{phys}}(x, kx) = (\tilde{\eta}^{\text{phys}})''(x)/[1 + ((\tilde{\eta}^{\text{phys}})''(x))^2]^{3/2}$. We see that $-\kappa^{\text{phys}}(x_1, x_2)$ has a maximum at (0, 0), confirming that the highest peak of $\tilde{\eta}^{\text{phys}}(x)$, which occurs at x=0, coincides with the sharpest peak, where the curvature is most negative.

These results are consistent with the conjecture that the maximum of $\eta^{\text{phys}}(\vec{x})$ at $\vec{x} = (0,0)$ will continue to grow and sharpen to form a singularity at the origin in such a way that the extracted wave $\tilde{\eta}^{\text{phys}}(x)$ forms a 120° corner at x=0. All the other peaks would remain rounded in this limit (assuming the torus function remains smooth except at the origin, where it is continuous but has a discontinuous gradient), though there would be peaks of arbitrarily high curvature as the characteristic line (x, kx) will pass arbitrarily closely to (0,0) modulo $2\pi\mathbb{Z}^2$ as $x\to\pm\infty$. This conjecture is highly

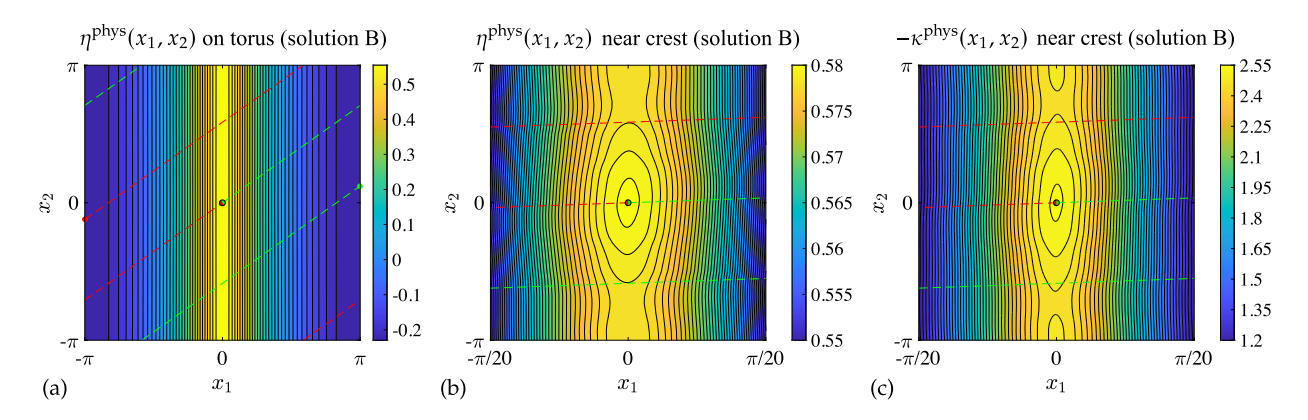


Fig. 10. Contour plots of the torus functions of the wave profile and the negative of the curvature for solution *B* after transforming to a graph-based representation of the solution. The dashed lines in panels (b) and (c) are the same lines shown in panel (a), but we have zoomed in on the wave crest by restricting to $-\frac{\pi}{20} \leqslant x_1 \leqslant \frac{\pi}{20}$.

speculative as there is still a long way to go from solution B to a solution with a sharp corner. The curvature $\tilde{\kappa}^{\text{phys}}(0)$ has only decreased from -2.513 for solution A to -2.554 for solution B and would have to approach $-\infty$ in order to form a corner wave. Bifurcation from solution E is perhaps more promising for reaching a genuinely quasi-periodic wave in which the crest at the origin has a sharp corner since solution E itself is closer to the limiting 120° periodic wave than solution E. The curvature at the crest of solution E is -52.015.

Exploring this conjecture further numerically is currently out of reach due to the computational cost of tracking quasiperiodic solutions on the branch from solution A past solution B or computing any solution on the path bifurcating from solution E. This is partly because the conformal mapping approach is not well suited to representing nearly singular wave profiles. The grid spacing tends to spread out precisely where one needs mesh refinement. This is evident already for solution A in Fig. 8 by comparing the plot of $\tilde{\eta}(\alpha)$ versus α , where the grid is uniformly spaced, to that of $\tilde{\eta}(\alpha)$ versus $\tilde{\xi}(\alpha)$, which describes the curve in physical space. The effect is much worse for solution E, and in the limit that $\tilde{\zeta}(\alpha)$ forms a corner, $\tilde{\eta}(\alpha)$ will form a cusp. Boundary integral methods [90] and auxiliary conformal maps [60,77] are more flexible for controlling the grid spacing but have not yet been adapted to the quasi-periodic setting.

For temporally periodic standing water waves, Penney and Price [68] conjectured that the largest-amplitude standing wave will form a 90° corner each time it comes to rest. Taylor performed wave tank experiments corroborating this conjecture but doubted Penney and Price's analysis [79]. Careful numerical studies suggested that the limiting wave may have a corner as sharp as 60° [63], or even a cusp [72]. Wilkening [88] increased the resolution near the crest tip by a factor of 200 over these previous studies and showed that the Penney and Price conjecture is false due to a breakdown of self-similarity. Increasing the amplitude leads to increasingly complex behavior at small scales that prevents the emergence of a limiting standing wave [90]. It is an interesting open question whether the 120° corner wave conjecture will turn out to be true for spatially quasi-periodic traveling waves, or whether the torus functions will become rough on small scales, diverging in some Sobolev norm before the crest can sharpen to a corner at the origin.

4.2. Overturning quasi-periodic gravity-capillary waves

In this section, we compute the two-parameter family of "type 1" gravity-capillary waves studied numerically by Schwartz and Vanden-Broeck [73] and more recently by Akers, Ambrose and Wright [1] and search for bifurcations to quasi-periodic traveling waves corresponding to $k = 1/\sqrt{2}$. In particular, we obtain overturning quasi-periodic waves that bifurcate from periodic overturning waves.

At large amplitude, the type 1 waves possess a symmetric air pocket at $x=\pi$ that drops down into the fluid, possibly surrounded by overhanging regions of the free surface. By contrast, type 2 waves have two air pockets that drop down into the fluid on either side of $x=\pi$; see Fig. 11. In our dimensionless units with the wavelength normalized to 2π and the acceleration of gravity normalized to g=1, our surface tension parameter τ agrees with the parameter κ used by Wilton [93] and by Schwartz and Vanden-Broeck [73]. The waves we seek, i.e., the primary branch of type 1 periodic traveling waves, bifurcate from zero amplitude for $\tau>1/2$. The case $\tau=1/2$ corresponds to a Wilton ripple [84,93], where there are two solutions of the Stokes expansion, one of which matches up with this family of type 1 waves. This family can be numerically continued to smaller values of τ , which we do, but the result is different than bifurcation from zero amplitude at these smaller values of τ . Indeed, bifurcating from zero amplitude with $\tau \in (1/3, 1/2)$ leads to "type 2" waves [73] that match up with the other solution of the Wilton ripple expansion at $\tau=1/2$. Fig. 11 shows a type 1 wave and a type 2 wave with $\tau=1/2$, with amplitudes chosen just below the point that self-intersection occurs. We use $\hat{\eta}_{1,0}=\hat{\eta}_1$ for the amplitude parameter.

Panel (a) of Fig. 12 shows a contour plot of χ evaluated on the family of type 1 waves we computed. We split the domain of the contour plot into 3 regions

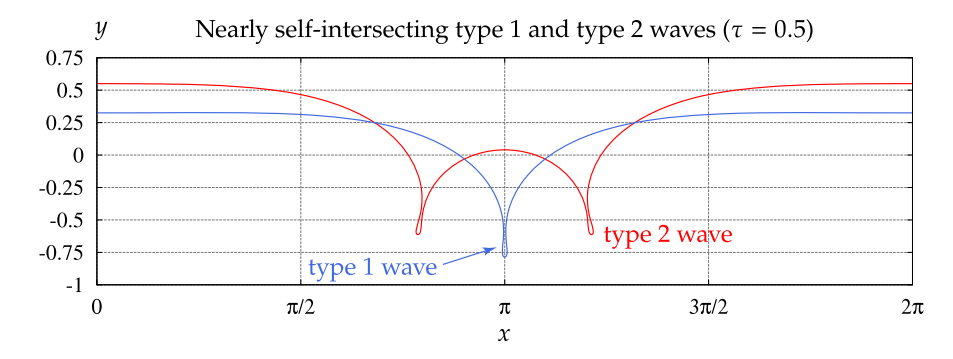


Fig. 11. Nearly self-intersecting type 1 and type 2 periodic traveling gravity-capillary waves with surface tension parameter $\tau = 1/2$. The amplitude parameter is $\hat{\eta}_1 = 0.26417$ for the type 1 wave shown, and $\hat{\eta}_1 = 0.28947$ for the type 2 wave shown.

region 1:
$$1 \le \tau \le 6.5$$
, region 2: $0.52 \le \tau \le 0.98$, region 3: $0.05 \le \tau \le 0.5$. (4.23)

In each region, we sample τ at equal intervals of size $\Delta \tau = 0.05$, 0.02 and 0.01, respectively. At each τ value of regions 1 and 2, we use $s = \hat{\eta}_{1,0}$ as an amplitude parameter and sweep forward with steps of size $\Delta s = 0.01$ until the wave self-intersects to form a trapped bubble. The conformal mapping method can compute non-physical waves in which the free surface crosses through itself to form an overlapping fluid region. We use this feature to root-bracket the amplitude at which the walls of the air bubble first meet. In more detail, once the amplitude is large enough that the wave contains an air pocket with overhanging walls, we compute the first zero, $\alpha_0(s,\tau)$, of $\tilde{\xi}'(\alpha)$ using Newton's method. We then evaluate $\tilde{\xi}(\alpha_0(s,\tau)) - \pi$ as we continue to increase s by $\Delta s = 0.01$. Once this function is positive, the wave has self-intersected and we have found a bracket to use in Brent's method to find $s(\tau)$ such that $\tilde{\xi}(\alpha_0(s(\tau),\tau)) = \pi$ to double-precision accuracy. We then compute $\chi(s,\tau)$ at 81 values of s, uniformly spaced between 0 and $s(\tau)$. As a result, the right boundary of the contour plot corresponds to the maximum amplitude for each τ where the air pocket closes to form a bubble.

In the third region of (4.23), an additional step is taken in which two numerical continuation paths are computed with $s=\hat{\eta}_{1,0}$ held fixed and τ decreasing. The specific choices of s are 0.005 and 0.006, with starting points at $\tau \in \{0.52, 0.54\}$, computed as part of region 2 in (4.23). Once solutions are known with (τ,s) in the range $0.05 \le \tau \le 0.5$ and $s \in \{0.005, 0.006\}$, we proceed as above to find the boundary to the right, but with Δs decreased to 0.001 for the search for the initial bracket for Brent's method. When the right boundary is found (where the air pocket pinches off into an air bubble), we compute χ at 81 equally spaced points between s=0.0017 and the pinch-off amplitude. We re-iterate that only for $\tau > 1/2$ does the wave approach zero-amplitude when the parameter s decreases to zero. We stop at s=0.0017 for $\tau \le 1/2$ since a different bifurcation parameter than $\hat{\eta}_{1,0}$ is needed to properly explore the limit as $s \to 0^+$ when $\tau \le 1/2$ on this sheet of type 1 solutions, and s=0.0017 is small enough for the purpose of plotting $\chi(s,\tau)$.

Because it is a two-parameter family, many solutions had to be computed to generate the contour plot of $\chi(s,\tau)$ in panel (a) of Fig. 12. There are 14661 solutions represented in the plot. The Fourier cutoffs N_1 and N used to compute the traveling waves and χ are as follows:

We set $M_1=3N_1$ and M=3N in all cases. We highlight the zero contours of $\chi(s,\tau)$ in red. There are 4 values of $\tau>0.5$ at which a red contour line reaches the τ axis, i.e., where $\chi(0,\tau)=0$. In the small-amplitude limit, the candidate quasi-periodic bifurcations are plane waves, enumerated by Fourier lattice points $\vec{l}\in\pm\Lambda$ from (3.13). Plane waves with wave numbers $k_1=1$ and $k_2=l_1+kl_2$ can co-exist as traveling waves if they are both roots of the dispersion relation

$$c^2 = \frac{g}{k_j} + \tau k_j, \qquad (j = 1, 2).$$
 (4.25)

Eliminating c^2 and setting g=1, we have $1+\tau=\frac{1}{k_2}+\tau k_2$, or $\tau=1/k_2$. In our calculation, we use Bloch theory to restrict attention to the case $l_2\in\{\pm 1\}$ when constructing \mathcal{J}^{qua} in (3.26). The possible values of τ that exceed 1/2, the Wilton ripple cutoff for type 1 waves, are then

$$\tau = \frac{1}{1-k} = 3.414, \quad \tau = \frac{1}{0+k} = 1.414, \quad \tau = \frac{1}{2-k} = 0.773, \quad \tau = \frac{1}{1+k} = 0.586, \tag{4.26}$$

where $k = 1/\sqrt{2}$. These are precisely the locations where the red contour lines in panel (a) meet the τ axis. We find that the contours at 1.414 and 0.773 form a closed loop, and the contour at 0.586 drops down below $\tau = 0.5$ into region 3 from (4.23), where we used numerical continuation to extend the range of type 1 waves below the Wilton ripple cutoff.

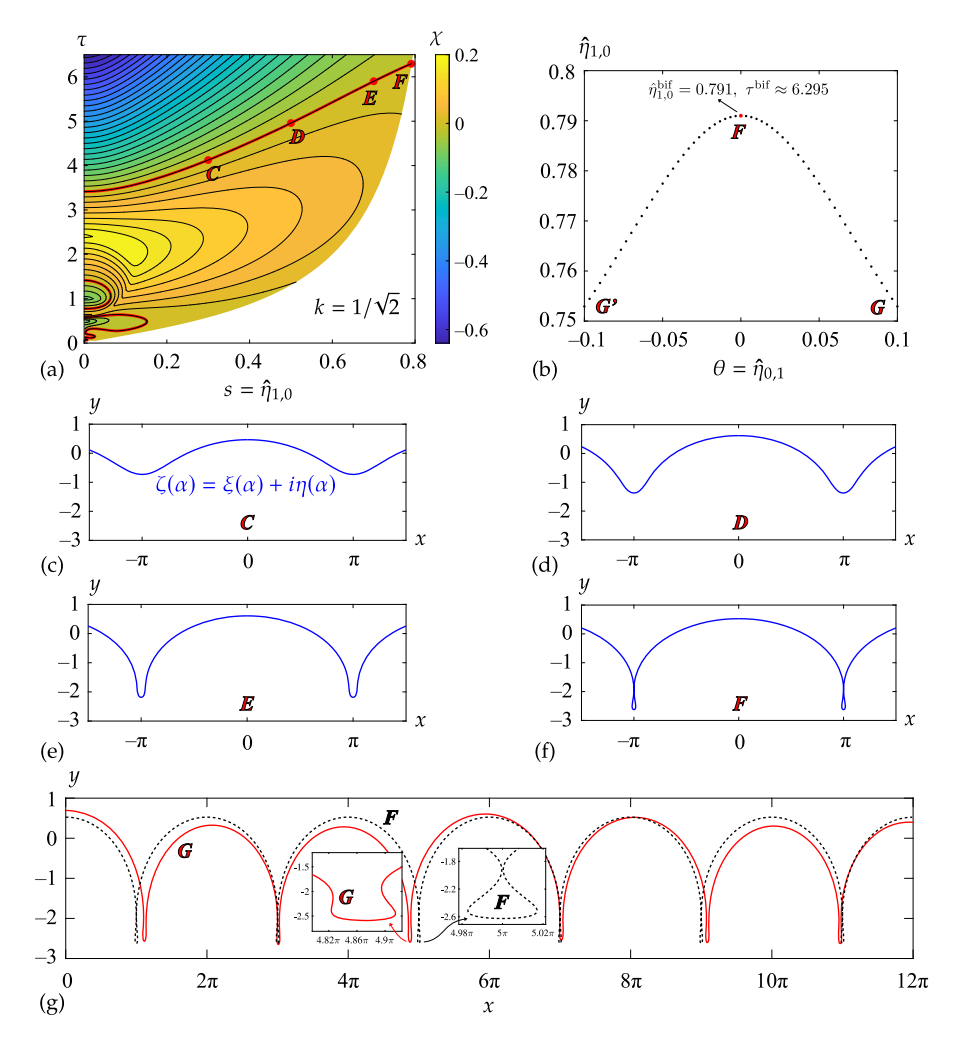


Fig. 12. Contour plot of $\chi(s, \tau)$ for type 1 gravity-capillary waves along with representative examples of bifurcation points on the zero contour of χ and a secondary branch of quasi-periodic, overhanging traveling waves bifurcating from solution F.

We now focus on the remaining contour, which begins at $\tau = 3.414$. We see in Fig. 12 that this contour extends all the way to the right boundary of the contour plot, where the type 1 waves self-intersect at a point, trapping an air bubble below. The solutions labeled C, D, E and E have values of E equal to 0.3, 0.5, 0.7 and 0.791, respectively, and are plotted in panels (E)-(E). As E increases along the contour, the air pocket at E (or one of its E)-periodic translations) deepens, eventually forming a trapped bubble. Solution E has formed a deep air pocket, but the free surface is still a graph. Solution E has overhanging walls that nearly touch. Using polynomial interpolation from the points on the right boundary with E0.1 E1 E2 E3 for E4 E5 E5. We find that the red contour meets the right boundary at

$$(s, \tau) = (0.7916457855, 6.297256422).$$
 (4.27)

Solution F is very close to this, with $(s,\tau)=(0.791,6.294747714)$. Solutions C, D and E correspond to $(s,\tau)=(0.3,4.1248233)$, (0.5,4.9579724) and (0.7,5.8995675), respectively. Each of the waves C-F bifurcates to a quasi-periodic family with basic frequencies $k_1=1$ and $k_2=k=1/\sqrt{2}$. Indeed, the entire red curve corresponding to $\chi=0$ gives the intersection of the two-parameter family of periodic type 1 waves and a two-parameter sheet of such QP waves. Fixing τ or s reduces the problem to a standard one-parameter bifurcation problem of the type studied in Section 4.1 above. See [3,9] for background on the general theory of multi-parameter bifurcation theory.

To explore the existence of spatially quasi-periodic, overhanging traveling waves, we follow the bifurcation branch from solution F using our numerical continuation algorithm. We choose $N_1=N_2=64$, $M_1=M_2=150$ and use $q^{\text{bif}}\pm 10^{-5} \left(0,0,\dot{\eta}^{\text{qua}}\right)$ to jump from the periodic branch to the quasi-periodic branch. The largest Fourier coefficient of $\dot{\eta}^{\text{qua}}$ is $\dot{\eta}^{\text{qua}}_{0,1}\approx 0.6901$. Thus, $\theta=\hat{\eta}_{0,1}$ is a natural choice for the continuation parameter on the QP branch. We hold τ fixed at τ^{bif} in this search. We are able to compute the quasi-periodic continuation path until θ reaches ± 0.1 . The corresponding solution with positive θ , labeled G in panel (b), is plotted in panel (g) of Fig. 12. For this solution, $\hat{\eta}_{1,0}\approx 0.7529$ and the

objective function f is minimized to 3.7×10^{-25} . In panel (b) of Fig. 12, we plot the Fourier coefficients $\hat{\eta}_{1,0}$ and $\hat{\eta}_{0,1}$ of the bifurcated quasi-periodic solutions. Along the quasi-periodic branch, as $|\theta|$ increases, $|\hat{\eta}_{1,0}|$ decreases. We also observe that the plot is symmetric with respect to the vertical line $\hat{\eta}_{0,1}=0$; this is because the quasi-periodic solutions with negative θ can be obtained from ones with positive θ through a spatial shift in α_2 : $(\alpha_1,\alpha_2) \mapsto (\alpha_1,\alpha_2+\pi)$. Solutions G and G' are related in this way.

In panel (g) of Fig. 12, we compare the wave profile $\zeta=\xi+i\eta$ of solution F, which is periodic with amplitude s=0.791, and solution G, which is quasi-periodic with $\theta=0.1$. We observe that the peaks and troughs of the QP solution appear in a non-periodic pattern. The peaks of solution G are above those of solution F near $\xi=0$, G and below near $\xi=2\pi$, G are on the left of those of G are will continue to differ from one peak and trough to the next, never exactly repeating over the real line. We zoom in on the troughs of the two solutions near G and observe that the trough of solution G is asymmetrical and wider than that of the periodic solution G. Neither solution is self-intersecting. Moreover, solution G is further from self-intersecting than solution G. This may be related to the result in panel (b) that increasing G causes G and observe the overhanging walls. Specifically, solution G has G has G on the periodic branch increases the gap between the overhanging walls. Specifically, solution G has G has G on the periodic solution G on the periodic solution G has G on the periodic solution G on the perio

5. Conclusion

We have shown that a signed version, χ , of the smallest singular value, σ_{min} , of the Jacobian serves as an excellent test function to locate branch points in equilibrium problems. While σ_{min} has a slope discontinuity at each of its zeros, the existence of an analytic or smooth SVD ensures that the function becomes smooth when a sign is included on one side of the bifurcation point. We show that this sign factor can be defined as the product of the determinants of the orthogonal matrices containing the left and right singular vectors in the standard SVD, which alleviates the need to actually compute an analytic SVD. We also show how to compute this sign efficiently from the bidiagonal matrix obtained in the first phase of the standard SVD algorithm. It is not necessary to form the matrices of singular vectors, compute their determinants, or compute the determinant of the Jacobian itself.

One benefit of using χ as a test function is that root bracketing algorithms such as Brent's method can then be used to locate bifurcation points. This is simpler than the Newton-type method proposed by Shen [75] to locate zeros of σ_{\min} or by various authors [5,14,16,33,49] to solve minimally extended systems. Within the constraints and philosophy of Remark 3.10, our method is as efficient as these alternative approaches. We also proposed a polynomial interpolation approach using Chebyshev polynomials, which relies on the smoothness of χ to achieve spectral accuracy. In multi-parameter bifurcation problems such as the gravity-capillary problem of Section 4.2, the zero level set of χ can be used to visualize and compute the intersection of the primary family of solutions with the secondary family of solutions. This would not work well using σ_{\min} or ψ from (1.2) instead of χ . We also showed that χ stops changing on further mesh refinement once the singular vectors corresponding to the smallest singular values are resolved. As a result, the plots in Fig. 3 and the contour plot of Fig. 12 are smooth even though many different mesh sizes are used in the underlying calculations plotted. Other test functions such as the determinant of the Jacobian or ψ (s) in (1.2) do not have this mesh independence property, and some behave poorly on large-scale discretizations of infinite dimensional problems.

We use this method to compute, for the first time, quasi-periodic traveling gravity waves with zero surface tension and overhanging traveling gravity-capillary waves. The former example yields traveling waves that still make sense at the scale of the ocean, where the length scale of capillary waves is so much smaller than that of gravity waves (by a factor of 10^{-7}) that one can set $\tau = 0$. Genuinely quasi-periodic pure gravity waves do not persist to zero amplitude, which motivated us to search for quasi-periodic bifurcations from large-amplitude periodic waves. The latter example showcases the use of $\chi(s,\tau)$ to study two-parameter bifurcation problems in which the primary sheet is parameterized over a region with one side bounded by singular solutions. In our case, the right boundary of the contour plot in Fig. 12 corresponds to type 1 waves that self-intersect to form an air pocket. This contour plot makes it easy to visualize how the secondary two-parameter family of quasi-periodic solutions fits together with the primary two-parameter family of periodic traveling waves.

Once bifurcations are found, we use numerical continuation to explore the secondary branches of quasi-periodic solutions. This becomes computationally expensive, especially in the case of the pure gravity wave problem. We formulated the problem of finding solutions on the secondary branch as an overdetermined nonlinear least squares problem and implemented a parallel algorithm employing MPI and ScaLapack to carry out the trust-region minimization steps of the Levenberg-Marquardt method. The largest-amplitude solution we computed, namely solution B of Figs. 5 and 6, required solving for $N_{\text{tot}} = 53398$ independent Fourier modes in its 2D torus representation. We used the Savio cluster at UC Berkeley and the Lawrencium cluster at Lawrence Berkeley National Laboratory for these calculations.

An interesting feature of these solutions is that the 2D Fourier modes $\hat{\eta}_{j_1,j_2}$ continue to exhibit visible effects of resonance near the line $j_1+kj_2=0$ even though these are large-amplitude solutions far from linear water wave theory. We explain this by noting that these modes correspond to long wavelengths when the torus function is restricted to the characteristic line $\alpha_1=\alpha$, $\alpha_2=k\alpha$, and the Euler equations are not strongly affected by long wavelength perturbations. We also identified a symmetry connecting solutions on one side of each secondary bifurcation branch to the other. In particular, solution B' in Fig. 5 is related to solution B via $\eta_{B'}(\alpha_1,\alpha_2)=\eta_B(\alpha_1,\alpha_2+\pi)$. The same symmetry was found in the gravity-

capillary problem, e.g., solutions G and G' in Fig. 12 are also related by this transformation. Figs. 9 and 12 also show that when a large-amplitude periodic traveling water wave is perturbed to create a quasi-periodic traveling wave, each crest and trough of the infinite wave train will undergo a different perturbation, so that no two are exactly the same. Nevertheless, they fit together to form a single traveling wave profile extending over the real line.

We took advantage of Bloch theory to express the Jacobian as a direct sum of operators mapping $(\mathcal{X}_{\sigma}^{\text{per}}, \mathbb{R}, \mathbb{R})$ to $\mathcal{X}_{\sigma}^{\text{per}}$ and $(\mathcal{X}_{\sigma}^{(l_2)}, 0, 0)$ to $\mathcal{X}_{\sigma}^{(l_2)}$. This greatly reduces the number of rows and columns of \mathcal{I}^{qua} in (3.26) since l_2 could be set to 1 rather than varying over some range $-N_2 \leq l_2 \leq N_2$. Bloch theory is also useful for studying the stability of traveling waves to subharmonic perturbations [58,61,62], and indeed the present work of searching for null vectors of the Jacobian of the traveling wave equations can be thought of as a special case of looking for zero eigenvalues of the dynamic stability problem. In the present paper, we have shown that perturbations in null directions of the linearization lead to branches of spatially quasi-periodic traveling waves for the full water wave equations. In future work, it would be interesting to investigate the Benjamin-Feir instability [11,94] and other unstable subharmonic perturbations [29,65,80,82] by evolving them beyond the realm of validity of Bloch stability theory using the dynamic version [92] of our spatially quasi-periodic water wave framework. Linearly stable subharmonic perturbations would also be interesting to investigate as they may lead to solutions of the full water wave equations that are quasi-periodic in time [10,12,13,44,89] as well as space.

CRediT authorship contribution statement

Jon Wilkening: Conceptualization, Data curation, Formal analysis, Funding acquisition, Investigation, Methodology, Project administration, Resources, Software, Supervision, Validation, Visualization, Writing – original draft, Writing – review & editing. **Xinyu Zhao:** Conceptualization, Data curation, Formal analysis, Investigation, Methodology, Software, Validation, Visualization, Writing – original draft, Writing – review & editing.

Declaration of competing interest

The authors declare that they have no known competing financial interests or personal relationships that could have appeared to influence the work reported in this paper.

Data availability

Data will be made available on request.

Acknowledgements

This work was supported in part by the National Science Foundation under award number DMS-1716560 and by the Department of Energy, Office of Science, Applied Scientific Computing Research, under award number DE-AC02-05CH11231. This research used the Lawrencium computational cluster resource provided by the IT Division at the Lawrence Berkeley National Laboratory and the Savio computational cluster provided by the Berkeley Research Computing program at the University of California, Berkeley (supported by the UC Berkeley Chancellor, Vice Chancellor for Research, and Chief Information Officer).

Appendix A. The effects of floating-point errors on the smallest singular value

The SVD algorithm is backward stable [32], which leads to a well-known estimate [31]

$$|\hat{\sigma}_i - \sigma_i| \le p(n) \|f\| \varepsilon, \qquad 1 \le i \le n, \tag{A.1}$$

where $\{\hat{\sigma}_i\}$ are the numerically computed singular values of the $n \times n$ matrix \mathcal{I} , p(n) is a slowly growing function of the matrix dimension, $\|\mathcal{I}\|$ is the 2-norm, and ε is machine precision. Following the approach of [87], one can show that $p(n) \leqslant O(n^{2.5})$ using standard backward stability estimates for Householder transformations in the bidiagonalization phase [32,51]; however, this is pessimistic. In particular, it assumes worst-case $O(n\varepsilon)$ errors when summing n numbers. In practice [8], p(n) is often taken to be 1. In section 4.1, the condition numbers of \mathcal{I}^{qua} for solutions A and E are 1636 and 69074, respectively. Taking p(n)=1, this leads to expected errors in $\chi(s)$ around $(1636)(2.2\times10^{-16})=3.6\times10^{-13}$ and $(69074)(2.2\times10^{-16})=1.5\times10^{-11}$, respectively. Using Brent's method, we reduced $|\chi(s)|$ to 2.9×10^{-15} for solution A. However, Brent's method will report the result in which floating-point errors combine most favorably to minimize $|\chi(s)|$, so this value likely over-predicts the accuracy actually obtained. Indeed, if we increase the size of \mathcal{I}^{qua} from 1537 to 2049 and recompute χ without re-optimizing via Brent's method, we obtain $|\chi|=1.5\times10^{-14}$, which is five times bigger. The flattening of the high-frequency Chebyshev modes χ_m in panel (d) of Fig. 3 suggests floating-point errors around 10^{-11} or 10^{-12} , which is consistent with the above condition number estimate. Chebyshev interpolation seems less prone than Brent's method to optimizing beyond the actual error, so the minimum value of $|\chi(s)|$ obtained in problem E, namely 2.1×10^{-12} , may be accurate. Additional calculations would have to be done in quadruple-precision to fully quantify the effects of floating-point arithmetic in double-precision, but this is beyond the scope of the present work.

Appendix B. Proof of Theorem 3.2

Let us restate the theorem in a slightly more general form that simplifies the proof. Theorem 3.2 is recovered by setting $\rho = \rho_1/2$ and $\sigma_1 = \sigma$.

Theorem B.1. Suppose $q^{per} = (\eta, \tau, b)$ with $\eta \in \mathcal{V}_{\sigma}^{per}$ for some $\sigma > 0$. Suppose also that η is real-valued and the resulting $J(\alpha_1, \alpha_2)$ in (2.9), which is independent of α_2 , is non-zero for every $\alpha_1 \in \mathbb{T}$. Then there exists $\rho_1 \in (0, \sigma]$ such that $D_q \mathcal{R}[q^{per}]$ is a bounded operator from $(\mathcal{V}_{\sigma_1}, \mathbb{C}, \mathbb{C})$ to \mathcal{V}_{ρ} provided that $0 < \rho < \rho_1$ and $\sigma_1 > \rho$.

Proof. Since $\eta \in \mathcal{V}^{\text{per}}_{\sigma}$, we know $\eta(\alpha_1, \alpha_2) = \tilde{\eta}(\alpha_1)$ is independent of α_2 , and $\tilde{\eta}(\alpha)$ is real analytic and 2π periodic. All the torus functions without a dot in (2.34) are then independent of α_2 , and can be replaced by the corresponding 1d extracted function (adding a tilde), evaluated at α_1 . The torus operators ∂_{α} and H are replaced by their 1d variants when this is done. For example, $J(\alpha_1, \alpha_2) = \tilde{J}(\alpha_1)$, where $\tilde{J}(\alpha) = (1 + H\partial_{\alpha}\tilde{\eta})^2 + (\partial_{\alpha}\tilde{\eta})^2$. Since $\tilde{J}(\alpha)$ is continuous and assumed non-zero at each $\alpha \in [0, 2\pi]$, it is bounded away from zero. Thus, each of the functions

$$1/(2\tilde{J}), \quad \tilde{\kappa}, \quad b/(2\tilde{J}^2), \quad (1+H\partial_{\alpha}\tilde{\eta}), \quad \partial_{\alpha}\tilde{\eta}, \quad 3\tilde{\kappa}/(2\tilde{J}), \quad \tilde{J}^{-3/2}, \quad \partial_{\alpha}^2\tilde{\eta}, \quad H\partial_{\alpha}^2\tilde{\eta}$$
 (B.1)

that appears in (2.34) (after setting $\xi = H\eta$) is real analytic and 2π -periodic. As a result (see, e.g., Lemma 5.6 of [19]) the 1d Fourier coefficients of each of these functions decay exponentially. Thus, there exist C, $\rho_1 > 0$ such that $Ce^{-\rho_1|j|}$ is a common bound on each of these sets of Fourier coefficients, i.e., if $\tilde{\gamma}(\alpha) = \sum_j \hat{\gamma}_j e^{ij\alpha}$ represents any of the functions in (B.1), then $|\hat{\gamma}_j| \leqslant Ce^{-\rho_1|j|}$ for $j \in \mathbb{Z}$. Now fix ρ in the range $0 < \rho < \rho_1$ and let $\sigma_1 > \rho$.

We need to show that $D_q \mathcal{R}[q^{\mathrm{per}}]$ is a bounded operator from $(\mathcal{V}_{\sigma_1}, \mathbb{C}, \mathbb{C})$ into \mathcal{V}_{ρ} . It suffices to show that the restrictions to the subspaces $(0, \mathbb{C}, \mathbb{C})$ and $(\mathcal{V}_{\sigma_1}, 0, 0)$ are bounded. In the first case, we have

$$D_q \mathcal{R}(q^{\text{per}})(0, \dot{\tau}, \dot{b}) = P \Big[\dot{b}/(2J) - \kappa \dot{\tau} \Big]. \tag{B.2}$$

Note that 1/(2I) and κ are independent of α_2 . Letting $\gamma(\alpha_1,\alpha_2) = \tilde{\gamma}(\alpha_1)$ represent either of these functions, we have

$$\|\gamma\|_{\psi_{\rho}}^{2} \leqslant C^{2} + 2C^{2} \sum_{i=1}^{\infty} e^{-2(\rho_{1} - \rho)j} = C^{2} + \frac{2C^{2}}{e^{2(\rho_{1} - \rho)} - 1} \leqslant C^{2} + \frac{C^{2}}{\rho_{1} - \rho} = A^{2} < \infty, \tag{B.3}$$

where the last equality defines A. So the V_{ρ} norm of the left-hand side of (B.2) is bounded by $A(|\dot{b}| + |\dot{\tau}|) \leq A\sqrt{2}(\dot{b}^2 + \dot{\tau}^2)^{1/2}$.

Now let $\dot{\eta} \in \mathcal{V}_{\sigma_1}$. We need to compute $\dot{R} = D_q \mathcal{R}[q^{\text{per}}](\dot{\eta}, 0, 0)$ and bound its norm in \mathcal{V}_{ρ} by a constant times $\|\dot{\eta}\|_{\mathcal{V}_{\sigma_1}}$. To compute \dot{R} , we evaluate (2.34) in two steps. First the terms

$$(\partial_{\alpha}\dot{\xi}) = (H\partial_{\alpha}\dot{\eta}), \qquad (\partial_{\alpha}\dot{\eta}), \qquad (\partial_{\alpha}^{2}\dot{\eta}), \qquad (\partial_{\alpha}^{2}\dot{\xi}) = (H\partial_{\alpha}^{2}\dot{\eta}) \tag{B.4}$$

are computed from $\dot{\eta}$. The symbols of $H\partial_{\alpha}$, ∂_{α} , ∂_{α}^2 and $H\partial_{\alpha}^2$ are, respectively, $|l_1+kl_2|$, $i(l_1+kl_2)$, $-(l_1+kl_2)^2$ and $i(l_1+kl_2)|l_1+kl_2|$, so these operators are bounded from \mathcal{V}_{σ_1} to \mathcal{V}_{ρ} since $\sigma_1 > \rho$. For example,

$$\|H\partial_{\alpha}\dot{\eta}\|_{\nu_{\rho}}^{2} = \sum_{l_{1},l_{2}} \left| |l_{1} + kl_{2}|\hat{\eta}_{l_{1},l_{2}} e^{\rho(|l_{1}|+|l_{2}|)} \right|^{2} \leq B^{2} \sum_{l_{1},l_{2}} \left| \hat{\eta}_{l_{1},l_{2}} e^{\sigma_{1}(|l_{1}|+|l_{2}|)} \right|^{2} = B^{2} \|\dot{\eta}\|_{\nu_{\sigma_{1}}}^{2}, \tag{B.5}$$

where $B^2 = \max(1, k) \max_{x \ge 0} x e^{-(\sigma_1 - \rho)x} = \max(1, k)/[e(\sigma_1 - \rho)] < \infty$. The second step is to consider

$$\dot{\mathcal{R}} = P \left[-\frac{b}{2I^2} \dot{J} + g\dot{\eta} - \tau \dot{\kappa} \right]. \tag{B.6}$$

The projection P is bounded on \mathcal{V}_{ρ} , and $\|g\dot{\eta}\|_{\mathcal{V}_{\rho}} \leqslant g\|\dot{\eta}\|_{\mathcal{V}_{\sigma_{1}}}$. Substitution of \dot{J} and $\dot{\kappa}$ in (2.34) into (B.6) yields sums of products containing two factors from the list (B.1) and one factor from the list (B.4). From the first step, we know each term in the list (B.4) is bounded in \mathcal{V}_{ρ} by a constant times $\|\dot{\eta}\|_{\mathcal{V}_{\sigma_{1}}}$. The following lemma shows that multiplication by any of the terms in (B.1) is a bounded operator on \mathcal{V}_{ρ} . Multiplying by two of them is then also bounded, which concludes the proof. \square

Lemma B.2. Suppose $\tilde{\gamma}(\alpha) = \sum_j \hat{\gamma}_j e^{ij\alpha}$ with $|\hat{\gamma}_j| \leq Ce^{-\rho_1|j|}$ for positive constants C and ρ_1 , and fix $\rho \in (0, \rho_1)$. Then multiplication by $\gamma(\alpha_1, \alpha_2) = \tilde{\gamma}(\alpha_1)$ is a bounded operator on \mathcal{V}_ρ .

Proof. Let $u \in \mathcal{V}_{\rho}$ and define $v(\alpha_1, \alpha_2) = \tilde{\gamma}(\alpha_1)u(\alpha_1, \alpha_2)$. The Fourier modes of v are related to those of u by convolution along horizontal slices, $\hat{v}_{l_1, l_2} = \sum_j \hat{\gamma}_{l_1 - j} \hat{u}_{j, l_2}$. Using the bound on $|\hat{\gamma}_j|$, we have

$$\begin{aligned}
e^{\rho(|l_{1}|+|l_{2}|)} |\hat{v}_{l_{1},l_{2}}| &\leq \sum_{j} Ce^{-\rho_{1}|l_{1}-j|} e^{\rho(|l_{1}|-|j|)} \left(e^{\rho(|j|+|l_{2}|)} |\hat{u}_{j,l_{2}}| \right) \\
&\leq \sum_{j} Ce^{-(\rho_{1}-\rho)|l_{1}-j|} e^{-\rho(|l_{1}-j|-|l_{1}|+|j|)} \left(e^{\rho(|j|+|l_{2}|)} |\hat{u}_{j,l_{2}}| \right).
\end{aligned} \tag{B.7}$$

Since $|l_1| \leq |l_1 - j| + |j|$, we can use Young's inequality to conclude

$$\sum_{l_1} e^{2\rho(|l_1|+|l_2|)} |\hat{v}_{l_1,l_2}|^2 \leqslant A^2 \sum_{j} e^{2\rho(|j|+|l_2|)} |\hat{u}_{j,l_2}|^2, \qquad (l_2 \in \mathbb{Z}),$$
(B.8)

where $A = \sum_m Ce^{-(\rho_1-\rho)|m|} \leqslant C + 2C/(\rho_1-\rho) < \infty$. Summing (B.8) over l_2 and square rooting gives $\|v\|_{V_\rho} \leqslant A\|u\|_{V_\rho}$, as claimed. \square

References

- [1] B.F. Akers, D.M. Ambrose, J.D. Wright, Gravity perturbed Crapper waves, Proc. R. Soc. A 470 (2014) 20130526.
- [2] B.F. Akers, W. Gao, Wilton ripples in weakly nonlinear model equations, Commun. Math. Sci. 10 (3) (2012) 1015-1024.
- [3] J.C. Alexander, S.S. Antman, Global and local behavior of bifurcating multi-dimensional continua of solutions for multiparameter nonlinear eigenvalue problems, Arch. Ration. Mech. Anal. 76 (1981) 339–354.
- [4] E.L. Allgower, K. Georg, Numerical Continuation Methods: an Introduction, vol. 13, Springer Science & Business Media, 2012.
- [5] E.L. Allgower, H. Schwetlick, A general view of minimally extended systems for simple bifurcation points, Z. Angew. Math. Mech. 77 (1997) 83-97.
- [6] D.M. Ambrose, J. Wilkening, Computation of time-periodic solutions of the Benjamin-Ono equation, J. Nonlinear Sci. 20 (3) (2010) 277-308.
- [7] C.J. Amick, L.E. Fraenkel, J.F. Toland, On the Stokes conjecture for the wave of extreme form, Acta Math. 148 (1) (1982) 193-214.
- [8] E. Anderson, Z. Bai, C. Bischof, S. Blackford, J. Demmel, J. Dongarra, J.D. Croz, A. Greenbaum, S. Hammarling, A. McKenney, D. Sorensen, LAPACK Users' Guide, third edition, SIAM, Philadelphia, 1999.
- [9] S.S. Antman, Nonlinear Problems of Elasticity, 2nd edition, Springer, New York, 2004.
- [10] P. Baldi, M. Berti, E. Haus, R. Montalto, Time quasi-periodic gravity water waves in finite depth, Invent. Math. 214 (2) (2018) 739-911.
- [11] T.B. Benjamin, J. Feir, The disintegration of wave trains on deep water, J. Fluid Mech. 27 (3) (1967) 417-430.
- [12] M. Berti, L. Franzoi, A. Maspero, Traveling quasi-periodic water waves with constant vorticity, Arch. Ration. Mech. Anal. 240 (2021) 99-202.
- [13] M. Berti, R. Montalto, Quasi-Periodic Standing Wave Solutions of Gravity-Capillary Water Waves, Memoirs of the American Mathematical Society, vol. 263, American Mathematical Society, 2016.
- [14] W.-J. Beyn, W. Kleß, V. Thümmler, Continuation of low-dimensional invariant subspaces in dynamical systems of large dimension, in: B. Fiedler (Ed.), Ergodic Theory, Analysis, and Efficient Simulation of Dynamical Systems, Springer, Berlin, 2001, pp. 47–72.
- [15] D. Bindel, J. Demmel, M. Friedman, Continuation of invariant subspaces in large bifurcation problems, SIAM J. Sci. Comput. 30 (2) (2008) 637–656.
- [16] D. Bindel, M. Friedman, W. Govaerts, J. Hughes, Y. Kuznetsov, Numerical computation of bifurcations in large equilibrium systems in matlab, J. Comput. Appl. Math. 261 (2014) 232–248.
- [17] R.P. Brent, Algorithms for Minimization Without Derivatives, Prentice Hall, Inc., Englewood Cliffs, New Jersey, 1973.
- [18] T. Bridges, F. Dias, Spatially quasi-periodic capillary-gravity waves, Contemp. Math. 200 (1996) 31–46.
- [19] H. Broer, F. Takens, Dynamical Systems and Chaos, Applied Mathematical Sciences., vol. 172, Springer, New York, 2011.
- [20] B. Buffoni, E. Dancer, J. Toland, The regularity and local bifurcation of steady periodic water waves, Arch. Ration. Mech. Anal. 152 (3) (2000) 207-240.
- [21] B. Buffoni, E. Dancer, J. Toland, The sub-harmonic bifurcation of Stokes waves, Arch. Ration. Mech. Anal. 152 (3) (2000) 241-271.
- [22] A. Bunse-Gerstner, R. Byers, V. Mehrmann, N.K. Nichols, Numerical computation of an analytic singular value decomposition of a matrix valued function, Numer. Math. 60 (1991) 1–39.
- [23] B. Chen, P. Saffman, Steady gravity-capillary waves on deep water 1. Weakly nonlinear waves, Stud. Appl. Math. 60 (3) (1979) 183-210.
- [24] B. Chen, P. Saffman, Numerical evidence for the existence of new types of gravity waves of permanent form on deep water, Stud. Appl. Math. 62 (1) (1980) 1–21
- [25] W. Choi, R. Camassa, Exact evolution equations for surface waves, J. Eng. Mech. 125 (7) (1999) 756-760.
- [26] S.-N. Chow, Y.-Q. Shen, Bifurcations via singular value decompositions, Appl. Math. Comput. 28 (1988) 231-245.
- [27] M.G. Crandall, P.H. Rabinowitz, Bifurcation from simple eigenvalues, J. Funct. Anal. 8 (2) (1971) 321-340.
- [28] G.D. Crapper, An exact solution for progressive capillary waves of arbitrary amplitude, J. Fluid Mech. 2 (1957) 532-540.
- [29] B. Deconinck, K. Oliveras, The instability of periodic surface gravity waves, J. Fluid Mech. 675 (2011) 141-167.
- [30] J. Demmel, L. Dieci, M. Friedman, Computing connecting orbits via an improved algorithm for continuing invariant subspaces, SIAM J. Sci. Comput. 22 (2001) 81–94.
- [31] J. Demmel, W. Kahan, Accurate singular values of bidiagonal matrices, SIAM J. Sci. Stat. Comput. 11 (5) (1990) 873-912.
- [32] J.W. Demmel, Applied Numerical Linear Algebra, SIAM, Philadelphia, 1997.
- [33] A. Dhooge, W. Govaerts, Y. Kuznetsov, MATCONT: a MATLAB package for numerical bifurcation analysis of ODEs, ACM Trans. Math. Softw. 29 (2003) 141–164.
- [34] L. Dieci, T. Eirola, On smooth decompositions of matrices, SIAM J. Matrix Anal. Appl. 20 (1999) 800-819.
- [35] L. Dieci, M. Friedman, Continuation of invariant subspaces, Numer, Linear Algebra Appl, 8 (2001) 317–327.
- [36] V.D. Djordjevic, L.G. Redekopp, On two-dimensional packets of capillary-gravity waves, J. Fluid Mech. 79 (1977) 703-714.
- [37] A.I. Dyachenko, On the dynamics of an ideal fluid with a free surface, Dokl. Math. 63 (1) (2001) 115-117.
- [38] A.I. Dyachenko, E.A. Kuznetsov, M. Spector, V.E. Zakharov, Analytical description of the free surface dynamics of an ideal fluid (canonical formalism and conformal mapping), Phys. Lett. A 221 (1–2) (1996) 73–79.
- [39] A.I. Dyachenko, V.E. Zakharov, E.A. Kuznetsov, Nonlinear dynamics of the free surface of an ideal fluid, Plasma Phys. Rep. 22 (10) (1996) 829-840.
- [40] S. Dyachenko, P. Lushnikov, A. Korotkevich, Branch cuts of Stokes wave on deep water. Part I: numerical solution and Padé approximation, Stud. Appl. Math. (2016)
- [41] S. Dyachenko, A.C. Newell, Whitecapping, Stud. Appl. Math. 137 (2016) 199-213.
- [42] S.A. Dyachenko, P.M. Lushnikov, A.O. Korotkevich, Branch cuts of Stokes wave on deep water. Part I: numerical solution and Padé approximation, Stud. Appl. Math. 137 (4) (2016) 419–472.
- [43] I.A. Dynnikov, S.P. Novikov, Topology of quasi-periodic functions on the plane, Russ. Math. Surv. 60 (1) (2005) 1.
- [44] R. Feola, F. Giuliani, Quasi-periodic traveling waves on an infinitely deep perfect fluid under gravity, arXiv:2005.08280, 2020.

- [45] K.V. Fernando, B.N. Parlett, Accurate singular values and differential QD algorithms, Numer. Math. 67 (1994) 191-229.
- [46] M. Friedman, Improved detection of bifurcations in large nonlinear systems via the continuation of invariant subspaces algorithm, Int. J. Bifurc. Chaos Appl. Sci. Eng. 11 (2001) 2277–2285.
- [47] I.S. Gandzha, V.P. Lukomsky, On water waves with a corner at the crest, Proc. R. Soc. A 463 (2007) 1597-1614.
- [48] W.J.F. Govaerts, Numerical Methods for Bifurcations of Dynamical Equilibria, SIAM, Philadelphia, 2000.
- [49] A. Griewank, G. Reddien, Characterization and computation of generalized turning points, SIAM J. Numer. Anal. 21 (1984) 176-185.
- [50] P. Guyenne, E.I.P. arău, Computations of fully nonlinear hydroelastic solitary waves on deep water, J. Fluid Mech. 713 (2012) 307-329.
- [51] N.J. Higham, Accuracy and Stability of Numerical Algorithms, SIAM, Philadelphia, 1996.
- [52] G. looss, P.I. Plotnikov, J.F. Toland, Standing waves on an infinitely deep perfect fluid under gravity, Arch. Ration. Mech. Anal. 177 (2005) 367-478.
- [53] T. Kato, Perturbation Theory for Linear Operators, Springer, Berlin, 1980.
- [54] W. Kinnersley, Exact large amplitude capillary waves on sheets of fluid, J. Fluid Mech. 77 (1976) 229-241.
- [55] C. Kittel, Introduction to Solid State Physics, 8th edition, John Wiley and Sons, New York, 2005.
- [56] S.G. Krantz, Several Complex Variables, 2nd edition, AMS Chelsea Publishing, Providence, RI, 2001.
- [57] Y.A. Kuznetsov, Elements of Applied Bifurcation Theory, 2nd edition, Springer-Verlag, New York, 1998.
- [58] M.S. Longuet-Higgins, The instabilities of gravity waves of finite amplitude in deep water. II. Subharmonics, Proc. R. Soc. Lond. A 360 (1978) 489-505.
- [59] M.S. Longuet-Higgins, M.J.H. Fox, Theory of the almost-highest wave. Part 2. Matching and analytic extension, J. Fluid Mech. 85 (4) (1978) 769-786.
- [60] P. Lushnikov, S. Dyachenko, D. Silantyev, New conformal mapping for adaptive resolving of the complex singularities of Stokes wave, Proc. R. Soc. A 473 (2017) 20170198.
- [61] R.S. MacKay, P.G. Saffman, Stability of water waves, Proc. R. Soc. Lond. A 406 (1986) 115–125.
- [62] J.W. McLean, Instabilities of finite-amplitude water waves, J. Fluid Mech. 114 (1982) 315-330.
- [63] G.N. Mercer, A.J. Roberts, Standing waves in deep water: their stability and extreme form, Phys. Fluids A 4 (2) (1992) 259-269.
- [64] J. Moser, On the theory of quasiperiodic motions, SIAM Rev. 8 (2) (1966) 145–172.
- [65] S. Murashige, W. Choi, Stability analysis of deep-water waves on a linear shear current using unsteady conformal mapping, J. Fluid Mech. 885 (A41) (2020) 1–27.
- [66] A.I. Nekrasov, On steady waves, Izv. Ivanovo-Voznesensk. Politekh. In-ta 3 (1921) 52-65.
- [67] J. Nocedal, S.J. Wright, Numerical Optimization, Springer, New York, 1999.
- [68] W.G. Penney, A.T. Price, Finite periodic stationary gravity waves in a perfect liquid, part II, Philos, Trans. R. Soc. Lond. A 244 (1952) 254-284.
- [69] P. Plotnikov, J. Toland, Nash-Moser theory for standing water waves, Arch. Ration. Mech. Anal. 159 (2001) 1-83.
- [70] P.I. Plotnikov, Nonuniqueness of solutions of the problem of solitary waves and bifurcation of critical points of smooth functionals, Math. USSR-Izv. 38 (2) (1992) 333.
- [71] V.P. Ruban, Water waves over a time-dependent bottom: exact description for 2D potential flows, Phys. Lett. A 340 (2005) 194-200.
- [72] W.W. Schultz, J.M. Vanden-Broeck, L. Jiang, M. Perlin, Highly nonlinear standing water waves with small capillary effect, J. Fluid Mech. 369 (1998) 253–272.
- [73] L.W. Schwartz, J.-M. Vanden-Broeck, Numerical solution of the exact equations for capillary-gravity waves, J. Fluid Mech. 96 (1979) 119-139.
- [74] H. Schwetlick, U. Schnabel, Iterative computation of the smallest singular value and the corresponding singular vectors of a matrix, Linear Algebra Appl. 371 (2003) 1–30.
- [75] Y.-Q. Shen, Computation of a simple bifurcation point using one singular value decomposition nearby, Computing 58 (1997) 335-350.
- [76] G.G. Stokes, On the theory of oscillatory waves, Trans. Camb. Philos. Soc. (1880).
- [77] M. Tanaka, The stability of steep gravity waves, J. Phys. Soc. Jpn. 52 (9) (1983) 3047-3055.
- [78] S. Tanveer, Singularities in water waves and Rayleigh-Taylor instability, Proc. R. Soc. Lond. A 435 (1991) 137-158.
- [79] G.I. Taylor, An experimental study of standing waves, Proc. R. Soc. A 218 (1953) 44-59.
- [80] R. Tiron, W. Choi, Linear stability of finite-amplitude capillary waves on water of infinite depth, J. Fluid Mech. 696 (2012) 402.
- [81] J.F. Toland, et al., Stokes waves, Topol. Methods Nonlinear Anal. 7 (1) (1996) 1-48.
- [82] O. Trichtchenko, B. Deconinck, J. Wilkening, The instability of Wilton's ripples, Wave Motion 66 (2016) 147-155.
- [83] H. Uecker, D. Wetzel, J. Rademacher, Pde2path a Matlab package for continuation and bifurcation in 2D elliptic systems, Numer. Math., Theory Methods Appl. 7 (1) (2014) 58–106.
- [84] J.-M. Vanden-Broeck, Gravity-Capillary Free-Surface Flows, Cambridge University Press, Cambridge, 2010.
- [85] J.-M. Vanden-Broeck, On periodic and solitary pure gravity waves in water of infinite depth, J. Eng. Math. 84 (1) (2014) 173-180.
- [86] Z. Wang, J. Vanden-Broeck, P. Milewski, Two-dimensional flexural–gravity waves of finite amplitude in deep water, IMA J. Appl. Math. 78 (4) (2013) 750–761.
- [87] J. Wilkening, An algorithm for computing Jordan chains and inverting analytic matrix functions, Linear Algebra Appl. 427 (2007) 6-25.
- [88] J. Wilkening, Breakdown of self-similarity at the crests of large amplitude standing water waves, Phys. Rev. Lett. 107 (2011) 184501.
- [89] J. Wilkening, Traveling-standing water waves, Fluids 6 (187) (2021) 1-35.
- [90] J. Wilkening, J. Yu, Overdetermined shooting methods for computing standing water waves with spectral accuracy, Comput. Sci. Discov. 5 (1) (2012) 014017
- [91] J. Wilkening, X. Zhao, Quasi-periodic travelling gravity-capillary waves, J. Fluid Mech. 915 (A7) (2021) 1-35.
- [92] J. Wilkening, X. Zhao, Spatially quasi-periodic water waves of infinite depth, J. Nonlinear Sci. 31 (52) (2021) 1-43.
- [93] J. Wilton, On ripples, Philos. Mag. Ser. 6 173 (173) (1915) 688-700.
- [94] V.E. Zakharov, Stability of periodic waves of finite amplitude on the surface of a deep fluid, J. Appl. Mech. Tech. Phys. 9 (2) (1968) 190-194.
- [95] E. Zeidler, Applied Functional Analysis: Main Principles and Their Applications, Springer, New York, 1995.
- [96] J. Zufiria, Non-symmetric gravity waves on water of infinite depth, J. Fluid Mech. 181 (1987) 17–39.